

**Wide Band Gap Compound Semiconductor  
Detectors for X-ray Spectroscopy in Harsh  
Environments**

Thesis submitted for the degree of  
Doctor of Philosophy  
at the University of Leicester

by

Anna Megan Barnett  
Space Research Centre  
Department of Physics and Astronomy

December 2011

# Wide Band Gap Compound Semiconductor Detectors for X-ray Spectroscopy in Harsh Environments

Anna Megan Barnett

## Abstract

Novel photon counting  $\text{Al}_{0.8}\text{Ga}_{0.2}\text{As}$ , GaAs and SiC X-ray photodiodes were investigated through experiments and Monte Carlo computer simulations for their suitability as spectroscopic soft ( $\leq 25$  keV) X-ray detectors in high temperature (up to 90 °C) environments.

Photon counting  $\text{Al}_{0.8}\text{Ga}_{0.2}\text{As}$  and GaAs non-avalanche  $\text{p}^+\text{-i-n}^+$  mesa X-ray photodiodes were shown to operate at temperatures as high as 90 °C. The temperature dependences of their spectral resolutions (FWHM at 5.9 keV) are reported. Analyses of the noise sources contributing to the devices' measured performances are presented which suggest that efforts to improve the spectral resolutions would be well targeted at reducing the noise contributions from the packaging of the detectors. For the GaAs diodes, the X-ray characterisation of the devices was extended to higher energies (25 keV). Internal detector X-ray fluorescence was demonstrated and Monte Carlo computer simulations were compared with the experimental results.

Prior to the research presented in this thesis, the only  $\text{Al}_{0.8}\text{Ga}_{0.2}\text{As}$  photon counting X-ray avalanche photodiodes reported in the literature (Lees et al., 2008, Nucl. Instr. and Meth. A, Vol. 594, pp. 202-205) had shown anomalies in the obtained spectra. Through new experimental measurements and computer simulations, the anomaly is explained. A new method was developed which uses the phenomenon to extract measurements of the electron and hole ionisation coefficients of  $\text{Al}_{0.8}\text{Ga}_{0.2}\text{As}$  at a typical operating field and the first report of their temperature dependence is made.

Measurements characterising the X-ray spectroscopic performance of Semi-Transparent SiC Schottky Diodes over an energy range  $\sim 6$  keV to 25 keV at temperatures up to 80 °C are presented and discussed, along with relative efficiency measurements and data showing the temperature dependence of the leakage current in such devices.

The research presented in this thesis shows that  $\text{Al}_{0.8}\text{Ga}_{0.2}\text{As}$ , GaAs and SiC X-ray detectors are promising devices for high temperature soft X-ray spectroscopy.

# Acknowledgements

My most heartfelt thanks are extended to all who made the completion of this thesis possible, most notably Dr John Lees and David Bassford. The time, patience and encouragement they have both shown in guiding me through three years of research have been vital. I have benefited enormously from their experience, clarity of thought and friendship and I feel extremely fortunate to have had such good luck as to work with them.

I am grateful to Prof George Fraser for accepting me onto the PhD programme at the Space Research Centre at University of Leicester, and for his advice, support and expertise, which have ensured I retain a suitable perspective on my work. I am also grateful to Dr Darren Wright for providing a refreshing and lucid independent view, and to Dr Jo Shien Ng, Dr Chee Hing Tan and Dr Alton Horsfall who provided the devices used in this work, along with much valuable advice and semiconductor engineering expertise.

I am appreciative, too, of my friends and colleagues throughout the SRC, particularly Dr Dean Talboys, Oliver Blake, Dr Adrian Martindale and Dr Graeme Hansford who warmly welcomed me and called by my office each day at coffee time, and to Dr Nigel Bannister for the music.

The financial support received from the Science and Technology Facilities Council in the form of a studentship is also gratefully acknowledged.

Finally, but by no means least, I am so very thankful to Mum and Dad for their love and support, and to Sarah for making life worthwhile.

# Contents

<b>Abstract</b>	<b>1</b>
<b>Acknowledgements</b>	<b>2</b>
<b>Contents</b>	<b>3</b>
<b>Publications</b>	<b>8</b>
<b>Chapter 1 Introduction</b>	<b>9</b>
1.1 Background	9
1.2 Motivation	10
1.3 Applications and requirements for high temperature tolerant soft X-ray detectors	10
1.3.1 Extraterrestrial Planetary Analysis	10
1.3.1.1 In situ planetary analysis	10
1.3.1.2 Planetary remote sensing	11
1.3.2 Terrestrial applications	13
1.4 Compound semiconductors for X-ray spectroscopy	14
1.5 Thesis organisation	18
<b>Chapter 2 Detector physics</b>	<b>20</b>
2.1 Introduction	20
2.2 X-ray attenuation	20
2.2.1 Beer-Lambert law	20
2.2.2 Photoelectric absorption	21

2.2.3	Absorption edges	21
2.3	Diode structure	22
2.4	Charge generation	25
2.5	Charge transport	27
2.6	Energy resolution and noise sources	28
2.6.1	Introduction	28
2.6.2	The energy resolution of a semiconductor detector	29
2.6.3	Parallel white noise	29
2.6.4	Series white noise	30
2.6.5	1/f series noise	31
2.6.6	Dielectric noise	31
2.6.7	Induced gate current noise	31
2.6.8	Electronic noise sources in combination	32
2.7	Impact ionisation	32
2.7.1	Introduction	32
2.7.2	Background theory	34
2.7.3	Multiplication factors	35
2.7.4	Excess noise factor	36
<b>Chapter 3</b>	<b>Monte Carlo model</b>	<b>39</b>
3.1	Introduction	39
3.2	Detector properties definition	40
3.3	X-ray source properties definition	41
3.4	X-ray attenuation and photoelectric absorption	41

3.5	Electron-hole pair creation	42
3.6	X-ray fluorescence	42
3.7	Avalanche multiplication	46
3.8	Spectrum generation	47
<b>Chapter 4 The temperature dependence of <math>\text{Al}_{0.8}\text{Ga}_{0.2}\text{As}</math> non-avalanche photodiodes</b>		<b>48</b>
4.1	Introduction	48
4.2	Background	48
4.3	Diode fabrication and design	49
4.4	Leakage current measurements	52
4.5	$^{55}\text{Fe}$ X-ray spectral measurements	55
4.6	Noise analysis	58
4.6.1	Initial measurements	58
4.6.2	Shaping time measurements	59
4.7	Conclusions and discussion	64
<b>Chapter 5 High temperature GaAs non-avalanche photodiodes</b>		<b>66</b>
5.1	Introduction	66
5.2	Diode design and fabrication	66
5.3	Leakage current measurements	68
5.4	$^{55}\text{Fe}$ X-ray spectral measurements	70
5.5	Noise analysis	73
5.5.1	Initial measurements	73
5.5.2	Shaping time measurements	74

5.6	$^{109}\text{Cd}$ spectra and GaAs diode internal X-ray fluorescence	78
5.7	Conclusions and discussion	83
<b>Chapter 6 Photon counting <math>\text{Al}_{0.8}\text{Ga}_{0.2}\text{As}</math> avalanche photodiodes</b>		<b>85</b>
6.1	Introduction	85
6.2	Diode fabrication, design and selection	86
6.3	Initial computer simulations	87
6.3.1	X-ray source definition	87
6.3.2	Detector properties definition	87
6.3.3	Initial simulation results	87
6.4	Experimentally observed spectra	90
6.5	Interpretation of experimental results and model adaptation	92
6.6	Adapted model results	93
6.7	Reduced $\text{p}^+$ layer thickness simulations	95
6.8	Temperature dependence of the impact ionisation coefficients in $\text{Al}_{0.8}\text{Ga}_{0.2}\text{As}$	97
6.8.1	Experimental measurements	97
6.8.2	Computer modelling and the determination of $\alpha$ and $\beta$	98
6.9	Conclusions and discussion	101
<b>Chapter 7 High temperature semi-transparent 4H-SiC Schottky photodiodes</b>		<b>103</b>
7.1	Introduction	103
7.2	Diode fabrication and design	104
7.3	Leakage current measurements	106

7.4	X-ray spectral resolution measurements	107
7.5	Noise analysis	110
7.6	Detector quantum efficiency	112
7.7	Conclusions and discussion	115
<b>Chapter 8</b>	<b>Summary, conclusions and further work</b>	<b>116</b>
8.1	Summary and conclusions	116
8.2	Further work	119
	<b>Bibliography</b>	<b>122</b>

## Publications

**A.M. Barnett**, D.J. Bassford, J.E. Lees, J.S. Ng, C.H. Tan, J.P.R. David, 2010, Temperature dependence of AlGaAs soft X-ray detectors, Nucl. Inst. and Meth. A, Vol. 621, Iss. 1-3, pp. 453-455.

**A.M. Barnett**, J.E. Lees, D.J. Bassford, J.S. Ng, C.H. Tan, R.B. Gomes, 2011, Modelling results of avalanche multiplication in AlGaAs soft X-ray APDs, Nucl. Inst. and Meth. A, Vol. 626-627, pp. 25-30.

**A.M. Barnett**, J.E. Lees, D.J. Bassford, J.S. Ng, C.H. Tan, R.B. Gomes, 2011, Temperature dependence of the avalanche multiplication process and impact ionization coefficients in  $\text{Al}_{0.8}\text{Ga}_{0.2}\text{As}$ , Nucl. Inst. and Meth, Vol. 629, Iss. 1, pp. 154-156.

J.E. Lees, **A.M. Barnett**, D.J. Bassford, R.C. Stevens, A.B. Horsfall, 2011, SiC X-ray detectors for harsh environments, J. Inst, Vol. 6, C01032.

C.H. Tan, R.B. Gomes, J.P.R. David, **A.M. Barnett**, D.J. Bassford, J.E. Lees, J.S. Ng, 2011, Avalanche Gain and Energy Resolution of Semiconductor X-ray Detectors, IEEE Trans. Elect. Dev., Vol. 58, No. 9, pp. 1696-1701.

**A.M. Barnett**, J.E. Lees, D.J. Bassford, J.S. Ng, C.H. Tan, N. Babazadeh, R.B. Gomes, 2011, The spectral resolution of high temperature GaAs photon counting soft X-ray photodiodes, Nucl. Instr. and Meth. A., Vol. 654, pp. 336-339.

J.E. Lees, **A.M. Barnett**, D.J. Bassford, J.S. Ng, C.H. Tan, N. Babazadeh, R.B. Gomes, P. Vines, R.D. McKeag, and D. Boe, 2011, Development of high temperature AlGaAs soft X-ray photon counting detectors, J. Inst. Vol. 6, C12007.

J.E. Lees, **A.M. Barnett**, D.J. Bassford, J.S. Ng, C.H. Tan, N. Babazadeh, R.B. Gomes, P. Vines, R.D. McKeag and D. Boe, 2011, Development of AlGaAs avalanche diodes for soft X-ray photon counting, IEEE conference on Room Temperature Semiconductor Detectors, Valencia Spain, 2011.

**A.M. Barnett**, J.E. Lees, D.J. Bassford, J.S. Ng, 2012, A varied shaping time noise analysis of  $\text{Al}_{0.8}\text{Ga}_{0.2}\text{As}$  and GaAs X-ray photodiodes, Nucl. Instr. and Meth. A., Vol. 673, pp. 10-15.

# Chapter 1 Introduction

## 1.1 Background

In 1913, Henry Moseley published research concerning the X-ray spectra of chemical elements (Moseley, 1913) with a view to testing a hypothesis made by Antonius van der Broek, stating that the chemical and optical properties (including X-ray properties) of the elements were determined by each element's atomic number,  $Z$ , rather than its atomic mass,  $A$  (Heilbron, 1966). Moseley's work, which confirmed a link between X-ray frequency and atomic number,  $Z$ , set the stage for X-ray spectroscopy to become the indispensable tool it is today, used in disciplines as varied as the analysis of works of art and the in situ investigation of the soils of other planets. In the years that have passed since Moseley published his findings, scientists and engineers have produced ever more sensitive and user-friendly instruments for the detection of X-rays and the characterisation of the elements and their abundances in samples of unknown composition.

In the 1960s, the first detectors based upon semiconducting material became available. Today, semiconductor soft X-ray ( $\leq 20$  keV) detectors are most often silicon based and take one of several broad structural forms, including charge coupled devices (CCDs) (Miyaguchi et al., 1999), silicon drift detectors (SDDs) (Gatti & Rehak, 1984), DEPFETs (Kemmer & Lutz, 1987) (Kemmer et al., 1990) and photodiodes (Kataoka et al., 2005). Semiconductor X-ray detectors have many advantages compared to other detector types. Their improving spectral resolution, availability in imaging array format and lower cost, along with their smaller size, have led to the present high popularity of semiconductor detectors among a wide variety of X-ray spectroscopists (Knoll, 2000) (Potts & West, 2008). However, silicon semiconductor detectors do have limitations. They are often prone to radiation damage that can degrade their performance (Hall and Holland, 2010) (Cappelletti, Cédola, & Blancá, 2008), and in order to achieve their optimum performance and spectral resolution they usually need to be operated at low ( $\leq 20$  °C) (Lechner et al., 1996) or sometimes near-cryogenic ( $\sim -120$  °C) temperatures (Abbey et al., 2003). The systems required to support a silicon semiconductor detector

needing to operate in a non-ideal (high temperature, intense radiation) environment are, therefore, not insignificant: protection against radiation damage must be designed into the system, as must facilities for cooling.

A review of the most important methods and detector types, including semiconductor detectors, developed for space related X-ray spectroscopy in the latter half of the twentieth century, can be found in Fraser (1989). A review of their use and applications in a wide variety of fields, where X-ray spectroscopy use flourishes particularly because of the miniaturisation of instrumentation brought by the semiconductor revolution, can be found in Potts and West (2008).

## **1.2 Motivation**

The development of semiconductor X-ray detectors that can operate at high temperature without any (or only minimal) cooling would enable X-ray spectroscopy to be used in many applications that are currently unable, through financial cost or energy, mass, volume or other technical restrictions, to accommodate the cooling apparatus (such as Peltier or cryogenic coolers) that may be required for silicon detectors in such environments. Even in applications that are able to accommodate the cooling needs of existing detectors, reducing the requirements for cooling would enable costs to be reduced and X-ray spectroscopy to be deployed more widely. If high temperature tolerant semiconductor detectors could be developed, they would be very attractive candidates for X-ray spectrometers for future space missions to hot environments such as the surface of Venus.

## **1.3 Applications and requirements for high temperature tolerant soft X-ray detectors**

### **1.3.1 Extraterrestrial Planetary Analysis**

#### **1.3.1.1 In situ planetary analysis**

The driving factors for X-ray spectrometers designed to be landed on the surface of planetary bodies, are mass, power, volume and performance. Instrument mass, power requirements and volume must all be minimised due to technological limitations and the financial restrictions inherent in, and imposed upon, space missions. Typically, for X-ray spectrometers to be deployed on landers or rovers, mass, power and volume

budgets are of the order of 1 kg, 10 W and  $10^3 \text{ cm}^3$ , with the requirement that the instrument must survive mechanical vibrations  $> 10 \text{ g}$  and be tolerant of high levels ( $> 10 \text{ Gy}$ ) of ionising radiation (Fraser, 2008). The environment in which the instrument is required to operate can also be extreme and vary dramatically: Martian surface temperatures reported by the Mars Exploration Rover Opportunity have varied between 295 K and 175 K (Spanovich et al., 2006) at surface pressures of  $610 \text{ Pa} \pm 110 \text{ Pa}$  (Withers & Smith, 2006) and if one wished to perform X-ray spectroscopy on the surface on Venus, where the environment is even more extreme, the instrument would have to survive temperatures  $\approx 735 \text{ K}$  and pressures at the surface  $\approx 9 \text{ MPa}$  (Moroz, 2002). Instruments can, of course, be designed so that the detector is exposed to less extreme environments, but using a detector that is able to cope with less protection may reward the designer with a lighter, smaller and simpler instrument.

In situ X-ray fluorescence analysis of planetary surfaces is typically concerned with determining the elemental composition of a rocky surface with a view to elucidating its history and formation. Thus it is necessary that detectors for this purpose be capable of resolving X-ray lines that will enable the identification of the major rock forming elements. A low energy limit to include magnesium ( $K\alpha = 1.25 \text{ keV}$ ), aluminium ( $K\alpha = 1.49 \text{ keV}$ ) and silicon ( $K\alpha = 1.74 \text{ keV}$ ), and an upper limit to include at least iron ( $K\alpha = 6.4 \text{ keV}$ ) is required along with a spectral resolution sufficient to separate those close, low energy lines (ideally  $\sim 150 \text{ eV}$  FWHM at  $1.5 \text{ keV}$ ). However, detectors with slightly lower spectral resolution (e.g.  $\sim 300 \text{ eV}$  FWHM at  $5.9 \text{ keV}$ ) may still prove attractive options if their high temperature tolerance is essential for the mission (e.g. as might be found for a surface mission to Venus or Mercury). For in situ planetary X-ray spectroscopy, as for many other applications, it is desirable for the detector have high quantum efficiency (see §2.2.1) throughout the X-ray energy range of interest ( $\sim 1 \text{ keV} - 7 \text{ keV}$ ) in order to detect as large a proportion of the radiated flux as possible to minimise spectrum accumulation time; a thick ( $500 \mu\text{m}$ ) silicon detector has a quantum efficiency  $\approx 0.99$  at  $6.4 \text{ keV}$ .

### 1.3.1.2 Planetary remote sensing

For remote sensing X-ray spectroscopy, unlike for in situ analysis, the source used to fluoresce the sample is not a radioisotope X-ray source or X-ray tube carried with the spectrometer, but instead a source external to the instrument, such as the Sun. For

airless bodies near the sun (e.g. Mercury, Earth's Moon and near earth objects) the solar X-rays can fluoresce the surface of the body. However, at distances further from the sun, the solar flux is not great enough to produce sufficient, detectable fluorescence. However, X-rays have been detected from Jupiter and its moons (Gladstone et al., 2002) (Elsner et al., 2002) and Saturn (Ness, 2004). Here the X-rays are thought to be generated through energetic ion interactions (Gladstone et al., 2002) (Elsner et al., 2002) (Ness, 2004) rather than solar induced fluorescence.

As is the case for in situ planetary analysis, the constraints for remote sensing detectors are challenging. Low mass, low power and small volume must be coupled with excellent spectral resolution and good performance at very soft X-ray energies with a  $\sim 1$  keV low energy cut off. The MUSES-C/Hayabusa X-ray Spectrometer, which used a silicon CCD cooled to  $-60$  °C as its detector (Miyaguchi, 1999) and was designed for, and used in, a remote sensing X-ray spectroscopy mission to asteroid Itokawa, is an example of one such instrument. In ideal conditions the detector could achieve a FWHM = 160 eV at 5.9 keV and its 0.7 keV low energy cut off allowed the detection of the K shell lines of the lighter rock forming elements such as magnesium ( $K\alpha = 1.25$  keV), aluminium ( $K\alpha = 1.49$  keV) and silicon ( $K\alpha = 1.74$  keV) along with the L shell lines of elements such as nickel ( $L\alpha = 0.85$  keV) and copper ( $L\alpha = 0.93$  keV). Whilst the instrument was capable of sensing energies up to 10 keV, it was found that the heavier elements were only detected during solar flares when the solar X-ray emissions became more intense at higher energy, enabling the heavier elements with larger electron binding energies to be fluoresced (Okada et al., 2006). At those times of increased solar activity, however, the lower detection limit became sulphur ( $K\alpha = 2.37$  keV) due to increases in instrument noise and a low signal to noise ratio (Okada et al., 2006).

It has also been shown that X-ray detectors with more modest spectral resolution (e.g.  $\sim 380$  eV FWHM @ argon  $K\alpha$  (2.96 keV)) can be scientifically useful for spectroscopic X-ray remote sensing missions (Grande et al., 2007) (Swinyard et al., 2009). A radiation hard detector that could achieve these performance characteristics would be of interest for future missions to rocky planets, moons and asteroids, and a detector with an even lower energy cut off would be useful for missions to Jupiter and its moons since X-ray emissions from Jupiter have been detected in the range 0.25 keV to 2 keV (Elsner, 2002). As for in situ X-ray spectroscopy, it is desirable to maximise the

quantum efficiency of the detector in order to reduce accumulation time. This can be particularly important for remote sensing X-ray fluorescence spectroscopy where typically the instrument is moving relative to the sample of interest. However, at such soft X-ray energies as would be of interest in a mission to Jupiter or Saturn, the quantum efficiency (§2.2.1) of some detectors can be poor due to a non-sensitive region at the front of the detector absorbing low energy photons before they can reach the active region of the device (see §6.7). Furthermore, for many detectors there are discontinuities in the dependence of quantum efficiency on photon energy in this region (0.25 keV to 2 keV) due to X-ray absorption edges (see §2.2.3).

### 1.3.2 Terrestrial applications

Terrestrial laboratories do not have the same degree of constraint on energy use, mass and volume that spacecraft do, and the laboratory environment can be more easily controlled for the benefit of the instruments than can the operating environment of an instrument orbiting another planet. Consequently, terrestrial applications for a high temperature detector are in situations where X-ray spectroscopy is needed outside of a laboratory environment and where energy, mass, volume or cost are driving factors. Oil condition monitoring using X-ray fluorescence for mechanical apparatus is one such application.

Much time and money is invested by the owners of high value, oil lubricated equipment (e.g. engines of railway locomotives, aircraft, military vehicles and Formula 1 racing cars) to ensure that their engines and oils are performing optimally. As part of this process, oils are monitored offline to detect increases in the concentration of the products of engine wear (e.g. lead ( $L\alpha_1 = 10.55$  keV), iron ( $K\alpha_1 = 6.40$  keV), aluminium ( $K\alpha_1 = 1.49$  keV) and silicon ( $K\alpha_1 = 1.74$  keV)), and decreases in the oil additives which improve oil function e.g. molybdenum ( $K\alpha_1 = 17.48$  keV) and sulphur ( $K\alpha_1 = 2.31$  keV) (Yang, Hou & Jones, 2003), (Bently Tribology Services, N.D.). At present, in the case of railway locomotives, oil samples are taken from the engine by hand and sent to a laboratory where the oil is analysed and the results returned to the customer. The process is continually repeated, typically on a weekly basis (Harrison, 2009). Much importance is placed by the operators of railway locomotives on ensuring their engines and oils are functioning optimally because engine damage is very costly and disruptive to business. Being able to monitor the engine oil in situ, in near real time,

would eliminate the need to send oil samples to laboratories and enable detection of problematic engine wear sooner than would otherwise occur. The instruments could report their information to displays in the driver's cab and/or via telecommunication networks to control rooms. Integration of X-ray spectrometers into engines for such applications requires that the detectors can function without bulky cooling systems because of volume and complexity of servicing restrictions. This need for miniaturisation is even more evident in the very mass and volume sensitive cases of aircraft and Formula 1 engines, where operating environments can be even harsher and the penalties for failure more severe than in railway locomotive engines.

Instruments for in situ engine oil monitoring need to be small enough ( $\leq 10^3 \text{ cm}^3$ ) and sufficiently low mass ( $\leq 1 \text{ kg}$ ) to be integrated into the engine and to be able to operate at engine oil temperature ( $\sim 100 \text{ }^\circ\text{C}$ ) to enable continuous monitoring. For oil condition monitoring, the instrument does not need to be imaging but it should have good enough spectral resolution to resolve the spectral lines of interest. As for planetary X-ray fluorescence spectroscopy, the quantum efficiency of the detector should be maximised in order to minimise spectrum accumulation time. In the case of engine oil monitoring, a shorter spectrum accumulation time enables monitoring with better time resolution, and consequently provides the ability to detect changes in oil and engine condition more quickly.

## 1.4 Compound semiconductors for X-ray spectroscopy

Compound semiconductors provide the opportunity to engineer detectors with material properties that are specifically suitable for the environment in which they are required to operate. Wide band gap compounds offer the potential for use in high temperature, extreme radiation environments that cannot be matched by silicon. An introduction to modern compound semiconductor radiation detector research can be found in Owens & Peacock (2004). Another, earlier, review was by McGregor and Hermon (1997).

In a compound semiconductor, it is possible to engineer the band gap,  $E_g$ , (the energy gap between valence and conduction bands) by modifying its average lattice constant (Owens & Peacock, 2004) by changing alloy composition, see **Fig. 1.1**. In some materials such as  $\text{Al}_x\text{Ga}_{1-x}\text{As}$ , the band gap changes rapidly with  $x$  and the lattice constant is relatively insensitive, making lattice matching of  $\text{Al}_x\text{Ga}_{1-x}\text{As}$  to GaAs substrates possible. Through the ability to select the preferred band gap, the device

designer can balance the improvements in the intrinsic resolution of the detector that derive from a narrower band gap (narrower band gaps give rise to improved charge carrier statistics) with the reduction of temperature dependent noise associated with a wider band gap (wider band gaps reduce leakage currents thus leading to reduced noise – see §2.6.3) for a particular temperature regime.

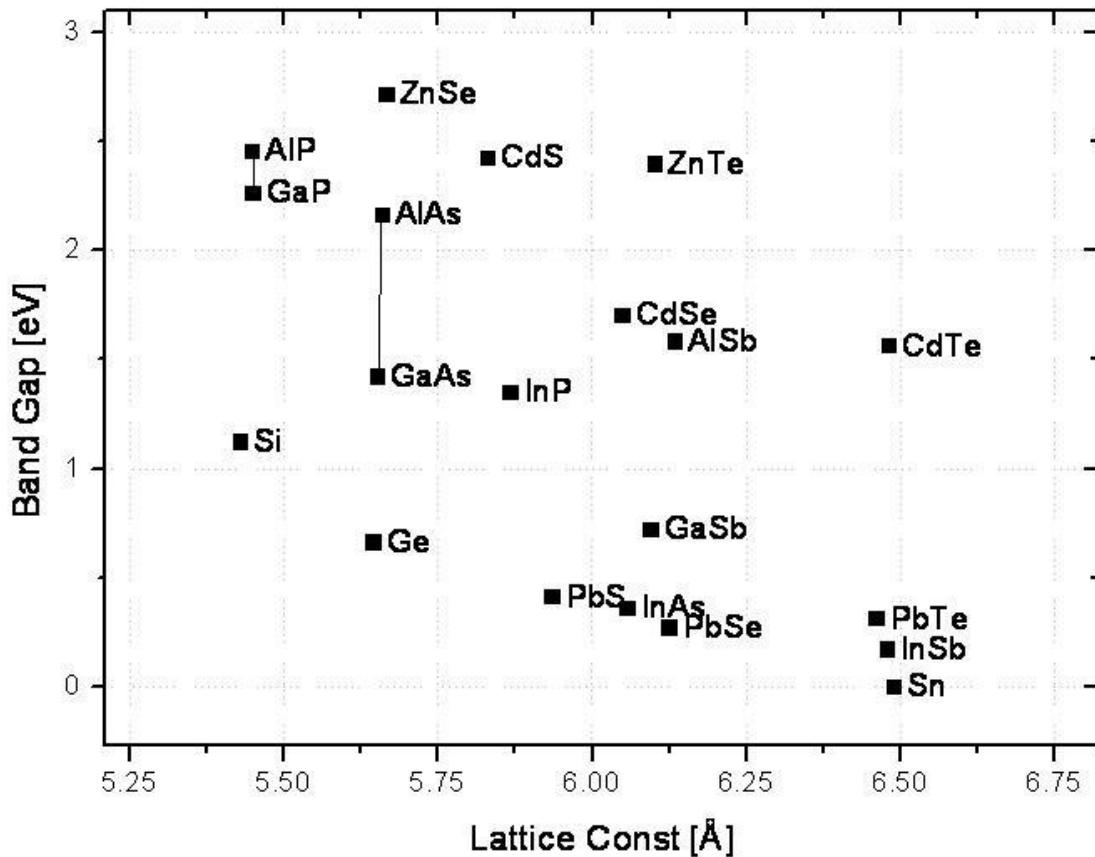


**Fig. 1.1.** The relationship between lattice constant and band gap for some common semiconductor compounds (Molhave, 2006). The lines connecting GaP and AlP, and GaAs and AlAs illustrate the values the band gap takes when varying the  $x$  fraction of  $Al_xGa_{1-x}P$  and  $Al_xGa_{1-x}As$  compounds, respectively.

The canny device designer can also select materials with a view to the intended application, as well as the intended environment. Sometimes materials can be selected so that the main absorption edges and fluorescence lines of the constituent elements of the semiconductor material are outside the X-ray energy region of interest. The K edges and fluorescence lines of gallium (Tables 1.1a & 1.1b) and arsenic (Tables 1.2a & 1.2b) are outside the main region of interest for planetary X-ray fluorescence spectroscopy ( $\sim 1$  keV –  $\sim 7$  keV). Consequently, when using a GaAs detector to obtain spectra for this application, correction of the spectra to take account of the internal

detector fluorescence from these lines is not required since they are outside the region of interest, unlike in the silicon K lines for silicon detectors (**Tables 1.3a & 1.3b**). At first glance it may appear as if no corrections for emission lines would be required in the region 1 keV to 7 keV, if a GaAs detector was used. However, the L edges and lines of gallium and arsenic are still within the spectral region of interest for planetary XRF and have significant fluorescence yields (**Tables 1.1a, 1.1b, 1.2a, 1.2b, 1.3a & 1.3b**), so spectra covering this region must still be corrected for these edges and lines.

	<b>L<sub>3</sub></b>	<b>L<sub>2</sub></b>	<b>L<sub>1</sub></b>	<b>K</b>
<b>Edge (keV)</b>	1.115	1.142	1.298	10.367
<b>Fluor. Yield</b>	0.013	0.012	0.002	0.543

*Table 1.1a. Gallium K and L X-ray edges and fluoresce yields (Brunetti et al., 2004).*

	<b>KL<sub>3</sub></b> <b>K<math>\alpha</math><sub>1</sub></b>	<b>KL<sub>2</sub></b> <b>K<math>\alpha</math><sub>2</sub></b>	<b>KM<sub>3</sub></b> <b>K<math>\beta</math><sub>1</sub></b>	<b>KM<sub>2</sub></b> <b>K<math>\beta</math><sub>3</sub></b>	<b>L<sub>1</sub>M<sub>3</sub></b> <b>L<math>\beta</math><sub>3</sub></b>	<b>L<sub>2</sub>M<sub>4</sub></b> <b>L<math>\beta</math><sub>1</sub></b>	<b>L<sub>3</sub>M<sub>5</sub></b> <b>L<math>\alpha</math><sub>1</sub></b>	<b>L<sub>3</sub>M<sub>1</sub></b> <b>Ll</b>
<b>Line energy (keV)</b>	9.252	9.225	10.264	10.260	1.197	1.125	1.098	0.957
<b>Radiative rate</b>	0.577	0.294	0.083	0.043	0.626	0.954	0.854	0.046

*Table 1.1b. Gallium X-ray fluorescence line energies and fractional radiative rates (Brunetti et al., 2004).*

	<b>L<sub>3</sub></b>	<b>L<sub>2</sub></b>	<b>L<sub>1</sub></b>	<b>K</b>
<b>Edge (keV)</b>	1.323	1.359	1.526	11.867
<b>Fluor. Yield</b>	0.016	0.014	0.003	0.581

*Table 1.2a. Arsenic K and L X-ray edges and fluorescence yields (Brunetti et al., 2004).*

	<b>KL<sub>3</sub></b> <b>K<math>\alpha</math><sub>1</sub></b>	<b>KL<sub>2</sub></b> <b>K<math>\alpha</math><sub>2</sub></b>	<b>KM<sub>3</sub></b> <b>K<math>\beta</math><sub>1</sub></b>	<b>KM<sub>2</sub></b> <b>K<math>\beta</math><sub>3</sub></b>	<b>L<sub>1</sub>M<sub>3</sub></b> <b>L<math>\beta</math><sub>3</sub></b>	<b>L<sub>2</sub>M<sub>4</sub></b> <b>L<math>\beta</math><sub>1</sub></b>	<b>L<sub>3</sub>M<sub>5</sub></b> <b>L<math>\alpha</math><sub>1</sub></b>	<b>L<sub>3</sub>M<sub>1</sub></b> <b>Ll</b>
<b>Line energy (keV)</b>	10.543	10.507	11.726	11.720	1.389	1.317	1.282	1.120
<b>Radiative rate</b>	0.571	0.294	0.086	0.044	0.607	0.957	0.857	0.042

*Table 1.2b. Arsenic X-ray fluorescence line energies and fractional radiative rates (Brunetti et al., 2004).*

	<b>L<sub>3</sub></b>	<b>L<sub>2</sub></b>	<b>L<sub>1</sub></b>	<b>K</b>
<b>Edge (keV)</b>	0.099	0.100	0.149	1.839
<b>Fluor. Yield</b>	0.000	0.000	0.000	0.048

**Table 1.3a.** Silicon K and L X-ray edges and fluorescence yields (Brunetti et al., 2004).

	<b>KL<sub>3</sub></b>	<b>KL<sub>2</sub></b>	<b>KM<sub>3</sub></b>	<b>KM<sub>2</sub></b>	<b>L<sub>1</sub>M<sub>3</sub></b>	<b>L<sub>2</sub>M<sub>4</sub></b>	<b>L<sub>3</sub>M<sub>5</sub></b>	<b>L<sub>3</sub>M<sub>1</sub></b>
	<b>Kα<sub>1</sub></b>	<b>Kα<sub>2</sub></b>	<b>Kβ<sub>1</sub></b>	<b>Kβ<sub>3</sub></b>	<b>Lβ<sub>3</sub></b>	<b>Lβ<sub>1</sub></b>	<b>Lα<sub>1</sub></b>	<b>Ll</b>
<b>Line energy (keV)</b>	1.740	1.739	1.836	1.836	-	-	-	0.094
<b>Radiative rate</b>	0.646	0.325	0.019	0.010	0.216	-	-	1.000

**Table 1.3b.** Silicon X-ray fluorescence line energies and fractional radiative rates (Brunetti et al., 2004).

A disadvantage of compound semiconductors is that often the material quality can be poorer than for elemental semiconductors. Owens and Peacock (2004) note that, due to charge trapping defects in the material, the charge transport properties (carrier mobility,  $\mu$ , or carrier lifetime,  $\tau$ ) of most semiconductor compounds are currently poor compared with silicon and germanium. For silicon and germanium, the product  $\mu\tau \geq 1$ , whereas for most compound semiconductors  $\mu\tau \sim 10^{-4}$  for electrons and  $\mu\tau \sim 10^{-5}$  for holes (e.g. for SiC  $\mu_e\tau_e = 4 \times 10^{-4} \text{ cm}^2/\text{V}^{-1}$  and  $\mu_h\tau_h = 8 \times 10^{-5} \text{ cm}^2/\text{V}^{-1}$ ) (Owens and Peacock, 2004). Unless the quality of compound semiconductor material can be improved, these comparably poor transport properties may limit the maximum thickness of compound semiconductor detectors. Growing thick, detector quality wafers can be difficult anyway due to lattice mismatches between the designer's preferred alloy and the available substrates (Gutiérrez et al., 2002) (Fuke et al., 1995) (Demeester et al., 1991). The thickness of the detector has a direct effect on the quantum efficiency of the device (see §2.2.1). Development of exotic compound semiconductor detectors is also often made difficult by lack of experimental data regarding even basic material properties of the different alloys.

This thesis concentrates on Al<sub>0.8</sub>Ga<sub>0.2</sub>As, GaAs and SiC compound semiconductor X-ray photodiodes. Prior to the research reported in this thesis, Lauter et al. (1995) had demonstrated X-ray detection with Al<sub>x</sub>Ga<sub>1-x</sub>As/GaAs (graded  $x$  from 0 to 0.45) separate absorption and multiplication regions (SAM) staircase APDs (Lauter et al., 1995) (Ripamoni et al., 1990) and published results of  $2 \times 2$  monolithic arrays made of similar

devices (Lauter et al., 1996). Silenas (2004), Silenas et al. (2002, 2003, 2005, 2006) and Dapkus et al. (2007) had reported results from graded-gap non-photon counting, non-spectroscopic  $\text{Al}_x\text{Ga}_{1-x}\text{As}/\text{GaAs}$  detectors that can detect changes in X-ray flux when operated in current mode, but had not demonstrated X-ray spectroscopy or photon counting with their devices.  $\text{Al}_{0.8}\text{Ga}_{0.2}\text{As}$   $\text{p}^+\text{-p}^-\text{-n}^+$  photodiodes, originally intended for use in telecommunications and grown and fabricated at the University of Sheffield had been shown to function as room temperature photon counting X-ray spectroscopic detectors in experiments at University of Leicester by Lees et al. (2008), but an artefact was present in the spectrum (see Chapter 6).

GaAs photon counting X-ray photodiodes have been reported operating at temperatures between  $+21\text{ }^\circ\text{C}$  and  $-16\text{ }^\circ\text{C}$  by Owens et al. (2001, 2002a) and Erd et al. (2002), but surprisingly no report has been made of the temperature dependence of the spectral resolution of GaAs photon counting X-ray photodiodes at higher temperatures.

The potential for SiC Schottky photodiodes to be used as high temperature photon counting spectroscopic X-ray detectors had also been previously recognised, most notably by Bertuccio, Casiraghi and Nava (2001) who were the first to report X-ray detection with SiC Schottky photodiodes. Subsequent work by Bertuccio (2005), Bertuccio & Casiraghi (2003), and Bertuccio et al. (2004a, 2004b, 2006, 2011), review by Nava et al. (2008), dominates the SiC X-ray photon counting spectroscopic detector literature. At University of Leicester, a novel type of SiC Schottky diode (the semi-transparent SiC Schottky diode – STSSD), fabricated at University of Newcastle, had also been shown to function as a photon counting spectroscopic X-ray detector in experiments at room temperature (Lees et al., 2007) (Lees et al., 2009).

## 1.5 Thesis organisation

Chapter 2 reviews the physics of X-ray detection with photodiodes and provides background on the theory of impact ionisation in X-ray photodiodes. Chapter 3 describes the Monte Carlo model developed to model X-ray detection in  $\text{Al}_{0.8}\text{Ga}_{0.2}\text{As}$  and GaAs  $\text{p}^+\text{-p}^-\text{-n}^+$  and  $\text{p}^+\text{-i-n}^+$  avalanche and non-avalanche photodiodes. Chapter 4 presents measurements and analysis characterising the performance of non-avalanche  $\text{Al}_{0.8}\text{Ga}_{0.2}\text{As}$  X-ray photodiodes at temperatures from  $+90\text{ }^\circ\text{C}$  to  $-30\text{ }^\circ\text{C}$ . Chapter 5 presents measurements and analysis of the performance of GaAs X-ray photodiodes at temperatures between  $+80\text{ }^\circ\text{C}$  and  $-30\text{ }^\circ\text{C}$ . Chapter 6 presents experimental and

computer modelling results which explain the origin of the additional peak anomaly reported by Lees et al. (2008) in their X-ray spectra taken with a  $p^+p^-n^+$  X-ray avalanche photodiode, and derives the temperature dependence of the impact ionisation coefficients in  $Al_{0.8}Ga_{0.2}As$  at a typical operating field. Chapter 7 reports high temperature X-ray spectrum measurements taken with semi-transparent SiC Schottky diodes. Chapter 8 offers overarching conclusions on the work and considers future directions for subsequent research.

## Chapter 2 Detector physics

### 2.1 Introduction

This chapter describes the physical principles of X-ray detection with photon counting non-avalanche photodiodes and photon counting avalanche photodiodes (APDs). The physics of soft X-ray attenuation and photoelectric X-ray absorption are reviewed, along with the basics of charge generation and transport in semiconductor detectors. The factors affecting the energy resolution of semiconductor detectors are discussed, and for avalanche photodiodes the impact ionisation process is reviewed with reference to the local model (McIntyre, 1966).

For further detail, various comprehensive introductions to X-ray detection with semiconductor devices exist, including Fraser (1989), Knoll (2000) and Owens & Peacock (2004).

### 2.2 X-ray attenuation

#### 2.2.1 Beer-Lambert law

Monochromatic X-rays incident on a material are attenuated through it (absorbed or scattered by it) according to the Beer-Lambert law (Potts, 1987):

$$I = I_0 e^{-\mu x} \quad (2.1)$$

where  $I$  is the intensity of the beam transmitted through the material,  $I_0$  is the original intensity of the beam,  $\mu$  is the linear attenuation coefficient for the material at the particular X-ray energy being investigated and  $x$  is the thickness of the material. It should be noted that the linear attenuation coefficient varies with the density of the material, even when the material stays the same. An absorber's linear attenuation coefficient,  $\mu$ , can be calculated from its mass attenuation coefficient,  $M$ , and density,  $\rho$  ( $\mu = M\rho$ ). If one wishes to detect a large fraction of the incident flux, it is desirable to maximise the absorption,  $I_0(1-e^{-\mu x})$ , by maximising  $\mu$  and  $x$ . The linear attenuation coefficient,  $\mu$ , is material dependent and can be maximised by selecting high  $Z$  (atomic number) detector materials. The thickness,  $x$ , can also be increased, but it cannot be

usefully increased indefinitely: it is limited by charge carrier mobility in the detector and the quality and thickness of the detector material that can be grown (Owens & Peacock, 2004).

For the soft X-ray energies ( $\sim 1 \text{ keV} - \sim 25 \text{ keV}$ ) of interest in this thesis, the dominant form of attenuation of the incident beam is photoelectric absorption (§2.2.2). For a consideration of Compton scattering and pair-production see Knoll (2000).

### 2.2.2 Photoelectric absorption

In photoelectric absorption, an incident X-ray photon interacts with one of the detector's atoms. The photon ionizes the atom, liberating an electron. The incident photon's energy is transferred to the atom's electron, less the binding energy of that electron in its original shell. The vacancy is filled by the capture of a free electron from the material or by rearrangement of the atom's electronic structure. This rearrangement can occur either by fluorescence, the Auger effect or both, since vacancies can cascade through the shells.

When an atom rearranges by emitting a fluorescence photon, this photon is either absorbed by the detector or escapes. When a fluorescence photon of energy,  $E_{flu}$ , escapes, this gives rise to an escape peak of energy,

$$E_{esc} = E - E_{flu} \quad (2.2)$$

in the spectrum, where  $E$  is the initial X-ray photon's energy. If only the fluorescence photon is absorbed (e.g. if the original X-ray photon was absorbed in a non-active region of the detector), an elemental characteristic fluorescence peak can be visible in the spectrum. Photoelectrons and Auger electrons have a sufficiently short range that they can be considered to be localised to the point of X-ray absorption for the detectors in this thesis.

### 2.2.3 Absorption edges

Plots of the linear absorption coefficients for GaAs,  $\text{Al}_{0.8}\text{Ga}_{0.2}\text{As}$ , SiC and Si as functions of X-ray energy are shown in **Fig. 2.1**. Whilst there is a general trend for the attenuation coefficient to decrease exponentially as the energy of the incident X-ray increases, there are discontinuities, known as absorption edges, at energies equal to the binding energies of the electrons in the material (for the energy range plotted, for GaAs,

these are the elements' K and L edges). Absorption edges have the effect that a photon of energy just more than an edge has a higher probability of being absorbed than a photon with an energy just below the absorption edge. The absorption edges result from the different binding energies of the electrons in different shells; when a photon has an energy greater than the binding energy of an electron in a given shell, the photon is more likely to be absorbed by the atom because the photon has sufficient energy to liberate electrons in that shell as well as the lower energy shells.

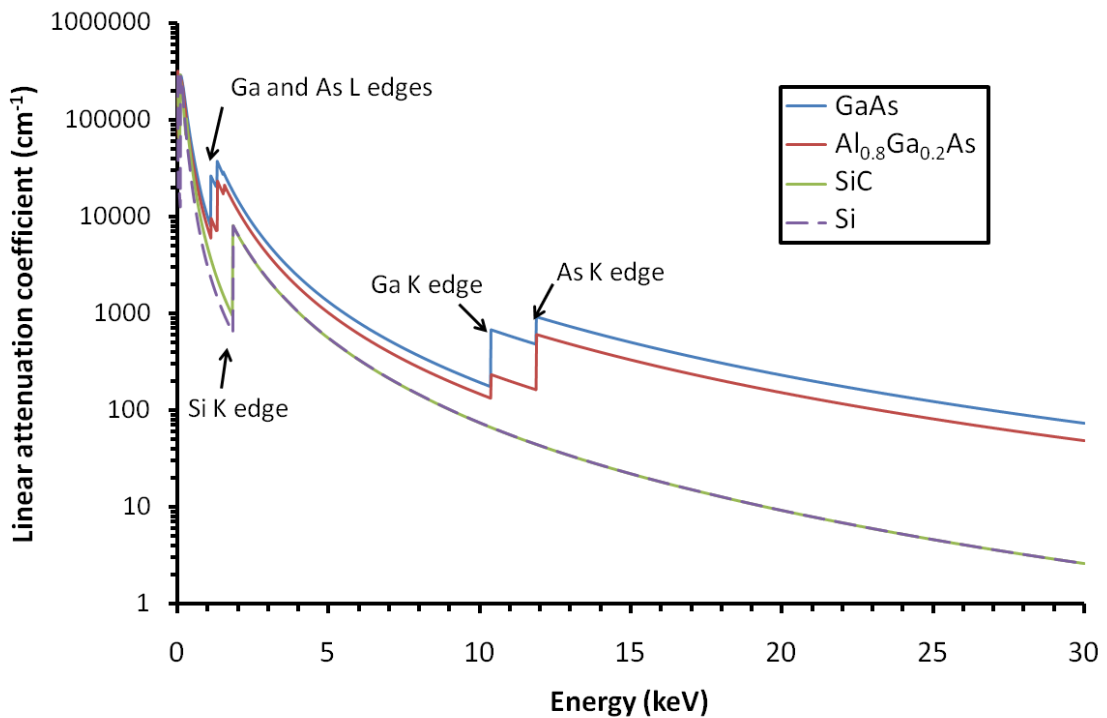


**Fig. 2.1.** The energy dependence of the linear attenuation coefficients for GaAs (blue line),  $Al_{0.8}Ga_{0.2}As$  (red line), SiC (green line), and Si (dashed purple line). The discontinuities are the absorption edges (see *Tables 1.1a, 1.2a & 1.3a*).

### 2.3 Diode structure

In order to collect efficiently the charge carriers generated by the absorption of an X-ray photon, it is necessary to apply an electric field across the semiconductor detector (§2.5). In order to minimise the device leakage current (§2.6.2) resulting from this electric field, reverse biased semiconductor junctions are used rather than simple crystals of intrinsic semiconductor material. A diode is reverse biased when a negative voltage is applied to the diode's p layer, with respect to its n layer (see below). This reverse biasing has the effect of increasing the natural potential difference between the p and n layers, and causes electrons to be attracted to the n layer and holes to the p layer.

The GaAs and  $\text{Al}_{0.8}\text{Ga}_{0.2}\text{As}$  diodes described in this thesis are based on circular (diameter = 200  $\mu\text{m}$ ) mesa  $\text{p}^+\text{-i-n}^+$  and  $\text{p}^+\text{-p-n}^+$  junctions, which have highly doped  $\text{p}^+$  and  $\text{n}^+$  layers (see **Tables 4.1, 5.1 & 6.1** for layer properties) either side of an intrinsic (or near intrinsic) layer; see **Fig. 2.2** for a simplified schematic diagram, **Fig. 2.3** for a scanning electron microscope photograph, and Chapters 4, 5 and 6. The SiC devices are square (250  $\mu\text{m} \times 250 \mu\text{m}$ ) 4H-SiC semi-transparent Schottky diodes, with an epitaxial n layer and a semi-transparent Schottky contact grown on a 4H-SiC  $\text{n}^+$  substrate (see **Fig. 2.4** and Chapter 7). Schottky diodes consist of a Schottky barrier metal-semiconductor junction rather than semiconductor-semiconductor junctions, as in p-n,  $\text{p}^+\text{-p}^-\text{-n}^+$  or  $\text{p}^+\text{-i-n}^+$  diodes.

The areas of the GaAs,  $\text{Al}_{0.8}\text{Ga}_{0.2}\text{As}$  and SiC diodes reported in this thesis are small compared with some silicon photodiodes (e.g. diameter > 3 mm, (Kataoka et al., 2005)) but diodes of comparable area to those reported in this thesis may find use in pixel array detectors and larger GaAs,  $\text{Al}_{0.8}\text{Ga}_{0.2}\text{As}$  and SiC devices are planned to be fabricated in future (see Chapter 8).

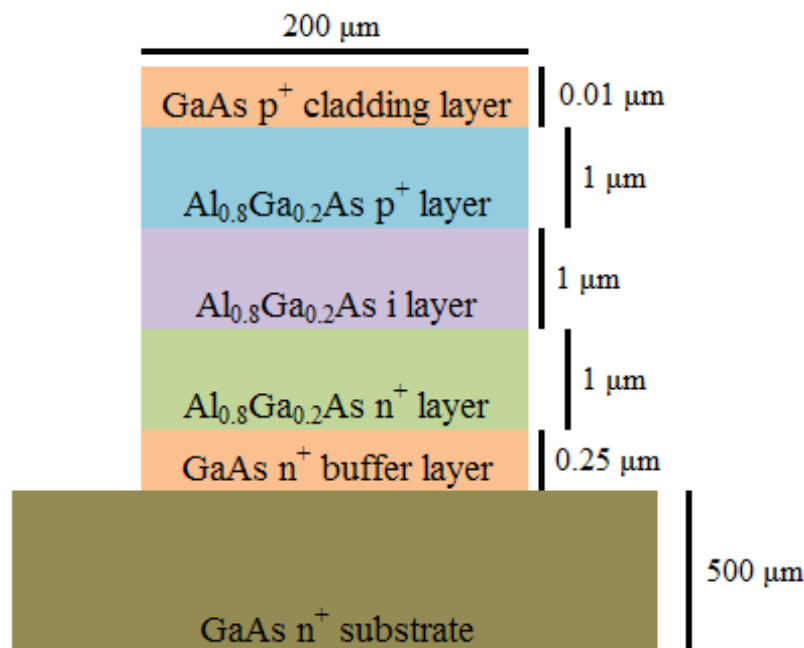


**Fig. 2.2.** A simplified schematic cross-section diagram depicting the  $\text{Al}_{0.8}\text{Ga}_{0.2}\text{As}$   $\text{p}^+\text{-i-n}^+$  diodes used in Chapter 4 (not to scale).

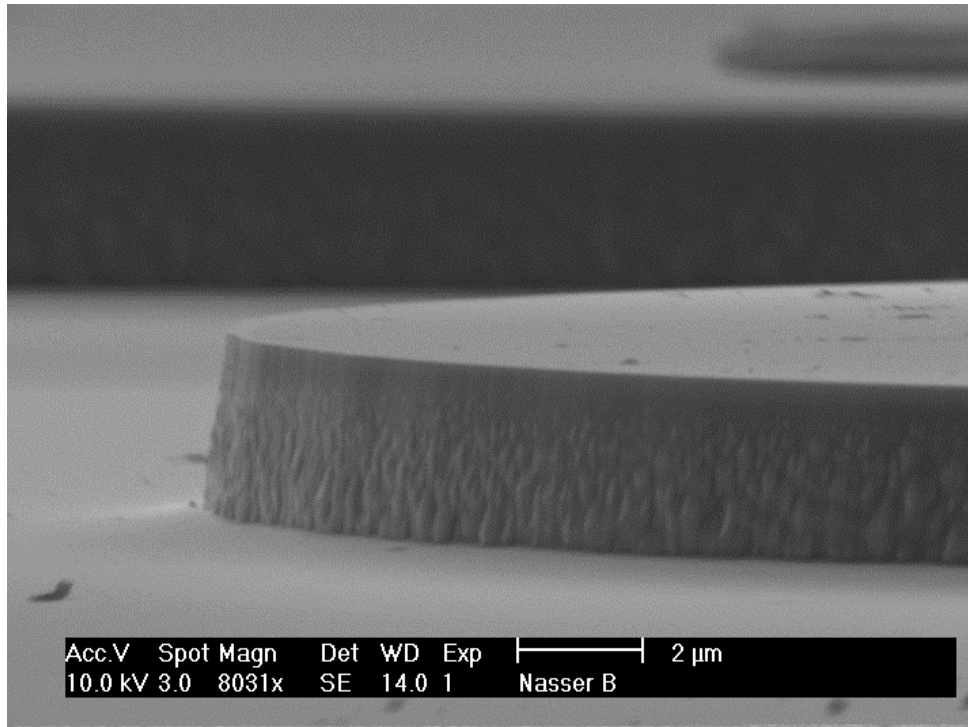


**Fig. 2.3.** A GaAs diode of the sort used in Chapter 5 seen through a scanning electron microscope. Image courtesy of Dr N. Babazadeh, Department of Electronic and Electrical Engineering, University of Sheffield, UK.

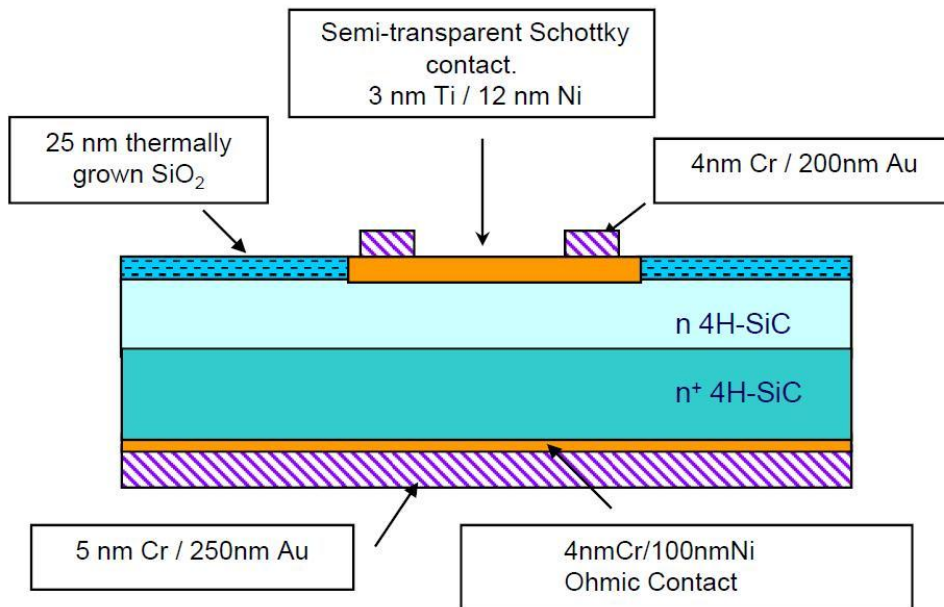


**Fig. 2.4.** A simplified schematic cross-section of a semi-transparent SiC Schottky diode (not to scale). The substrate is the  $n^+$  4H-SiC region (doping density =  $2 \times 10^{18} \text{ cm}^{-3}$ ). The epitaxial layer is the  $n$  4H-SiC region (doping density =  $7.7 \times 10^{14} \text{ cm}^{-3}$ ) (Lees et al., 2011).

In a  $p^+ - i - n^+$  diode, the depletion (high field) region thickness is, to a first approximation, simply the thickness of the  $i$  layer. There can be some small extension of the depletion region into the  $p^+$  and  $n^+$  layers as a consequence of the applied electric field but the high doping concentrations of the  $p^+$  and  $n^+$  layers typically make this negligible compared to the width of the  $i$  layer. The total thickness,  $D_T$ , of the depletion region in a  $p^+ - i - n^+$  diode including any extension into the  $p^+$  and  $n^+$  layers is given by

$$D_T = \left[ w^2 + \frac{2\varepsilon_s(N_p + N_n)}{q(N_p N_n)} V \right]^{1/2} \quad (2.3)$$

where  $w$  is the thickness of the  $i$  layer,  $\varepsilon_s$  is the static permittivity of the diode material,  $q$  is the charge on an electron,  $N_p$  and  $N_n$  are the doping concentrations in the  $p^+$  and  $n^+$  layers, and  $V$  is the potential difference (reverse bias) across the diode (Van Zeghbroeck, 2007). Conversely, in a Schottky diode, the thickness of the depletion region is very dependent upon the reverse bias (there is no  $i$  layer), and it is given by

$$D_T = \left[ \frac{2\varepsilon_s V}{qN} \right]^{1/2} \quad (2.4)$$

where  $\varepsilon_s$ ,  $V$ , and  $q$  have been previously defined, and  $N$  is the doping density in the epitaxial layer.

## 2.4 Charge generation

The average number of electron-hole pairs,  $N_{EHP}$ , created by the absorption of an initial X-ray photon is given by

$$N_{EHP} = E / \omega_{EHP} \quad (2.5)$$

where  $E$  is the initial X-ray photon's energy and  $\omega_{EHP}$  is the average electron-hole pair creation energy, which for  $\text{Al}_{0.8}\text{Ga}_{0.2}\text{As} = 5.25$  eV (NSM Archive, 2004). However, while Eq. 2.5 gives the average number of electron-hole pairs created for photons of energy  $E$ , in actuality the number of electron-hole pairs created is subject to random variation from one photon absorption event to the next. Assuming that the process of creating electron-hole pairs is Poissonian, the variability as quantified by the standard deviation,  $\sigma$ , of the distribution of  $N_{EHP}$ , is  $\sqrt{N_{EHP}}$ . Since the number of electron-hole pairs is typically large at X-ray energies (see Eq. 2.5), a Gaussian distribution (FWHM =  $2.35\sigma$ ) results, which, assuming there are no other factors affecting the fluctuations in

measured charge, suggests a fundamental, Poissonian charge resolution  $\left(\frac{\text{FWHM of } N_{EHP} \text{ distribution}}{\text{Modal } N_{EHP}}\right)$  limit of

$$R_{Poisson} = \frac{2.35}{\sqrt{N_{EHP}}}. \quad (2.6)$$

Eq. 2.6 shows that this limit depends on the number of electron-hole pairs created, with larger  $N_{EHP}$  leading to improved statistics and resolution. Consequently, it is desirable for detectors to have as many electron-hole pairs generated as possible per photon absorbed, to make  $R_{Poisson}$  as small as possible.

However, it has been experimentally shown that the processes by which each individual electron-hole pair is generated are not independent (Fano, 1947). Consequently the variation in  $N_{EHP}$  cannot be fully quantified by Poissonian statistics. The observed deviation in number of electron-hole pairs (charge carriers) created, from that predicted by Poissonian statistics, is quantified by the Fano factor (Fano, 1947),  $F$ , as

$$F \equiv \frac{\text{Observed variance in } N}{\text{Poisson predicted variance in } N}. \quad (2.7)$$

Typical values of  $F$  in semiconductors are around 0.12 (**Table 2.1**) and  $F$  is bounded by 0 and 1. This modifies Eq. 2.6, to give the fundamental statistical resolution  $\left(\frac{\text{FWHM of } N_{EHP} \text{ distribution}}{\text{Modal } N_{EHP}}\right)$  ‘‘Fano’’ limit as

$$R_{Fano} = 2.35 \sqrt{\frac{F}{N_{EHP}}} \quad (2.8)$$

with the FWHM of the distribution as

$$\text{FWHM [electron-hole pairs]} = 2.35 \sqrt{\frac{FE}{\omega_{EHP}}} \quad (2.9)$$

and the variance,  $\sigma^2$ , as

$$\sigma^2 = FN_{EHP} = \frac{FE}{\omega_{EHP}}. \quad (2.10)$$

This gives the fundamental statistically limited energy resolution (FWHM, in eV) of a semiconductor detector as

$$\text{FWHM [eV]} = 2.35\omega_{EHP}\sqrt{\frac{FE}{\omega_{EHP}}}. \quad (2.11)$$

## 2.5 Charge transport

The negatively charged electrons and positively charged holes can move in semiconductors under the influence of an electric field. The electron and hole velocities,  $v_e$  and  $v_h$  respectively, in a uniform electric field of strength  $E_d$ , are given by

$$v_e = \mu_e E_d \quad (2.12a)$$

$$v_h = \mu_h E_d \quad (2.12b)$$

where  $\mu_e$  and  $\mu_h$  are the electron and hole mobilities. The motion of charge carriers through a semiconductor is impeded by charge carrier trapping and recombination, caused by impurities and defects in the semiconductor material (Owens & Peacock, 2004). Trapping centres may immobilise charge carriers for longer than the read out time of the detector, and recombination centres may capture both an electron and a hole causing them to recombine. This restricts the lifetimes of the electrons and holes,  $\tau_e$  and  $\tau_h$ . Both processes can cause a reduction in the measured charge, and trapping can cause a second burst of charge to be recorded from the detector when charge carriers are released. The recombination lengths, the average distances electrons and holes can travel without being lost,  $r_e$  and  $r_h$  respectively, are given by

$$r_e = \mu_e \tau_e E_d \quad (2.13a)$$

$$r_h = \mu_h \tau_h E_d \quad (2.13b)$$

where all the symbols have been previously defined. The recombination lengths limit the useful thickness of a detector, since any charge carriers generated beyond one recombination length from an electrode do not contribute to the total detected charge.

The charge carrier mobilities are similar and high for electrons and holes in silicon (**Table 2.1**). However, most compound semiconductors suffer from poor mobility of one or both charge carrier types, or short charge carrier lifetimes. A table of properties for some common semiconductor materials is given in **Table 2.1**, details for other compound semiconductors can be found in Owens & Peacock (2004).

Parameter	Si	4H-SiC	GaAs	Al <sub>0.8</sub> Ga <sub>0.2</sub> As	Cd <sub>0.9</sub> Zn <sub>0.1</sub> Te	CVD Diamond
Density (g cm <sup>3</sup> )	2.33	3.21	5.32	4.07	5.78	3.515
Mean atomic number	14	10	31.5	24.8	49.1	6
Band gap (eV)	1.12	3.26	1.43	2.09	1.572	5.46-5.6
Pair creation energy (eV)	3.62	7.8	4.2	5.25	4.64	7.8
Electron Mobility (cm <sup>2</sup> V <sup>-1</sup> s <sup>-1</sup> )	1400	1000	8000	1000	1000	2200
Hole Mobility (cm <sup>2</sup> V <sup>-1</sup> s <sup>-1</sup> )	1900	115	400	-	120	1800
Electron Lifetime (s)	>10 <sup>-3</sup>	5 × 10 <sup>-7</sup>	10 <sup>-8</sup>	-	3 × 10 <sup>-6</sup>	10 <sup>-9</sup> - 10 <sup>-10</sup>
Hole Lifetime (s)	10 <sup>-3</sup>	7 × 10 <sup>-7</sup>	10 <sup>-7</sup>	-	1 × 10 <sup>-6</sup>	5 × 10 <sup>-11</sup>
Electron μτ product (cm <sup>2</sup> V <sup>-1</sup> )	>1	4 × 10 <sup>-4</sup>	8 × 10 <sup>-5</sup>	-	4 × 10 <sup>-3</sup>	2 × 10 <sup>-5</sup>
Hole μτ product (cm <sup>2</sup> V <sup>-1</sup> )	~1	8 × 10 <sup>-5</sup>	4 × 10 <sup>-6</sup>	-	1.2 × 10 <sup>-4</sup>	8 × 10 <sup>-8</sup>
Lattice constant (Å)	5.431	a = 3.073 c = 10.053	5.653	5.659	6.44	3.567
Fano Factor	0.116	0.100	0.12	-	0.099	0.08 (predicted)

**Table 2.1.** Indicative values of properties for some common intrinsic semiconductor materials, (Adachi, 1985), (Franklin et al., 1992), (Salvatori et al., 1999), (Owens et al., 2002b), (Bertuccio & Casiraghi, 2003), (Marinelli et al., 2004), (Owens & Peacock, 2004), (Sridharan et al., 2004), (Alig et al., 1980), (Kashiwagi et al., 2006), (Bertuccio et al., 2011). Reliable measurements of some parameters for Al<sub>0.8</sub>Ga<sub>0.2</sub>As are yet to be reported.

## 2.6 Energy resolution and noise sources

### 2.6.1 Introduction

The ability to measure characteristic X-ray lines is the essence of X-ray spectroscopy. The spectroscopic (energy) resolution of an X-ray detector is of basic importance since it describes how close two X-ray lines can be in energy terms and still be distinguishable from each other. A better (smaller) energy resolution allows X-ray lines that are closer in energy to be separated more clearly.

### 2.6.2 The energy resolution of a semiconductor detector

The fundamental (statistically limited) FWHM energy resolution of a semiconductor X-ray detector (Eq. 2.11) is degraded by noise terms,  $R$  &  $A$ , defined below, which cause the detector's FWHM, expressed in eV, to become

$$\Delta E [\text{eV}] = 2.35\omega_{EHP} \sqrt{\frac{FE}{\omega_{EHP}} + R^2 + A^2} . \quad (2.14)$$

The factor  $R$  is the equivalent noise charge (in r.m.s.  $e^-$ ) introduced by the detector during the movement of the charge to the contacts (e.g. by charge trapping), and  $A$  is the equivalent noise charge (in r.m.s.  $e^-$ ) introduced by the detector's leakage current and pre-amplifier (Fraser, 1989). It is desirable to minimise  $R$  and  $A$ , in order to improve the resolution of the detector; when  $R$  and  $A$  are negligible, the spectral resolution is said to be Fano limited.

Where charge trapping is the primary source of noise contributing to charge read out noise,  $R$  has the form

$$R = \frac{k_1 E^{k_2}}{(2.35\omega_{EHP})^2} \quad (2.15)$$

where  $k_1$  and  $k_2$  are empirically derived constants. However,  $R$  is small compared with  $A$  for most modern semiconductor crystals (Owens & Peacock, 2004).

A comprehensive introduction to the various electronic noise sources contributing to  $A$  in photon counting X-ray photodiodes coupled to charge sensitive preamplifiers can be found in Bertuccio, Pullia & DeGeronimo (1996), the salient points of which are summarised below to give expressions for the parallel white noise (§2.6.3), series white noise (§2.6.4),  $1/f$  series noise (§2.6.5), dielectric noise (§2.6.6) and induced gate current noise (§2.6.7) contributions.

### 2.6.3 Parallel white noise

Parallel white noise stems from the shot noise of the currents flowing through the input node of the preamplifier. It is primarily dependent on the leakage currents of the detector,  $I_{LD}$ , and the preamplifier input field effect transistor (JFET),  $I_{LT}$  (Bertuccio, Pullia, DeGeronimo, 1996).

The parallel white noise power spectral density,  $S_{PW}$ , can be expressed as

$$S_{PW} = 2q(I_{LD} + I_{LT}) + \frac{4kT}{r} \quad (2.16)$$

where  $q$  is the charge on an electron ( $1.602 \times 10^{-19}$  C),  $k$  is the Boltzmann constant,  $T$  is the temperature (in K) and  $r$  is the resistance of the preamplifier feedback resistor if the preamplifier has one (Bertuccio, Pullia, DeGeronimo, 1996). The preamplifier used for the measurements reported in this thesis does not have a feedback resistor so the  $\frac{4kT}{r}$  term is omitted. The contribution (measured in r.m.s.  $e^-$ ) of  $S_{PW}$  to the equivalent noise charge  $A$  (Eq. 2.14), is

$$N_{PW} = \frac{1}{q} \sqrt{(A_3/2)S_{PW}\tau} \quad (2.17)$$

where  $A_3$  is a constant dependent on signal shaping function (Gatti et al. 1990), and  $\tau$  is the shaping time. The leakage currents of the detector and JFET are therefore important in determining the limits of spectral resolution of the detector.

Whilst  $N_{PW}$  is not directly dependent on the capacitance of the preamplifier input JFET, it can be beneficial to reduce the JFET capacitance as this reduces the optimum shaping time,  $\tau$ , which does reduce  $N_{PW}$  (Bertuccio, Pullia & DeGeronimo, 1996).

#### 2.6.4 Series white noise

The series white noise primarily arises from the effect of thermal noise on the drain current of the input JFET (Bertuccio, Pullia & DeGeronimo, 1996). When secondary sources (e.g. stray resistance in series with the input JFET's gate) are negligible, the series white noise power spectral density,  $S_{SW}$ , can be approximated to the thermal noise of the JFET drain current:

$$S_{SW} = \gamma \frac{4kT}{g_m} \quad (2.18)$$

where  $0.7 \leq \gamma \leq 1$  depending on JFET characteristics, and  $g_m$  is the transconductance of the JFET. The contribution (measured in r.m.s.  $e^-$ ) of  $S_{SW}$  to the equivalent noise charge (Eq. 2.14) is

$$N_{SW} = \frac{1}{q} \sqrt{(A_1/2)S_{SW}C_T^2(1/\tau)} \quad (2.19)$$

where  $A_1$  is a constant depending on signal shaping function (Gatti et al., 1990) and  $C_T$  is the total capacitance at the preamplifier input ( $= C_d + C_i + C_f + C_s$ , where  $C_d$  is the

detector capacitance,  $C_i$  is the input transistor capacitance,  $C_f$  is the feedback capacitance and  $C_s$  is the stray capacitance) (Bertuccio, Pullia & DeGeronimo, 1996). The equivalent noise charge contribution  $N_{SW}$  becomes increasingly significant at shorter shaping times because of the  $1/\tau$  dependence.

### 2.6.5 $1/f$ series noise

The noise from the drain current of the preamplifier input JFET is also the main constituent of  $1/f$  series noise. The  $1/f$  noise contribution to the equivalent noise charge  $A$  (Eq. 2.14) is

$$N_{1/f} = \frac{1}{q} \sqrt{A_2 \pi A_f C_T^2} \quad (2.20)$$

where  $A_f$  is a characteristic constant dependent on the JFET and  $A_2$  is a constant ranging from 0.64 to 2 depending on signal shaping function (Gatti et al., 1990) (Bertuccio, Pullia & DeGeronimo, 1996).

### 2.6.6 Dielectric noise

Dielectrics in close proximity to the preamplifier, such as the packaging of the JFET and detector contribute

$$N_D = \frac{1}{q} \sqrt{A_2 2kTD C_{die}} \quad (2.21)$$

to the total electronics equivalent noise charge,  $A$ , where  $C_{die}$  is the capacitance of the dielectrics,  $D$  is the dielectrics dissipation factor (Bertuccio, Pullia & DeGeronimo, 1996) and  $q$ ,  $A_2$ ,  $k$  and  $T$  have all been previously defined. It is therefore desirable to design the input JFET and detector packaging to minimise exposure to dielectrics, for example by reducing the capacitance of the JFET and detector assembly by integrating the JFET onto the detector.

### 2.6.7 Induced gate current noise

Drain current noise (§2.6.4) causes charge fluctuations in the JFET gate current giving rise to the induced gate current noise. The contribution from this to  $A$  is dependent on  $S_{SW}$  (Eq. 2.18). Like the series white noise, the induced gate current noise becomes important at short shaping times because of the  $1/\tau$  dependence. Experimental

investigation has shown that Eq. 2.18 can be modified by a factor,  $G_c$ , ( $\sqrt{G_c} \approx 0.8$ ) to take account of the noise in the JFET's gate (Bertuccio, Pullia & DeGeronimo, 1996):

$$S_{SWC} = S_{SW}G_c. \quad (2.22)$$

Consequently the ENC contribution to  $A$  becomes

$$N_{SWC} = \frac{1}{q} \sqrt{(A_1/2)S_{SW}G_c C_T^2 (1/\tau)} = N_{SW} \sqrt{G_c}. \quad (2.23)$$

### 2.6.8 Electronic noise sources in combination

When considered together, the parallel white (§2.6.3) and series (§2.6.4) noise contributions' dependences on  $\tau$  and  $1/\tau$  respectively, can give rise to an optimum shaping time which minimises the combined noise from these sources (Pullia & Bertuccio, 1996). In §4.6.2 and §5.5.2, it is shown how the parallel white, series white,  $1/f$  and dielectric noises combine to produce the overall measurement ENC of a preamplifier and how this is effected by varying the shaping time,  $\tau$ .

## 2.7 Impact ionisation

### 2.7.1 Introduction

Avalanche photodiodes (APDs) – photodiodes in which impact ionisation occurs – are widely used in photonic detection systems (for compound semiconductors most notably in telecommunications (Campbell, 2007) (David & Tan, 2008)) to increase the system's signal to noise ratio, with the charge from each detected event being multiplied by the multiplication factor,  $M$ , of the APD. The multiplication factor depends on the position,  $x$ , at which the initial electron-hole pairs are created within (or injected to) the avalanche region, the charge carrier ionisation coefficients which are material specific, the electric field,  $E$ , and the temperature,  $T$ , of the diode.

Avalanche multiplication occurs when charge carriers created by a photon absorption event gain sufficient kinetic energy from being accelerated by the electric field in a diode to cause the generation of additional charge carriers upon their interaction with a lattice atom.

In the case of a conduction band electron which was generated by the absorption of a photon in the device, the electron is accelerated toward the  $n^+$  contact, gaining kinetic

energy as it travels. When this energetic electron interacts with a lattice atom, some of the electron's energy is transferred to that atom, promoting one of the atom's higher energy valence band electrons into the conduction band. This newly promoted conduction electron necessarily creates a hole upon leaving its valence band position. The electron of the electron-hole pair created by the absorption of the photon, together with the newly created (by impact ionisation) electrons and holes are then accelerated through the device by the electric field in the same manner as before (electrons toward the  $n^+$  contact and holes toward  $p^+$  contact). Both the charge carriers of the electron-hole pairs liberated by the absorption of the photon, and the charge carriers created by impact ionisation of those initial charge carriers, are free to impact ionise with lattice atoms and generate more charge carriers once they have gained sufficient energy. This chain of events is avalanche multiplication (avalanche gain) and can be repeated many times with many impact ionisation events taking place before the charge carriers reach their respective destination boundaries.

There are various structural forms of APD, including simple  $p^+ - i - n^+$  (or  $p^+ - p - n^+$ ) devices (Lees et al., 2008) (the APD structure considered in this thesis, see Chapter 6), and separate absorption and multiplication region (SAM) or 'reach-through' devices, which have their depletion regions separated into two regions: a low-field drift region (typically of low doping) for the absorption of photons and one or more high-field regions (typically p-n junctions) where avalanche multiplication takes place (**Fig. 2.5**) (Ruegg, 1967), (Ochi et al., 1996), (Yatsu et al., 2006). The drift region is much thicker than the multiplication region leading to the majority of the incident photons being absorbed in the drift region. The charge carriers attracted to the multiplication region (electrons for a p-i-p-n type device, as shown in **Fig. 2.5**) all enter the multiplication region at the same position and consequently receive the same multiplication (§2.7.3). This is in contrast to APDs of simple design (where the absorption region is also the multiplication region); here the multiplication factor depends on the position,  $x$ , at which the initial electron-hole pairs are created.

The X-ray photon counting APDs reported in the literature are dominated by silicon devices e.g. (Squillante et al., 1985), (Farrell et al., 1991), (Ochi et al., 1996), (Yatsu et al., 2006), although there have also been reports of  $Al_xGa_{1-x}As$  and GaAs APDs e.g. (Lees et al., 2008), (Lauter et al., 1995) (Lauter et al., 1996).

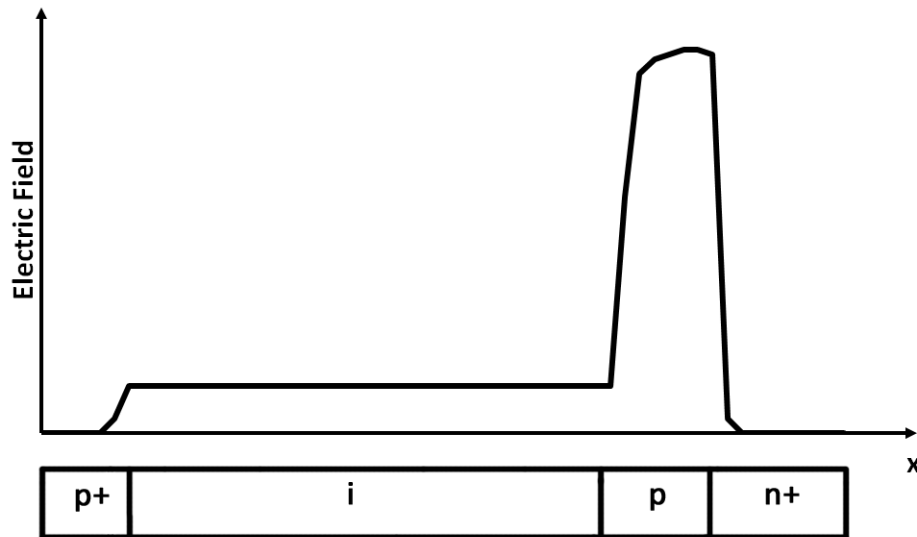


Fig. 2.5. An illustrative field profile in a  $p^+ - i - p - n^+$  SAM diode (see text).

### 2.7.2 Background theory

The number of charge carriers generated through impact ionisation is dependent upon the number of times that impact ionisation can occur before all charge carriers reach the end of the high field region. The number of charge carriers generated by impact ionisation can be different for electron and hole initiated avalanches. Stronger electric fields within the device result in charge carriers obtaining the necessary energy to impact ionise over a shorter distance and consequently more charge carriers can be generated in devices operated at high electric field. The distance that charge carriers must travel between impact ionisation events (the ionisation path length) is not constant because the impact ionisation process is stochastic (i.e. random within the bounds of the probability distributions) (see §2.7.4). The electron,  $\alpha$ , and hole,  $\beta$ , ionisation coefficients are the reciprocal of the average distance each charge carrier type must travel between impact ionisation events. At sufficiently high fields, the number of impact ionisation generated electrons and holes can increase very rapidly causing the device to suffer avalanche breakdown.

The ionisation coefficients of a material are assumed in the local model (McIntyre, 1966), to be dependent only upon the electric field and temperature in the device. Conventionally, it is assumed that the ionisation coefficients are constant throughout the material, and that differences in the multiplication experienced by charge carriers of the same type are solely due to their starting position and not the charge carrier's history (McIntyre, 1966). This local model assumption is generally assumed to be valid when

the width,  $w$ , of the avalanche region is significantly larger than the electron,  $d_e$ , and hole,  $d_h$ , dead spaces (Plimmer, 1996) (Tan et al., 2001) (Ng et al., 2002). The electron and hole dead spaces are the minimum distance that each type of charge carrier must travel to gain the minimum (threshold) energy ( $E_{The}$  and  $E_{Thh}$ , for electrons and holes respectively) required to impact ionise. The values of  $d_e$  and  $d_h$  are dependent on the electric field in the avalanche region and scattering processes associated with the movement of the charge carriers (Childs & Leung, 1991). The time it takes each type of charge carrier to travel the dead space for each carrier type is termed the dead time ( $\tau_{de}$  and  $\tau_{dh}$ , for electrons and holes respectively).

Since the impact ionisation process is dependent upon the electric field, and the field profile in a diode can be engineered by doping controls and layering, the region in which charge carriers can impact ionize can be restricted by suitable layer doping arrangements. In a reverse biased, idealised  $p^+i-n^+$  APD, the central  $i$  layer is the avalanche region, since it is the high field layer and consequently charge carriers within it are subject to avalanche multiplication if the electric field generated by the applied reverse bias is sufficiently large.

### 2.7.3 Multiplication factors

Assuming a local model (McIntyre, 1966), for a given temperature, the multiplication factor,  $M$ , as a function of photon absorption position,  $x$ , in the  $i$  layer, in an ideal  $p^+i-n^+$  diode of  $i$  layer width,  $w$ , and where the  $p^+i$  boundary is defined as  $x = 0$  (**Fig. 2.6**), is

$$M(x) = \frac{(\alpha - \beta)e^{-(\alpha - \beta)x}}{\alpha e^{-(\alpha - \beta)w} - \beta} . \quad (2.24)$$

For pure (maximum) electron initiated multiplication, which occurs when photons are absorbed at the  $p^+i$  boundary,  $x = 0$ , Eq. 2.24 becomes

$$M_e = \frac{\alpha - \beta}{\alpha e^{-(\alpha - \beta)w} - \beta} . \quad (2.25)$$

For pure (maximum) hole initiated multiplication, which occurs when photons are absorbed at the  $n^+i$  boundary,  $x = w$ , Eq. 2.24 becomes

$$M_h = \frac{(\alpha - \beta)e^{-(\alpha - \beta)w}}{\alpha e^{-(\alpha - \beta)w} - \beta} . \quad (2.26)$$

When photon absorption is not confined to an  $i$  layer boundary, avalanche multiplication is a mixture of electron and hole initiated avalanche. The mixed multiplication factor ( $M_{mix}$ ) is given by

$$M_{mix} = \frac{\int_0^w M(x)G(x)dx}{\int_0^w G(x)dx} \quad (2.27)$$

where  $G(x)$  is the distribution of photon absorption through the  $i$  layer.

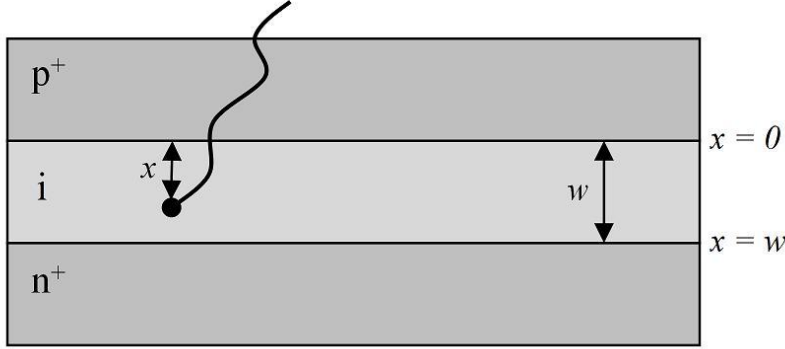


**Fig. 2.6.** Schematic cross-sectional diagram of a  $p^+ - i - n^+$  diode with the position of photon absorption,  $x$ , width of  $i$  layer,  $w$ , and the  $p^+ - i$  and  $i - n^+$  boundaries marked.

Just as the electron,  $\alpha$ , and hole,  $\beta$ , impact ionisation coefficients can be used to derive the multiplication factors, measurements of the multiplication factors can also be used to derive the ionisation coefficients:

$$\alpha = \frac{1}{w} \left( \frac{M_e - 1}{M_e - M_h} \right) \ln \left( \frac{M_e}{M_h} \right) \quad (2.28)$$

$$\beta = \frac{1}{w} \left( \frac{M_h - 1}{M_h - M_e} \right) \ln \left( \frac{M_h}{M_e} \right). \quad (2.29)$$

#### 2.7.4 Excess noise factor

Variation in the ionisation path length leads to variation in the multiplication factor achieved for the charge carriers of each electron-hole pair for a given photon absorption position. The excess noise factor,  $N_{XS}$ , quantifies the variation that arises in multiplication factor due to the stochastic nature of the impact ionisation process. The excess noise factor is defined by

$$N_{XS} = \frac{\langle m^2 \rangle}{\langle m \rangle^2} = \frac{\langle m^2 \rangle}{M^2} \quad (2.30)$$

where  $m$  is the multiplication factor of a given electron-hole pair of a set of electron-hole pairs (Eq. 2.5) for a given photon absorption event, and  $M$  is the mean multiplication factor over all electron-hole pairs in the same circumstance. When no multiplication is experienced by the charge carriers (i.e.  $m = M = 1$ ), the excess noise factor is at its minimum,  $N_{XS} = 1$ .

The excess noise factor modifies Eq. 2.14 to make it

$$\Delta E = 2.35\omega_{EHP} \sqrt{\frac{(F+N_{XS}-1)E}{\omega_{EHP}} + R^2 + A^2} . \quad (2.31)$$

The excess noise factors for pure electron and pure hole initiated avalanche were thought until recently to be well described (McIntyre, 1966) as:

$$N_{XSe} = kM_e + \left(2 - \frac{1}{M_e}\right) (1 - k) \quad (2.32)$$

and

$$N_{XSh} = \frac{M_h}{k} + \left(2 - \frac{1}{M_h}\right) \left(1 - \frac{1}{k}\right) \quad (2.33)$$

where  $k = \beta/\alpha$ .

These relations suggest that to prevent broadening of the spectral resolution when the avalanche multiplication is appreciable, it is necessary to have electron and hole ionisation coefficients such that  $k$  is small. However, for most semiconductors  $k$  ranges from 0.3 to 1.0; consequently Eqs. 2.32 & 2.33 suggest large excess noise factors and therefore poor spectral resolution when the gain is appreciable. Another way to limit  $N_{XS}$  is to have a very thin ( $< 0.3 \mu\text{m}$ ) avalanche region; in this case dead space effects are exploited to restrict the range of probable multiplications achievable, thus limiting  $N_{XS}$  (Ng et al., 2002) (David & Tan, 2008).

However, recent theoretical work (Tan et al., 2011) has shown that for a photon of energy,  $E$ , where  $E/\omega_{EHP} \gg 1$ , the distribution of avalanche gains achieved by the charge carriers generated by the absorption of that photon is dependent on  $E/\omega_{EHP}$ , with larger values of  $E/\omega_{EHP}$  leading to lower (improved) values of  $N_{XS}$ . **Fig. 2.7** shows how as  $E/\omega_{EHP}$  increases, the distribution of gains tightens.

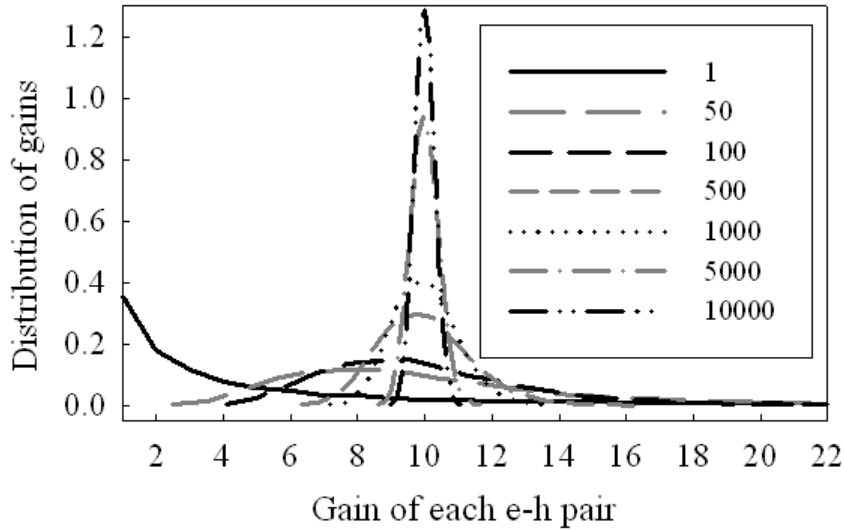


**Fig. 2.7.** Simulated gain distributions for numbers of electrons ( $E/\omega_{EHP}$ ) = 1 to 10000 (see figure key), injected at  $x = 0$  (the  $p^+$ -i boundary) when  $k = 1$  (the situation of greatest excess noise). Each distribution has a mean gain of 10. The distribution quickly tightens from exponential-like to narrow Gaussians as  $E/\omega_{EHP}$  increases (Tan et al., 2011).

## Chapter 3 Monte Carlo model

### 3.1 Introduction

This chapter describes a new Monte Carlo computer model that has been developed to simulate X-ray detection with three layer (e.g.  $p^+ - i - n^+$ ) non-avalanche and avalanche mesa photodiodes, the results of which are presented in later chapters. Monte Carlo modelling is a numerical simulation technique that can be used to model systems in which there are stochastic (probabilistic) processes that cannot be well modelled with deterministic methods. Many of the processes that occur in semiconductor X-ray detectors are probabilistic and the use of Monte Carlo techniques in the simulation of such devices is well established e.g. Lees (2010), Keister et al. (2010), Campbell et al. (2001), McCarthy et al. (1995) and Fraser et al. (1994). The aim of developing the model was to understand better the processes at work in X-ray semiconductor detectors, as well as predict detector behaviour and inform future detector development.

The model was developed in The Mathworks Inc. Matlab® 7.10.0 and run on a Microsoft® Windows® XP desktop PC with an Intel® Core 2 duo CPU. For a user defined three-dimensional, three layer compound semiconductor detector (e.g. an  $Al_{0.8}Ga_{0.2}As$   $p^+ - i - n^+$  diode) (§3.2) and X-ray source (§3.3), the relatively simple model simulates X-ray attenuation and photoelectric absorption (§3.4), electron-hole pair creation (§3.5), X-ray fluorescence (§3.6) and local model avalanche multiplication (§3.7), to produce a spectrum (§3.8). A flowchart giving an overview of the model is shown in **Fig. 3.1**. The processes shown in this overview are described in more detail in the sub-sections of this chapter.

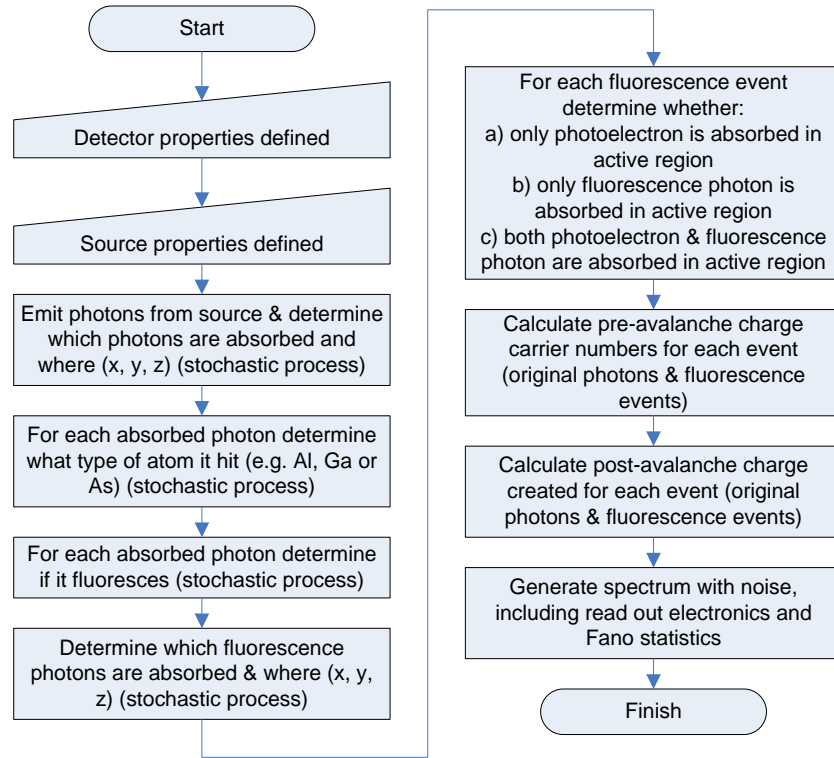


**Fig. 3.1.** Flow diagram of the Monte Carlo model.

### 3.2 Detector properties definition

A three-dimensional square single pixel mesa photodiode consisting of three layers is specified by the user. A schematic of the diode showing the definable dimensional parameters is given in **Fig. 3.2**. The detector sizes in the  $y$  and  $z$  dimensions ( $L_y$  and  $L_z$  respectively) are defined along with the  $x$ -dimension thickness of each layer ( $L_{x1}$ ,  $L_{x2}$  and  $L_{x3}$ ). The material from which each layer is made is input by the user in terms of its elemental composition and the X-ray fluorescence probabilities (yields) of each shell of those elements along with the elemental X-ray emission lines, fractional radiative rates and electron binding energies. The electron,  $\alpha$ , and hole,  $\beta$ , impact ionisation coefficients of the diode material as functions of electric field, along with the electric field strength to simulate, are also input by the user. The Fano factor, electron-hole pair creation energy for the material and the total noise in r.m.s.  $e^-$  to be simulated are specified. For layers 1 and 3 the electron,  $r_e$ , and hole,  $r_h$ , recombination lengths are also specified. The path to a pre-generated text file (using data from Cromer & Liberman (1970)) containing X-ray linear attenuation coefficients for the energy range of interest is provided by the user.

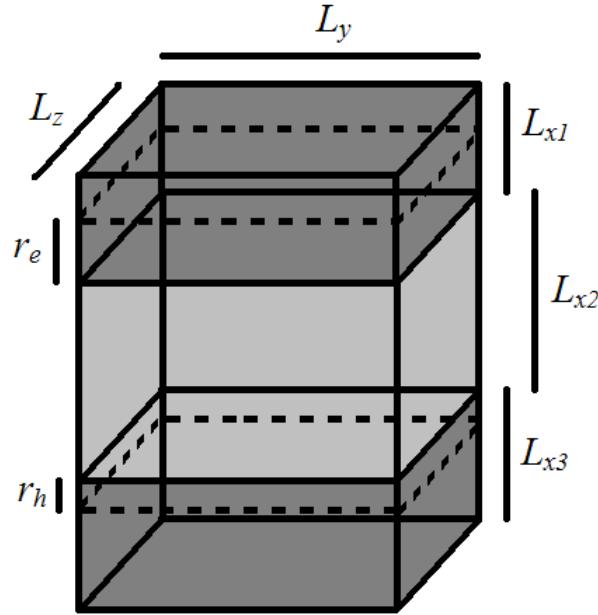


*Fig. 3.2. A schematic of the simulated diode with its dimensional definitions (see text).*

### 3.3 X-ray source properties definition

An X-ray source is specified by the user in terms of the number and energy of photons it will emit. The X-ray source can be configured to be monochromatic or polychromatic. In cases of polychromatic sources, the user can specify the number of photons the source emits at each energy. The user can choose for the X-rays to be emitted such that they are all incident in the middle of the  $y$ - $z$  diode face or, alternatively, so that the photons' positions of incidence are randomly distributed over the diode face. In either case, all emissions from the source are normal to the surface of the diode.

### 3.4 X-ray attenuation and photoelectric absorption

The probabilistic depth at which each photon would interact in a block of material of the same properties as the diode is calculated from Eq. 2.1 on a photon-by-photon basis by

$$d_i = \frac{1}{-\mu} \ln R_i \quad (3.1)$$

where  $d_i$  is the depth reached by the  $i^{\text{th}}$  photon,  $\mu$  is the linear attenuation coefficient at the energy of the  $i^{\text{th}}$  photon and  $R_i$  is a pseudorandom number drawn from a uniform distribution  $0 < R_i \leq 1$  for the  $i^{\text{th}}$  photon. If the depth at which the  $i^{\text{th}}$  photon is calculated to interact by Eq. 3.1 is less than the thickness of the diode, the position and the layer in which the photon interacts with the detector are recorded.

### 3.5 Electron-hole pair creation

For X-rays which do not fluoresce the atom with which they interact, each absorbed X-ray results in the generation of an average number of electron-hole pairs at the position of absorption in accordance with Eq. 2.5. The number of electron-hole pairs created is not single valued, but rather is the distribution which was described in §2.4.

Of the charge carriers generated by photons absorbed in layer 1, it is assumed that only electrons generated within one electron recombination length,  $r_e$ , of the layer 1-layer 2 boundary will reach and transit layer 2. Electrons generated in layer 1 more than one recombination length away from the layer 1-layer 2 boundary are assumed to recombine before they can be read out. The converse is true for layer 3: holes generated more than one hole recombination length,  $r_h$ , away from the layer 3-layer 2 boundary recombine before reaching layer 2. It is assumed that layer 1 is  $p^+$  doped and layer 3 is  $n^+$  doped so any minority charge carriers generated in these layers are reabsorbed before they can travel a significant distance and contribute their charge. In layer 2, the model assumes by default that both electron and hole recombination lengths are sufficiently long to allow complete collection of the charge carriers created in this layer.

Whether an atom fluoresces or not, when an atom photoelectrically absorbs an X-ray of energy  $E$ , the atom emits a photoelectron of energy,  $E_{pe} = E - E_b$ , where  $E_b$  is the electron binding energy of the shell of the atom with which the photon interacted (Eq. 2.2). Whilst in reality this photoelectron does have a non-zero, but short, range in the material over which it deposits its energy before being completely absorbed (0.12 and 0.42  $\mu\text{m}$  at 5 and 10 keV respectively in GaAs; 0.28 and 0.96  $\mu\text{m}$  at the same energies in silicon (Everhart & Hoff, 1971)), for simplicity the model assumes that the range is negligible and that all photoelectrons are reabsorbed at the point of creation, generating  $E_{pe}/\omega_{EHP}$  electron-hole pairs of the total number of electron-hole pairs generated ( $E/\omega_{EHP}$ ).

### 3.6 X-ray fluorescence

The probability,  $P$ , of an X-ray photon of energy,  $E$ , photoelectrically interacting with an atom of a particular element,  $i$ , in a compound made of a total number of elements,  $j$ , depends on the mass attenuation coefficient of each element at energy  $E$ ,  $\psi_i(E)$ ,  $\psi_{i+1}(E)$ , ...  $\psi_j(E)$ , and the weight fraction for each element in the compound,  $W_i$ ,  $W_{i+1}$ , ...  $W_j$ ,

(Eq. 2.15 & Eq. 2.16 of Jenkins et al. (1995)), such that the probability,  $P(i)$ , can be written as

$$P(i) = \frac{W_i \psi_i(E)}{\psi_c(E)} \quad (3.2)$$

where the weight fraction,  $W_i$ , is expressed as

$$W_i = \frac{n_i A_i}{\sum_{i=1}^j n_i A_i} \quad (3.3)$$

where  $n_i$  and  $A_i$  are the atomic fraction and atomic mass, respectively, of element  $n_i$  in the compound. The mass absorption coefficient for the compound,  $\psi_c$ , is expressed as

$$\psi_c(E) = \sum_{i=1}^j W_i \psi_i(E). \quad (3.4)$$

To model the stochastic process determining which type (element) of atom a photon initially interacts with, for each photon emitted a new pseudorandom number is drawn from a uniform distribution,  $0 < R_a \leq 1$ . For a compound consisting of three elements, A, B and C, given the probability of interacting with each (Eq. 3.2), if  $0 < R_a \leq P(A)$  then the photon is defined to have interacted with an element A atom, if  $P(A) < R_a \leq P(A) + P(B)$  the photon is defined to have interacted with an element B atom, and if  $P(A) + P(B) < R_a \leq 1$ , the photon interacted with an element C atom.

Once the element of initial interaction has been determined for each absorbed photon, the absorbing element's shells' electron binding energies are considered. Whilst the model takes into account the effects of K, L and M shell interactions for calculating the absorption (Cromer & Liberman, 1970), for simplicity the model currently only includes K shell fluorescence emission from the compound's elements; fluorescence from L and M shells will be included in future versions. Since K shell fluorescence can only occur when the interacting photon's energy,  $E$ , is greater than or equal to the K shell electron binding energy,  $E_k$ , for each interaction when  $E \geq E_k$ , the probability of fluorescence from that shell is considered for each photon-atom interaction.

The fluorescence yield,  $P(F)$ , for the K shell having already been specified by the user at the start of the simulation, a new pseudorandom number is drawn from a uniform distribution  $0 < R_f \leq 1$ . If  $R_f \leq P(F)$ , then the atom is considered to have fluoresced. For each atom that fluoresces, the fractional radiative rates of each emission line,  $P(K\alpha_1)$ ,  $P(K\alpha_2)$ ,  $P(K\beta_1)$ ,  $P(K\beta_2)$ ,  $P(K\beta_3)$ , are considered in order to determine the energy of the

fluorescence photon emitted in this instance. To do this, a new pseudorandom number is drawn from a uniform distribution  $0 < R_r \leq 1$  and, given the fractional radiative rates, **Table 3.1** lists the ranges of  $R_r$  that result in emission of each fluorescence photon.

Range of $R_r$	Fluorescence photon emitted
$0 < R_r \leq P(K\alpha_1)$	$K\alpha_1$
$P(K\alpha_1) < R_r \leq P(K\alpha_1) + P(K\alpha_2)$	$K\alpha_2$
$P(K\alpha_1) + P(K\alpha_2) < R_r \leq P(K\alpha_1) + P(K\alpha_2) + P(K\beta_1)$	$K\beta_1$
$P(K\alpha_1) + P(K\alpha_2) + P(K\beta_1) < R_r \leq P(K\alpha_1) + P(K\alpha_2) + P(K\beta_1) + P(K\beta_2)$	$K\beta_2$
$P(K\alpha_1) + P(K\alpha_2) + P(K\beta_1) + P(K\beta_2) < R_r \leq P(K\alpha_1) + P(K\alpha_2) + P(K\beta_1) + P(K\beta_2) + P(K\beta_3)$	$K\beta_3$

**Table 3.1.** Ranges of pseudorandom number,  $R_r$ , that result in the emission of each  $K$  shell fluorescence photon.

The fluorescence photon emitted from the absorbing atom is subject to attenuation and absorption in the same way as photons emitted from the X-ray source. The distance,  $d_{flu}$ , that the fluorescence photon travels from its point of creation is calculated by the same stochastic process as the original photons emitted from the source (§3.3). However, unlike the photons emitted from the source (which are all travelling perpendicular to the diode's  $y$ - $z$  plane), the direction in which each fluorescence photon travels is randomised. Two new pseudorandom angles,  $\theta$  and  $\varphi$ , drawn from a uniform distribution,  $0 < D \leq 2\pi$ , are generated for each fluorescence photon and these are used to randomise the vector describing the fluorescence photon's direction of travel (**Fig. 3.3**). The  $x$ ,  $y$ ,  $z$  components of distance that the fluorescence photon travels are thus calculated by:

$$d_{flux} = d_{flu} \sin \theta \quad (3.5a)$$

$$d_{flu y} = d_{flu} \cos \theta \cos \varphi \quad (3.5b)$$

$$d_{flu z} = d_{flu} \cos \theta \sin \varphi. \quad (3.5c)$$

These components are added to the coordinates of the absorption position of the initial photon to produce the coordinates of absorption of the fluorescence photon. This position is then recorded. Both the photoelectron and fluorescence X-ray generate electron-hole pairs in proportion to their respective energies when they are absorbed (§3.5). The charge carriers generated by both the photoelectron and the fluorescence photon are subject to avalanche multiplication (§3.7).

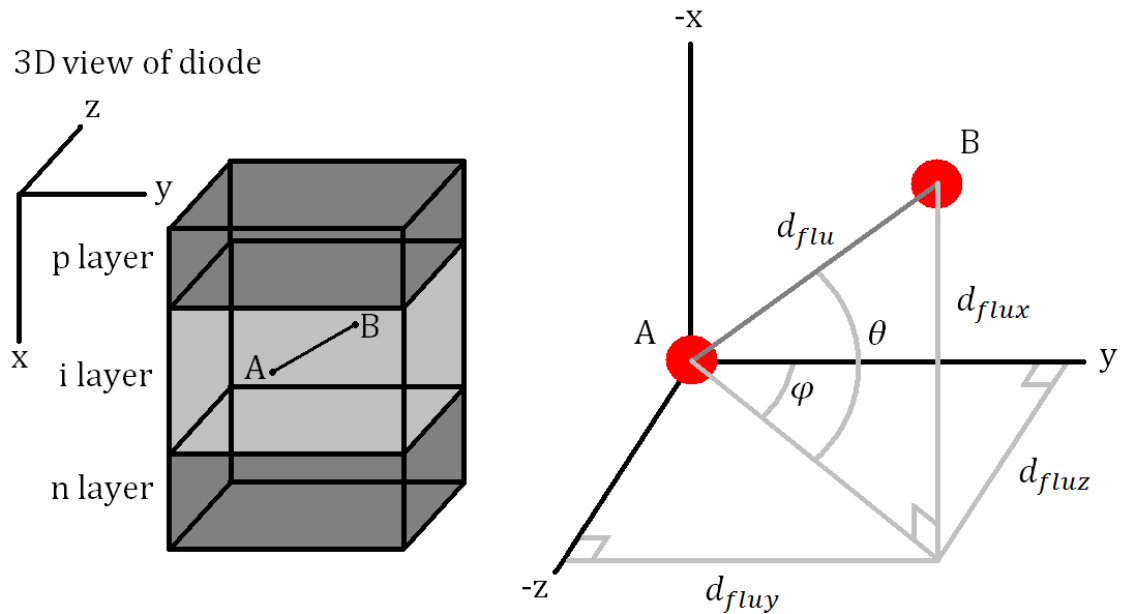


**Fig. 3.3.** Diagram showing the vector (and its components) that describes the path the fluorescence photon takes to its absorption position (B) from the initial photon's position of interaction (A). Variables previously defined in text.

The model uses the logic summarised by the truth table in **Fig. 3.4** to determine whether both the photoelectron and fluorescence photon contribute charge to the spectrum or only one of them (and if only one of them, which one). When both the photoelectron and the fluorescence photon are absorbed in the active region (i layer + layer 1  $r_e$  + layer 3  $r_h$ ) the sum of their charge (post-avalanche) is contributed to the spectrum in one event. When there is no avalanche multiplication, this event is of the same charge (within the variance of Eq. 2.10) as if the original photon had not fluoresced and instead just contributed its charge directly. When just the fluorescence photon is absorbed in the active region, only its charge contributes to the spectrum – events from this process contribute to the fluorescence peak. When just the photoelectron from the source photon is absorbed in the active region, only its charge contributes to the spectrum – events of this nature contribute to the escape peak. When there is avalanche

multiplication, the charge carriers generated by both the photoelectron and fluorescence photon are subject to avalanche multiplication before the charge is contributed to the spectrum. When neither the photoelectron or fluorescence photon is absorbed in the active region, no charge is contributed to the spectrum.

	<b>Fluorescence photon absorbed in active region of detector</b>	<b>Fluorescence photon not absorbed in active region of detector</b>
<b>Photoelectron from source photon absorbed in active region of detector</b>	Charge from photoelectron and fluorescence photon collected	Only charge from photoelectron collected (escape peak)
<b>Photoelectron from source photon not absorbed in active region of detector</b>	Only charge from fluorescence photon collected (fluorescence peak)	No charge from photoelectron or fluorescence photon collected

*Fig. 3.4. Truth table summarising the outcomes of photoelectron and fluorescence photon absorption in the model.*

### 3.7 Avalanche multiplication

In the simulation, a local model as per §2.7 and McIntyre (1966) is assumed. The avalanche multiplication factor  $M$  (the avalanche gain experienced), Eq. 2.24, is thus dependent on the position at which the electron-hole pair is created and the electron and hole ionisation coefficients,  $\alpha$  and  $\beta$  respectively. Dead space effects are neglected for simplicity (Ng et al., 2001).

The electric field strength used in the avalanche multiplication calculations is specified by the user, and restricted to layer 2 in a uniform field profile. Since the high field region is restricted to layer 2, when a photon is absorbed in layer 1 within one electron recombination length of layer 2, the electron's starting position for multiplication purposes is the layer 1-layer 2 boundary (i.e. at  $x = 0$  in Eq. 2.24). When a photon is absorbed in layer 2, the starting location for multiplication purposes is the position of photon absorption. The same is assumed to be true for photoelectrons.

The electron,  $\alpha$ , and hole,  $\beta$ , ionisation coefficients are calculated by the model from the electric field parameterised versions input by the user. For  $\text{Al}_{0.8}\text{Ga}_{0.2}\text{As}$  the parameterised forms of the ionisation coefficients have been reported by Ng et al. (2001) as:

$$\alpha = 3.18 \times 10^5 \exp \left[ - \left( \frac{1.04 \times 10^6}{E} \right)^{1.67} \right] \text{cm}^{-1} \quad (3.6a)$$

$$\beta = 3.55 \times 10^5 \exp \left[ - \left( \frac{1.12 \times 10^6}{E} \right)^{1.85} \right] \text{cm}^{-1} \quad (3.6b)$$

where  $E$  is the electric field in V/cm. The position dependent multiplication factor is then used on a photon-by-photon basis to calculate the total charge contribution to the spectrum from each photon absorption event.

The noise contribution to the final spectrum from the variation in the multiplication factor between sibling electron-hole pairs created from the same photon absorption event, i.e. the excess noise (§2.7.4), is assumed to be negligible because  $E/\omega_{EHP} \gg 1$  for X-ray energies (Tan et al., 2011).

### 3.8 Spectrum generation

The charge generated in the detector for each photon emitted from the source (taking account of fluorescence, avalanche multiplication and all other processes) is subjected to random Gaussian noise (using pseudorandom numbers drawn from a Gaussian distribution in Matlab) to simulate the noise (see §2.6) specified by the user. Finally, the charge is calibrated into its energy equivalent and binned into energy bins of width specified by the user.

# Chapter 4    The temperature dependence of Al<sub>0.8</sub>Ga<sub>0.2</sub>As non-avalanche photodiodes

## 4.1    Introduction

This chapter describes work characterising the temperature dependence of the X-ray spectroscopic performance of Al<sub>0.8</sub>Ga<sub>0.2</sub>As non-avalanche photodiodes with a view to establishing their performance at high temperatures. The experimental methods and techniques used to characterise the devices are presented, along with the findings of the experimental work performed.

## 4.2    Background

Previous investigation of Al<sub>0.8</sub>Ga<sub>0.2</sub>As photodiodes for soft X-ray photon counting spectroscopy has shown that they can operate with promising spectral resolution (~1.5 keV FWHM at 5.9 keV) at room temperature (Lees et al., 2008). However, there has been no report of their operation at any other temperature and no report of the temperature dependence of their spectral performance. The reports in the literature regarding Al<sub>x</sub>Ga<sub>1-x</sub>As photon counting X-ray detectors are very few. Ripamoni et al. (1990) and Lauter et al. (1995, 1996) reported graded  $x$  Al<sub>x</sub>Ga<sub>1-x</sub>As/GaAs separate absorption and multiplication (SAM) staircase photodiodes, and Silenas (2004), Silenas et al. (2002, 2003, 2005, 2006, 2011) and Dapkus et al. (2007) have reported non-photon counting Al<sub>x</sub>Ga<sub>1-x</sub>As/GaAs X-ray detectors. Lees et al. (2008) was the only report of Al<sub>x</sub>Ga<sub>1-x</sub>As p<sup>+</sup>-p<sup>-</sup>-n<sup>+</sup> (or p<sup>+</sup>-i-n<sup>+</sup>) spectroscopic X-ray photon counting photodiodes in the literature at the start of the research reported in this thesis. However, work on Al<sub>0.8</sub>Ga<sub>0.2</sub>As p<sup>+</sup>-i-n<sup>+</sup> photodiodes for telecommunications had been reported, concentrating on the characterisation of avalanche multiplication in the material at room temperature (Ng et al., 2000, 2001, 2002) (Saleh et al., 2000), as had similar work for Al<sub>x</sub>Ga<sub>1-x</sub>As  $x < 0.8$ , e.g. Plimmer et al. (2000) and Tan et al. (2001).

If detectors made from  $\text{Al}_{0.8}\text{Ga}_{0.2}\text{As}$  can operate at temperatures  $> 20\text{ }^\circ\text{C}$ , as the wide band gap of  $\text{Al}_{0.8}\text{Ga}_{0.2}\text{As}$  (2.09 eV) suggests may be possible (by reducing parallel white noise from the thermally dependent leakage current (§2.6.3)), depending on the spectral resolution required, it may remove or reduce the need for the cooling normally needed by conventional semiconductor detectors in these regimes. This would reduce the volume and mass of the instruments into which the detectors are integrated and potentially lead to cost savings and greater instrument robustness because the detectors would not be dependent on cooling systems.

### 4.3 Diode fabrication and design

Circular mesa  $\text{Al}_{0.8}\text{Ga}_{0.2}\text{As}$  diodes of 25, 50, 100 and 200  $\mu\text{m}$  radii were fabricated by photolithography from wafers grown on GaAs  $n^+$  substrates by molecular beam epitaxy at the National Centre for III-V Technologies, University of Sheffield, UK and mounted in TO-5 packages (gold plated, 9 mm diameter, 12 pins, see **Fig. 4.1**). Diode layer thicknesses and dopings as estimated at University of Sheffield from capacitance-voltage ( $C$ - $V$ ) measurements (**Fig. 4.4**) which show how the capacitance of the device changes as the reverse bias is increased and the  $i$  layer is swept out, are given for the  $\text{Al}_{0.8}\text{Ga}_{0.2}\text{As}$  diodes in **Table 4.1**.

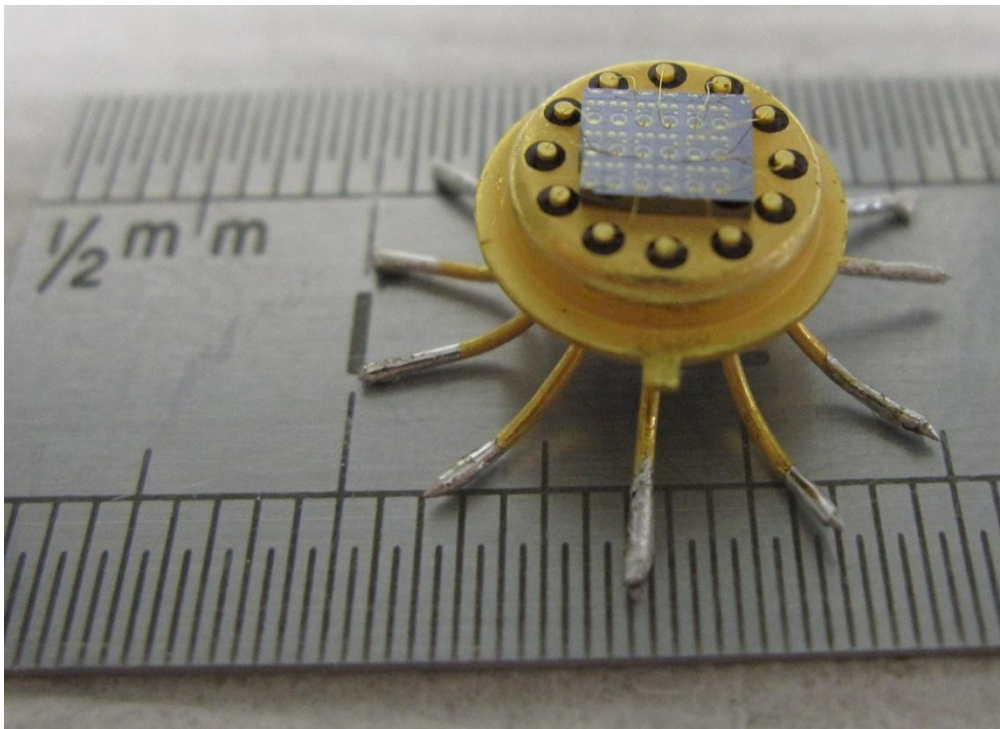


**Fig. 4.1.** Photograph of a TO-5 package with attached wafer chip. The smallest divisions on the scale are 0.5 mm.

The calculated (Eq. 2.1) quantum efficiency of the  $\text{Al}_{0.8}\text{Ga}_{0.2}\text{As}$  devices implied by the layer thicknesses in **Table 4.1** (assuming only charge generated in the i layer (layer 3) is collected) is shown in **Fig. 4.2**, along with a plot of the quantum efficiency if the same device were made of silicon. The greater density of  $\text{Al}_{0.8}\text{Ga}_{0.2}\text{As}$  can be seen contributing to the greater efficiency of the device, albeit at the expense of additional absorption edges. If the detector was being used to examine elements which have X-ray emission or escape lines in the regions of these edges (see **Fig. 4.2**), the absorption edges and detector internal fluorescence and escape lines (see Chapter 5) of the  $\text{Al}_{0.8}\text{Ga}_{0.2}\text{As}$  device would complicate analysis of the spectrum because the effects of these lines and edges would have to be subtracted from the spectrum in order to quantify the abundance of these and other nearby elements (in energy terms) in the sample. For planetary X-ray fluorescence spectroscopy (XRF), many common interesting X-ray lines are below the Ga and As K edges (10.367 and 11.867 keV, respectively) (see Chapter 1), so these particular edges may encroach less on the spectrum than the Ga and As L and Al K edges (which are in the region 1.1 – 1.6 keV). It should be noted that silicon has its K edge at 1.839 keV which is also in the region of interest for planetary XRF, so even with a Si detector it can be necessary to process spectra to subtract effects of detector fluorescence in this region.

An optical microscope photograph showing the diode layout of an  $\text{Al}_{0.8}\text{Ga}_{0.2}\text{As}$  chip ready for packaging is shown in **Fig. 4.3**. For the 100 and 200  $\mu\text{m}$  radii diodes, quasi-annular contacts (Au/Zn/Au) which provide electric field uniformity across the face of the diode are used, along with enlarged area bond pads to facilitate easier wire bonding (**Fig. 4.3**).

Layer	Material	Thickness ( $\mu\text{m}$ )	Dopant	Type	Doping Density ( $\times 10^{18} \text{ cm}^{-3}$ )
1	GaAs	0.01	Be	$\text{p}^+$	2.5
2	$\text{Al}_{0.8}\text{Ga}_{0.2}\text{As}$	1	Be	$\text{p}^+$	2.0
3	$\text{Al}_{0.8}\text{Ga}_{0.2}\text{As}$	1	Undoped		
4	$\text{Al}_{0.8}\text{Ga}_{0.2}\text{As}$	1	Si	$\text{n}^+$	2.5
5	GaAs	0.25	Si	$\text{n}^+$	2.5
Substrate	$\text{n}^+$ GaAs				

**Table 4.1.** Layer details of the  $\text{Al}_{0.8}\text{Ga}_{0.2}\text{As}$  wafer.

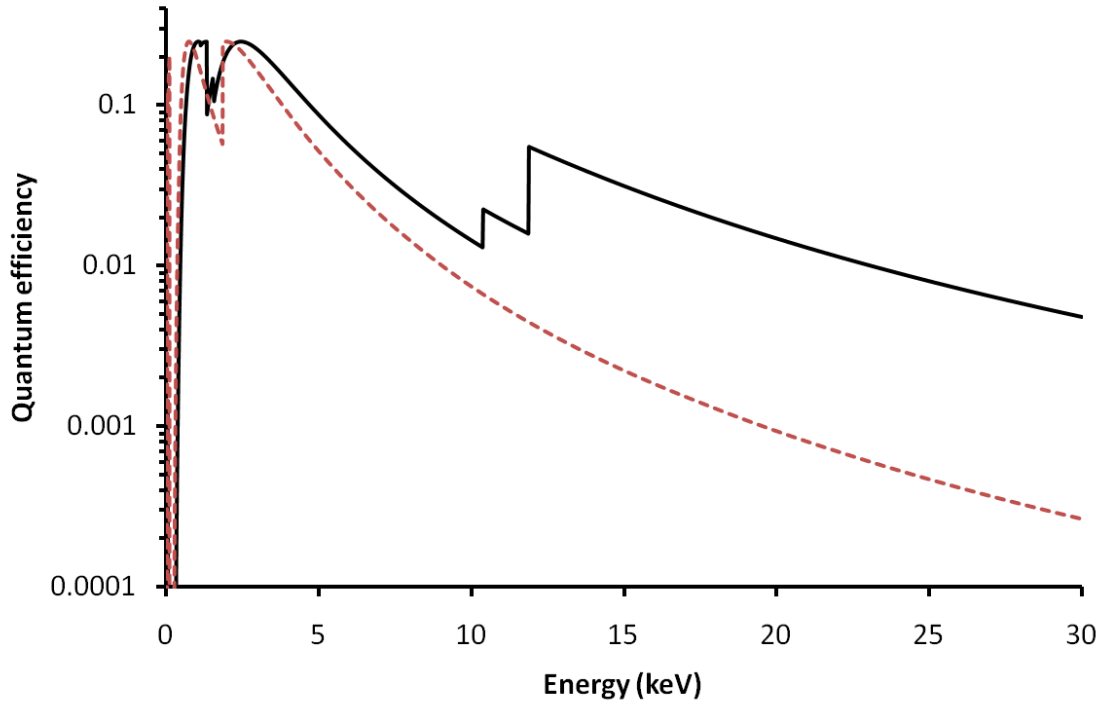


**Fig. 4.2.** The quantum efficiency of the  $Al_{0.8}Ga_{0.2}As$   $p^+i-n^+$  diodes (solid black line) with varying X-ray energy (assuming only charge generated in the  $i$  layer (layer 3) is collected). For comparison, the quantum efficiency of the same structure of diode made from silicon is also shown (dashed red line). The discontinuities are the absorption edges of As (K edge = 11.867 keV, L edges = 1.527, 1.359 and 1.324 keV), Ga (K edge = 10.367 keV, L edges = 1.299, 1.143 and 1.116 keV) and Al (K edge = 1.560 keV) and Si (K edge = 1.839 keV)

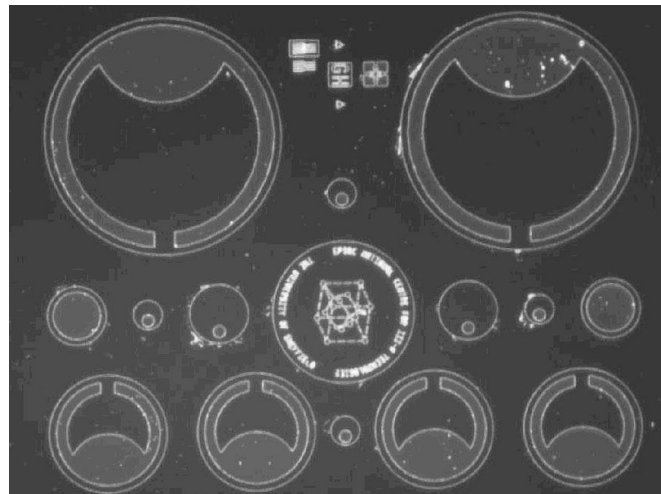


**Fig. 4.3.** An optical microscope photograph showing the diode layout of an  $Al_{0.8}Ga_{0.2}As$  chip ready for packaging (Lees et al., 2008).

The active layer of the devices is considered to be limited to the i layer (layer 3); the large doping concentrations in the  $p^+$  and  $n^+$  layers limit extension of the depletion region into the  $p^+$  and  $n^+$  layers at normal operating reverse bias (10 V) to a total of  $6.5 \times 10^{-3} \mu\text{m}$  (Eq. 2.3 using **Table 4.1**) which is small compared with the thickness of the i layer (1  $\mu\text{m}$ ).  $C$ - $V$  testing at the University of Sheffield showed that the i layer is swept out and the capacitance of the 100  $\mu\text{m}$  radius diode = 3.1 pF at reverse biases  $\geq 10$  V (**Fig. 4.4**).

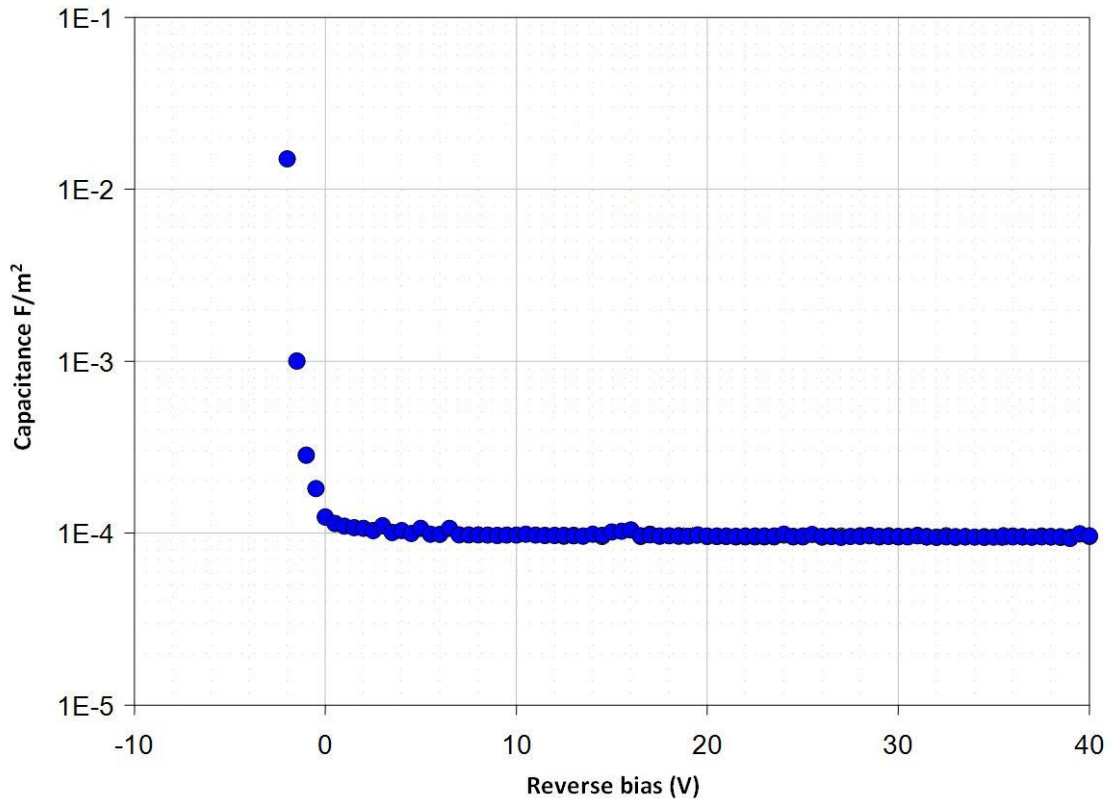


**Fig. 4.4.** Measurements of the area normalised capacitance of a 100  $\mu\text{m}$  radius diode with varied reverse bias, courtesy of Dr. J. S. Ng, Department of Electronic and Electrical Engineering, University of Sheffield, UK.

#### 4.4 Leakage current measurements

The three functional 100  $\mu\text{m}$  radius diodes on the diode chip supplied by University of Sheffield were installed in a mechanical mounting (MM) and placed inside a Design Environmental FS55-65 Temperature Test Chamber (TTC) (Design Environmental, N.D.). Each diode was individually reverse biased in turn by an externally located Thurlby Thandar Instruments PL330QMD stabilised power supply kept at room temperature (Thurlby Thandar Instruments Ltd, N.D.). The leakage current of each

diode was amplified by a Keithley Instruments 427 current amplifier (Keithley Instruments Inc., 1975) and measured by an Iso-Tech IDM 105 digital multimeter, both located outside the TTC. Room temperature (20 °C) current-voltage measurements (up to 28 V reverse bias) were taken for each diode and are plotted in **Fig. 4.5**. At 10 V (the operating reverse bias of these diodes used for the spectroscopic X-ray measurements, see §4.5), diodes 1, 2 and 3 were found to have leakage currents of 4.3, 5.6 and 11.9 pA, respectively. The variation in the leakage currents between diodes may be attributable to variations in wafer quality and/or diode fabrication.

The two diodes with the lowest leakage current at 10 V, D1 and D2, (4.3 and 5.6 pA, respectively) were selected on this basis for temperature dependence testing of their leakage current and X-ray spectroscopic performance. The measurements were taken at temperatures between +90 °C and -30 °C, in 10 °C steps. The temperature inside the MM was monitored by thermocouple and Fluke 50D digital thermometer to ensure that the temperature had equalised between the MM and chamber after each temperature change. The diode and the MM were assumed to be in thermal equilibrium. **Fig. 4.6** shows how the leakage currents of the diodes vary as a function of temperature. At temperatures > 60 °C, the leakage currents of the devices diverge from each other. The exact cause of the difference between the leakage currents is currently unknown but is attributed to small variations in wafer quality and diode fabrication, as for the room temperature *I-V* testing leakage current variations (**Fig. 4.5**). Even at the highest measured temperature (90 °C), the difference is less than a factor of two and the leakage current is still < 200 pA in each case.

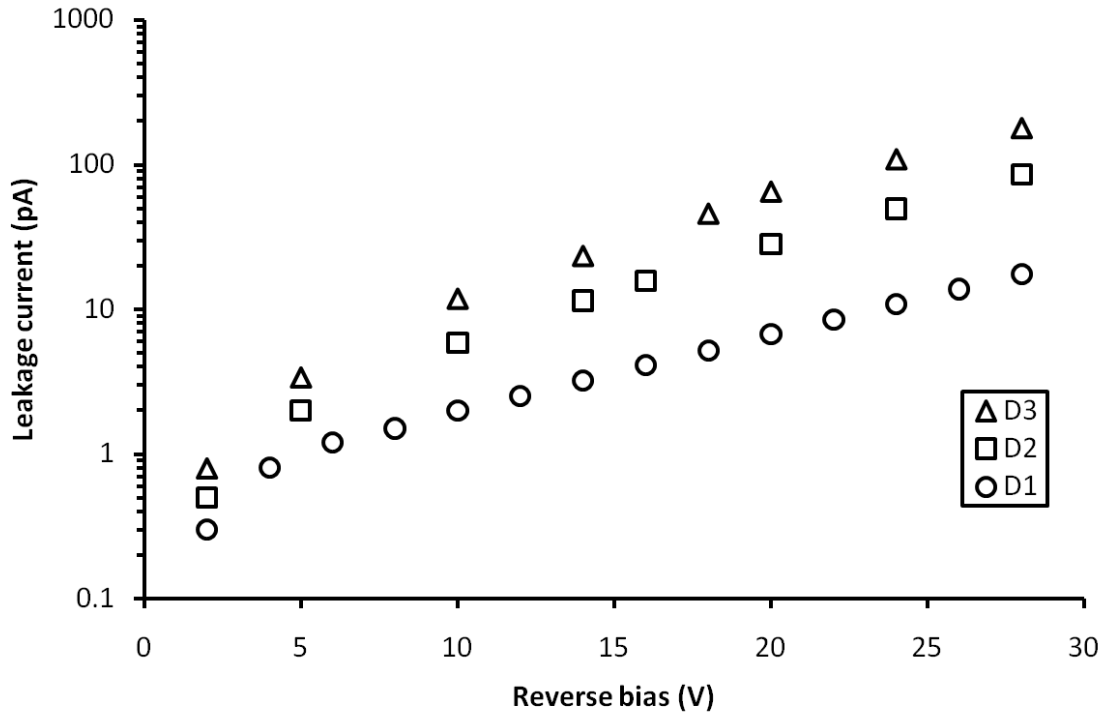


**Fig. 4.5.** Room temperature (20 °C) leakage current dependence on reverse bias of  $Al_{0.8}Ga_{0.2}As$  100  $\mu m$  radius diodes, D1 (open circles), D2 (open squares), D3 (open triangles).

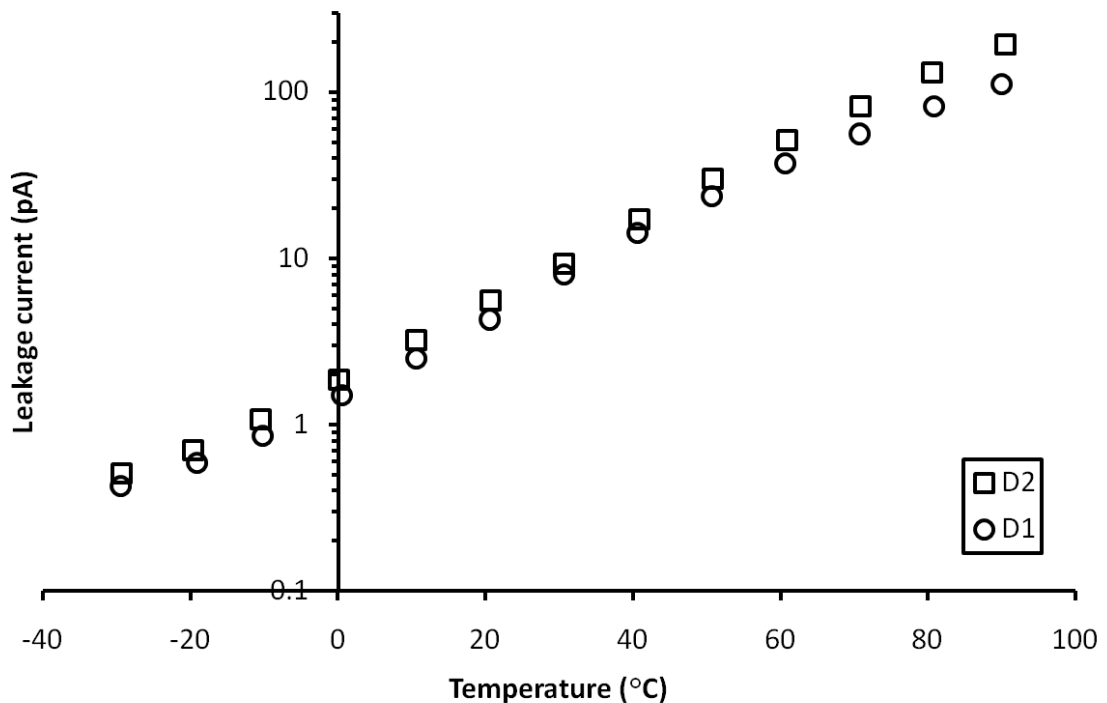


**Fig. 4.6.** The measured temperature dependence of the leakage current of  $Al_{0.8}Ga_{0.2}As$  diodes D1 (open circles) and D2 (open squares) at 10 V.

## 4.5 $^{55}\text{Fe}$ X-ray spectral measurements

To obtain the X-ray measurements, each diode was individually reverse biased at 10 V and connected to a charge-sensitive preamplifier with a Si JFET (Vishay Siliconix 2N4416, capacitance = 2 pF) input transistor (Siliconix, 1997). The preamplifier was connected to an EG&G Ortec® 571 shaping amplifier (EG&G Ortec, N.D.) (shaping time constant = 3  $\mu\text{s}$ ) whose output signal was connected to an Ortec multi-channel analyser (MCA) (Advanced Measurement Technology Inc., 2008) (**Fig. 4.7**). The input discriminator level of the MCA was adjusted to minimise the number of noise counts from the zero energy noise peak. An  $^{55}\text{Fe}$  radioisotope source ( $\sim 10$  MBq) giving characteristic Mn  $K\alpha$  and  $K\beta$  peaks (5.9 keV and 6.5 keV) was used as the X-ray source and positioned 3 mm above the diode (detected count rate = 28  $\text{s}^{-1}$ ). The X-ray source, diode and preamplifier were installed in the TTC and subject to temperature control. The shaping amplifier and MCA were located outside the TTC, at room temperature. During the measurement period, the bias voltage was continuously applied to the diode and the preamplifier constantly powered. For all temperature measurements, to ensure thermal equilibrium, the system was allowed to stabilise for  $\geq 1$  h after the diode and preamplifier had reached the target temperature before the X-ray spectra were accumulated.

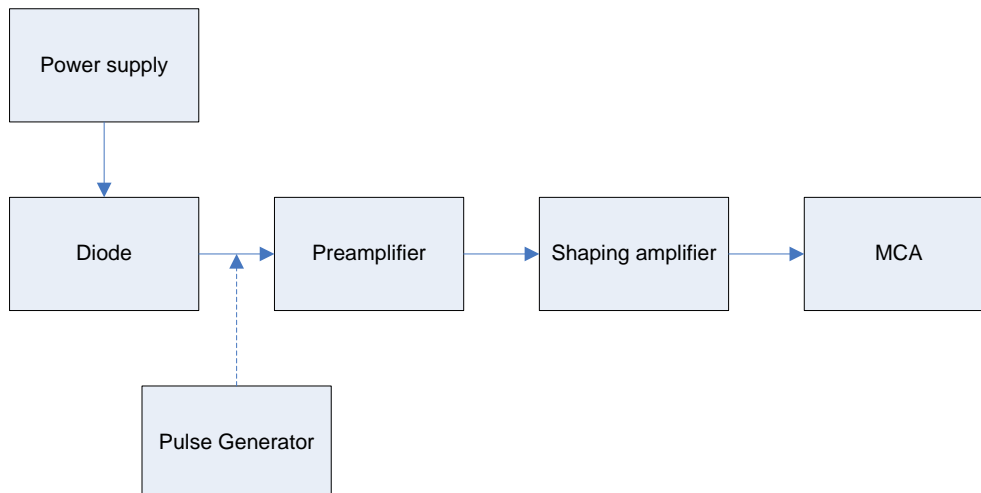


**Fig. 4.7.** Block diagram showing the electronics chain for spectral measurements (see text) (see §4.6.2 for pulse generator).

A typical  $^{55}\text{Fe}$  spectrum obtained at 20 °C with D1 at 10 V is shown in **Fig. 4.8**. Double Gaussians (dashed lines in **Fig. 4.8**) were fitted to the observed peak representing the

Mn  $K\alpha$  (5.9 keV) and  $K\beta$  (6.5 keV) peaks from the radioisotope source, which are too close together to be resolved with the present energy resolution of the detector. A low energy cut off of 2 keV was set as a compromise between minimising the number of noise counts from the tail of zero energy noise and maintaining the low energy response of the detector. Also seen in **Fig. 4.8**, is low energy tailing on the combined Mn  $K\alpha$ , Mn  $K\beta$  peak due to partial charge collection, possibly from photon interactions in the non-active layers and substrate. The upwards curve on the low energy tail at low energies is from the right hand side of the zero energy noise peak, which has not been entirely eliminated by the 2 keV low energy cut off, extending under the low energy tail of the combined Mn  $K\alpha$  Mn  $K\beta$  peak. The spectra were calibrated in energy terms by using the zero energy noise peak and the observed peak from the radioisotope source as points of known energy on the MCA's charge scale and assuming a linear variation of detected charge with energy (Eq. 2.5). The spectral resolution (as measured by the FWHM) at 5.9 keV of the complete system for D1 and D2 as a function of temperature is shown in **Fig. 4.9**. At room temperature, the diodes have energy resolutions (FWHMs) at 5.9 keV of 1.07 keV (D1) and 1.12 keV (D2). At 90 °C, the FWHMs at 5.9 keV of D1 and D2 are 2.2 keV and 2.5 keV, respectively. The difference in spectral resolution between D1 and D2 is small ( $\leq 50$  eV) at low temperatures ( $\leq 30$  °C), but larger than can be entirely attributed to the differences in leakage current of the diodes (**Fig. 4.6**): plots of the temperature dependence of FWHM of each diode with the effect of the leakage current removed (i.e. with parallel white noise subtracted) still diverge with increasing temperature (**Fig. 4.10**). The remaining difference in spectral resolution between the two diodes may be attributable to small variations in diode fabrication or wafer quality.

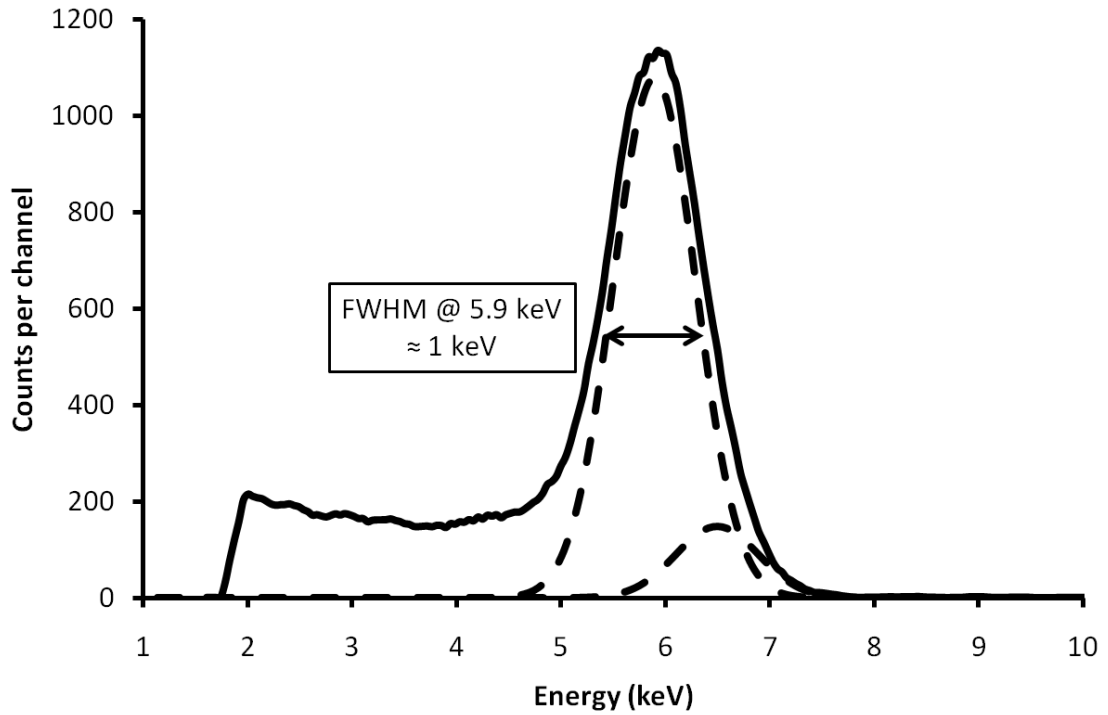


**Fig. 4.8.** A typical  $^{55}\text{Fe}$  spectrum (solid line) obtained at 20 °C and 10 V with diode D1. The Mn K $\alpha$  (5.9 keV) and K $\beta$  (6.5 keV) X-ray lines (dashed lines) are not resolved and contribute to a single peak.

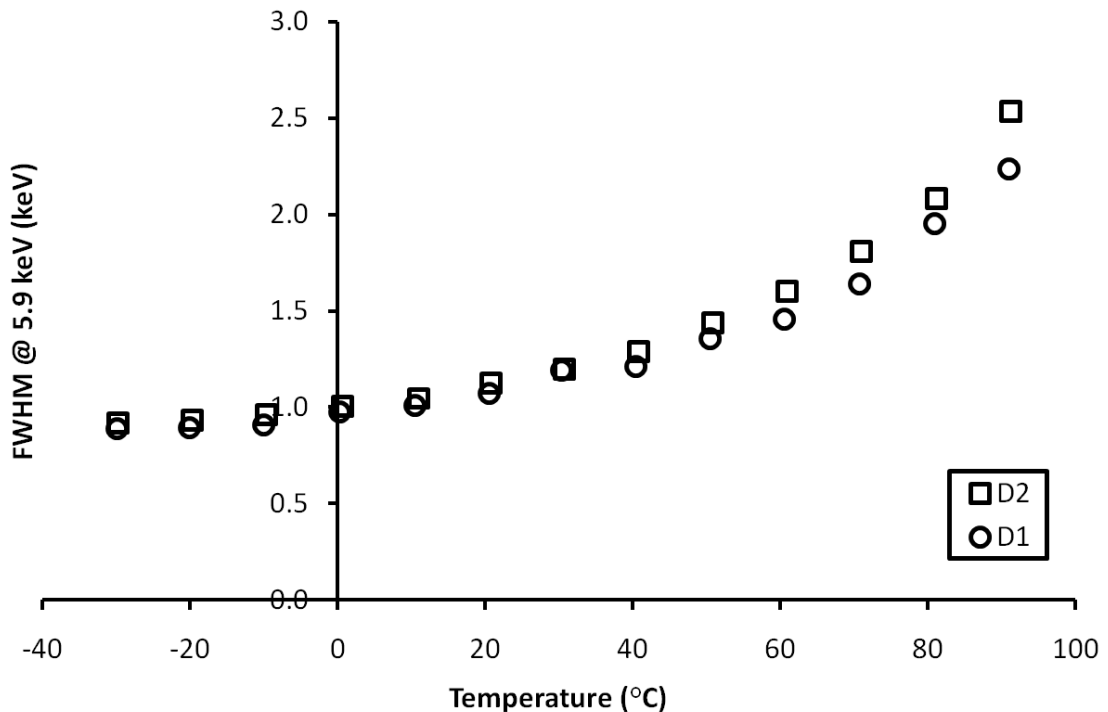


**Fig. 4.9.** The temperature dependence of the spectral resolution (FWHM at 5.9 keV) of diodes D1 (open circles) and D2 (open squares).

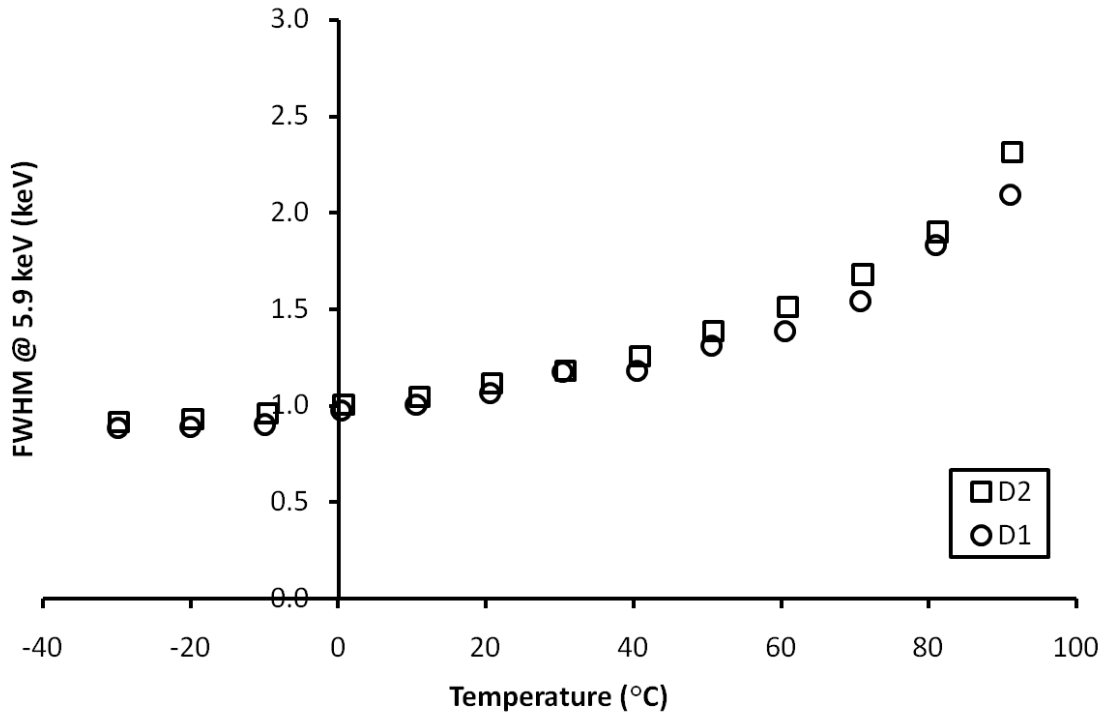


**Fig. 4.10.** The temperature dependence of the spectral resolutions (FWHM at 5.9 keV) of diodes D1 (open circles) and D2 (open squares) with the effects of the leakage current subtracted.

## 4.6 Noise analysis

### 4.6.1 Initial measurements

The spectral resolutions reported in §4.5 for the  $\text{Al}_{0.8}\text{Ga}_{0.2}\text{As}$  diodes are much poorer than would be expected if the system were Fano limited. The expected Fano limited resolution is 155 eV FWHM at 5.9 keV (assuming a Fano factor = 0.14 throughout the measured temperature range and an electron-hole pair creation energy = 5.25 eV (NSM Archive, 2004)). In Chapter 2, the noise components which limit the energy resolution of soft X-ray detectors were reviewed. To assess the composition of the noise that is causing the resolutions achieved with the diodes to be poorer than the expected Fano limit, the detector's parallel white noise,  $N_{PW}$ , contributions were calculated for each temperature (Eqs. 2.16 and 2.17, with  $A_3 = 2$ ) and subtracted, along with the calculated Fano noise contribution,  $N_F$ , in quadrature from the total system noise observed. Assuming broadening of the 5.9 keV FWHM by charge trapping noise is insignificant compared with the other noise sources (**Fig. 4.8**), the remaining noise is the contribution from the rest of the electronics,  $N_E$ , (i.e. series white noise, induced gate current noise,

$1/f$  noise, dielectric noise and parallel white noise of the JFET). The noise contributions from  $N_F$ ,  $N_{PW}$  and  $N_E$ , and their temperature dependences can be seen in **Fig. 4.11**.

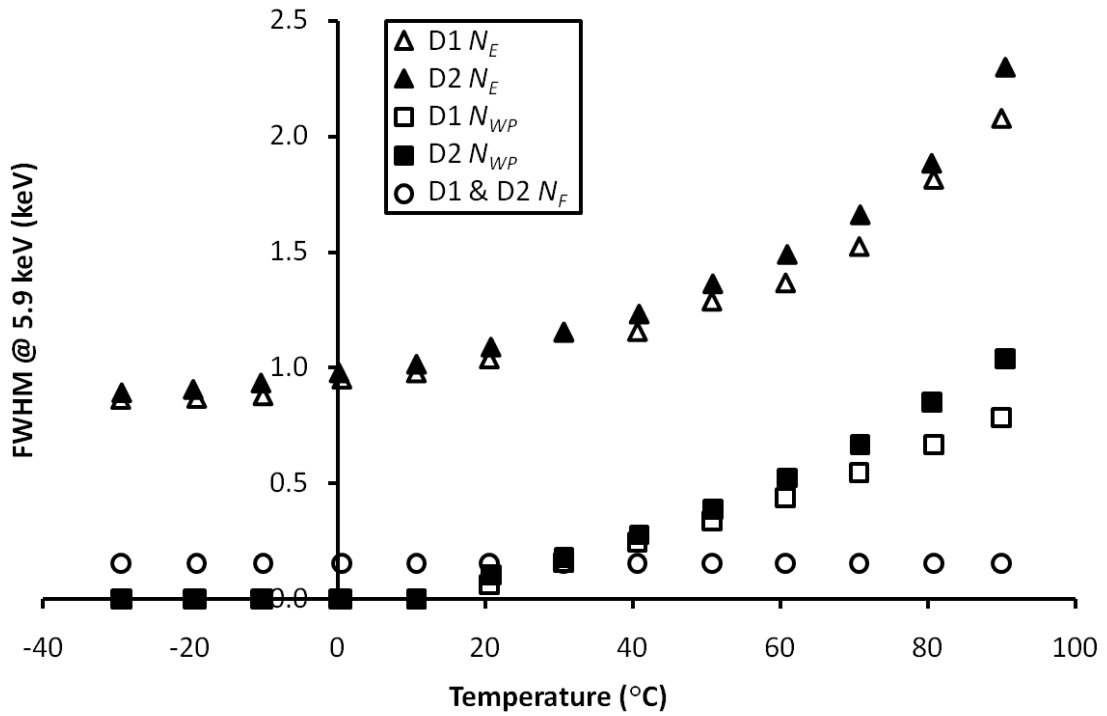


**Fig. 4.11.** The calculated noise contributions for the system as a function of operating temperature. D1: remaining electronics noise (open triangles), D2: remaining electronics noise (filled triangles); D1: detector parallel white noise (open squares), D2: detector parallel white noise (filled squares) and D1 and D2 Fano noise (open circles) (assuming  $F = 0.14$  and  $\omega_{EHP} = 5.25$  eV throughout the measured temperature range).

#### 4.6.2 Shaping time measurements

To further analyse the contribution of the noise components, a pulse generator was connected to the system (**Fig. 4.7**). By measuring the FWHM of the peak produced by the pulse generator, the performance of the electronics can be characterised without having to disentangle detector effects such as Fano noise, charge trapping and partial charge collection. Since the electronics' performance depends on the capacitance of the detector and the detector's leakage current (Chapter 2), the detector remained connected to the system and reverse biased (10 V) during these measurements. It was also necessary to keep the detector connected and powered in order to energy calibrate the spectra produced by using the zero energy noise peak and combined Mn  $K\alpha$  Mn  $K\beta$  peak from the  $^{55}\text{Fe}$  source (as per §4.5). To assess the shaping time and temperature

dependence of the electronics noise, spectra were accumulated with shaping times of 0.5, 1, 2, 3, 6 and 10  $\mu\text{s}$  at temperatures of +50, +20 and -10  $^{\circ}\text{C}$ .

Unlike the parallel white noise ( $N_{PW}$ ), the series white noise including induced gate current noise ( $N_{SWC}$ ) and  $1/f$  noise ( $N_{1/f}$ ) contributions (see §2.6), the dielectric noise ( $N_D$ ) is not readily calculable because the stray capacitances are not easily measured. However, by calculating the noise contributions from detector and JFET parallel white noise (§2.6.3), series white noise including induced gate current noise (§2.6.4 and §2.6.7), and  $1/f$  noise (§2.6.5), and subtracting these in quadrature from the total noise,  $N_T$ , shown by the FWHM of the pulser peak, it is possible to obtain an estimate for the dielectric noise,  $N_D$ , assuming any noise sources other than those mentioned are insignificant.

The total (detector and JFET) parallel white noise contribution for each shaping time and temperature was calculated from Eqs. 2.16 and 2.17 with signal shaping function constant  $A_3 = 2$  (Gatti et al., 1990) (EG&G Ortec, N.D.). The JFET's parallel white noise contribution was estimated to be 0.10, 0.11 and 0.50 keV at -10, 20 and 50  $^{\circ}\text{C}$ , respectively (Siliconix, 1997). The series white noise contribution was calculated from Eqs. 2.18 and 2.19 assuming  $\gamma = 0.85$  (Bertuccio, Pullia & DeGeronimo, 1996), transconductance of the JFET  $g_m = 5 \text{ mS}$  (Siliconix, 1997), and that the total capacitance at the preamplifier input,  $C_T$ , is dominated by the capacitances of the detector (3.1 pF) and JFET (2 pF). The series white noise contribution was adjusted for induced gate current noise (§2.6.7) by assuming  $\sqrt{G_c} \approx 0.8$  (Bertuccio, Pullia & DeGeronimo, 1996). The  $1/f$  noise contribution was calculated from Eq. 2.20 with the above assumptions and also that  $A_2 = 1.2$  and  $A_f = 3 \times 10^{-15} \text{ V}^2$  (Gatti et al., 1990).

The calculated total (detector and JFET) parallel white, series white (including induced gate current noise) and  $1/f$  noise components together with the measured pulser peak FWHM and estimated dielectric noise contribution ( $N_D^2 = N_T^2 - N_{PW}^2 - N_{SWC}^2 - N_{1/f}^2$ ) at each shaping time for temperatures of +50, +20 and -10  $^{\circ}\text{C}$  are shown in **Fig. 4.12**. The contribution from the parallel white noise decreases and the series white contribution increases as the shaping time is increased at all three temperatures. The increase in parallel white noise with increased shaping time is more significant at higher temperature because of the positive temperature dependence of the leakage current of the detector (**Fig. 4.5**) and JFET. The series white noise contribution can be seen

decreasing with increasing shaping time, as expected from its  $1/\tau$  dependence (Eq. 2.19). The  $1/f$  noise contribution is not shaping time dependent and is, therefore, constant (Eq. 2.20). The shaping time at which the functions representing the parallel white and series white contributions intersect lengthens with decreasing temperature ( $\tau = 2 \mu\text{s}$  at  $50 \text{ }^\circ\text{C}$ ,  $\tau = 5.25 \mu\text{s}$  at  $20 \text{ }^\circ\text{C}$ ,  $\tau = 8.45 \mu\text{s}$  at  $-10 \text{ }^\circ\text{C}$ ). The optimum shaping time lengthens with decreasing temperature ( $\tau = 2, 3$  and  $6 \mu\text{s}$  at  $50, 20$  and  $-10 \text{ }^\circ\text{C}$ , respectively). The data shown in **Fig. 4.12** suggest that dielectric noise is a significant noise source; indeed for the temperature range shown, the analysis suggests that the dielectric noise is the most significant noise source.

The estimated dielectric noise is broadly similar across the measured shaping times as would be expected from a shaping time independent contribution (Eq. 2.21). However, slight increases in the calculated dielectric contribution are apparent, primarily at a shaping time of  $0.5 \mu\text{s}$  for temperatures of  $50 \text{ }^\circ\text{C}$  and  $-10 \text{ }^\circ\text{C}$ , and to a lesser extent, at long shaping times ( $6 \mu\text{s}$ ,  $10 \mu\text{s}$ ) for  $50 \text{ }^\circ\text{C}$  and  $20 \text{ }^\circ\text{C}$ . The apparent increase in dielectric noise at short shaping times may be attributable to an underestimate of  $N_{SWC}$  (Eq. 2.19), probably as a consequence of underestimating the total capacitance at the preamplifier input (i.e. the stray capacitance is not insignificant compared with those of the diode ( $3.1 \text{ pF}$ ) and JFET ( $2 \text{ pF}$ )). However, if the apparent increase in dielectric noise is attributable to underestimating the significance of the stray capacitance, it is not clear why measurements at short shaping times at  $20 \text{ }^\circ\text{C}$  do not show a comparable rise. The slight rise shown in calculated dielectric noise at long shaping times at  $20 \text{ }^\circ\text{C}$  could be attributed to an underestimate of the parallel white noise as a consequence of underestimating the leakage current of the JFET (the JFET's parameters were taken from its data sheet rather than being measured directly in the lab). The leakage currents of the JFET and detector are greater and more significant at higher temperature, explaining why little increase is observed in the parallel white noise at long shaping times in the  $-10 \text{ }^\circ\text{C}$  data.

A computer model of the noise which varies parameters such as the additional stray capacitances (capacitances in addition to those of the detector and JFET), to fit the experimental data, may produce better estimates for the individual noise contributions of the system, but the analysis presented here is sufficient to show that the dielectrics around the detector and JFET may be a very significant source of noise in the system

and that, if the dielectric noise could be reduced, the performance of the system is likely to improve.

To demonstrate the importance of reducing the dielectric noise contribution, **Fig. 4.13** shows the expected spectral resolution (FWHM) of diode D1 at 5.9 keV at a shaping time of 3  $\mu$ s, if the dielectric noise were to be eliminated. The spectral resolution data obtained for the current system (**Fig. 4.9**) is replotted in **Fig. 4.13** for comparison. If the dielectric noise could be eliminated, at 20 °C a spectral resolution (FWHM) at 5.9 keV of 380 eV could be obtained, compared with 1.07 keV with the current dielectric noise.

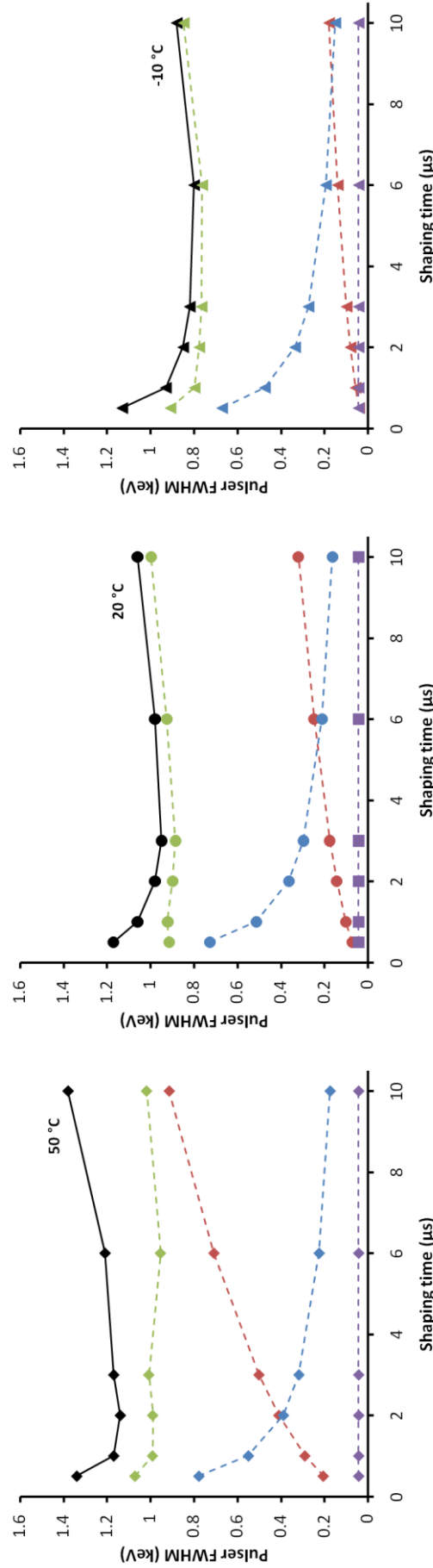


**Fig. 4.12.** Shaping time dependence of the pulser's FWHM (black symbols) at 50 °C (diamonds), 20 °C (circles) and -10 °C (triangles) with calculated noise components: dielectric noise (olive symbols), series white noise including induced gate current noise (blue symbols), total parallel white noise (red symbols) and I/f noise (mauve symbols).

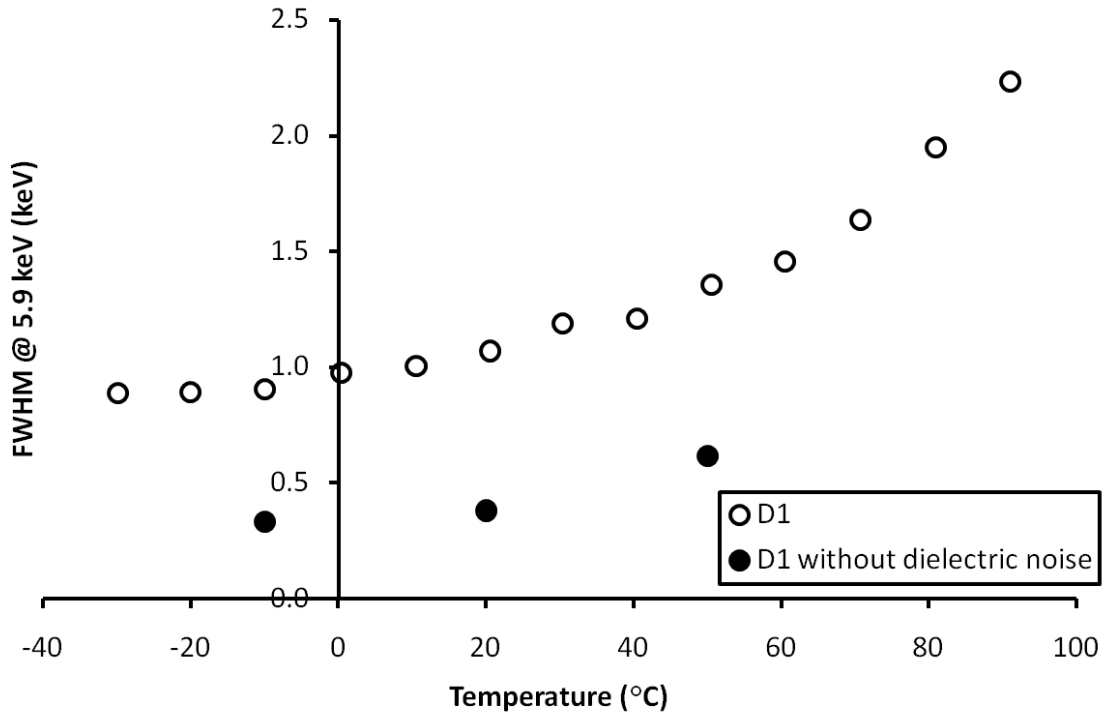


**Fig. 4.13.** The calculated spectral resolution (FWHM) of diode D1 if the dielectric noise was eliminated (filled circles). Also shown is the measured temperature dependence of the spectral resolution of diode D1 including dielectric noise (open circles).

## 4.7 Conclusions and discussion

$\text{Al}_{0.8}\text{Ga}_{0.2}\text{As}$   $\text{p}^+\text{-i-n}^+$  diodes have been shown to operate as photon counting spectroscopic X-ray detectors in non-avalanche mode at temperatures from  $-30\text{ }^\circ\text{C}$  to  $+90\text{ }^\circ\text{C}$  with promising spectral resolution (FWHM) of the full system (0.9 – 2.5 keV). Room temperature spectral measurements have shown spectral resolutions at 5.9 keV of 1.07 keV and 1.12 keV FWHM for the diodes studied. This is better than that of the previously reported  $\text{Al}_{0.8}\text{Ga}_{0.2}\text{As}$  devices when operated in non-avalanche mode ( $\sim 1.5$  keV FWHM at 5.9 keV) using the same preamplifier electronics as here (Lees et al., 2008).

Investigations of the noise sources contributing to the 1.07 keV spectral resolution of diode D1 have indicated that dielectric noise, thought to arise primarily from the diode and JFET packaging, is the most significant factor in limiting the spectral resolution of the current system. If the dielectric noise could be eliminated through improvements to the diode and JFET packaging (e.g. custom designed packaging, perhaps using ceramic

or Teflon mountings), spectral resolutions (FWHM at 5.9 keV) of 380 eV at 20 °C and ~500 eV at 50 °C are predicted (**Fig. 4.13**).

The spectral resolution of the diodes and system is currently modest compared with that achievable with a Si CCD cooled to -90 °C (130 eV FWHM at 5.9 keV) (Nakajima et al., 2005) and a silicon drift detector (SDD) operated at 20 °C (300 eV FWHM at 5.9 keV) (Lechner et al., 2001). SDDs may achieve good spectral performance at lower temperatures ( $\leq 20$  °C) but their spectral performance rapidly degrades at higher temperatures ( $\geq 20$  °C) (PNSensor GmbH, N.D.). Furthermore, avalanche multiplication in  $\text{Al}_{0.8}\text{Ga}_{0.2}\text{As}$  is increasingly well understood (Chapter 6) and recently it has been found that appreciable avalanche multiplication can be achieved at X-ray energies without introducing significant avalanche excess noise (§2.7.4) (Tan et al., 2011) (Lees et al., 2008). This may provide potential to exploit avalanche multiplication in  $\text{Al}_{0.8}\text{Ga}_{0.2}\text{As}$  APDs to achieve better resolutions than could be achieved with non-avalanche devices (Tan et al., 2011).

The uncooled  $\text{Al}_{0.8}\text{Ga}_{0.2}\text{As}$  detectors reported in this chapter show promise for X-ray spectroscopy at temperatures as high as +90 °C. An X-ray spectrometer based on  $\text{Al}_{0.8}\text{Ga}_{0.2}\text{As}$  detectors similar to those reported here, may find use in monitoring e.g. iron or molybdenum content in oils as a consequence of engine and oil wear, and in other applications where uncooled operation at high temperature is required, especially if the dielectric noise could be reduced.

Refinements to the design of the preamplifier and reduction of the diode leakage current through improved diode material quality, fabrication experience and mesa side wall passivation will all enable improvement upon the currently achieved resolutions, facilitating further progress towards the expected Fano limit of 155 eV at 5.9 keV (assuming  $F = 0.14$ ).

# Chapter 5 High temperature GaAs non-avalanche photodiodes

## 5.1 Introduction

Owens et al. (2001, 2002a) have reported a number of photon counting GaAs X-ray photodiodes operating at +23 °C with FWHM at 5.9 keV between 0.266 keV and 0.66 keV, and Erd et al. (2002) have reported the temperature dependence of the spectral resolution of a GaAs diode at 5.9 keV, for temperatures between +21 °C and -16 °C. However, the spectral resolution of GaAs photon counting soft X-ray photodiodes at temperatures much greater than 20 °C has not been reported. Considering the potential for GaAs photodiodes to operate at high temperature (it is a relatively wide band gap material;  $E_g = 1.43$  eV (NSM Archive, 2004)), this is surprising.

This chapter presents measurements of the temperature dependence of the spectral resolution and leakage current of GaAs non-avalanche photon counting  $p^+i-n^+$  diodes over a temperature range of +80 °C to -30 °C, together with an analysis of the noise components of the system. Also presented are experimental and computer modelling results which show  $^{109}\text{Cd}$  X-ray spectra obtained with the GaAs devices and the detector's internal X-ray fluorescence that results from higher energy ( $E \geq$  Ga K shell binding energy, 10.367 keV) X-ray photon interactions with the detector.

## 5.2 Diode design and fabrication

A GaAs  $p^+i-n^+$  wafer was grown on a GaAs substrate by molecular beam epitaxy at the EPSRC National Centre for III-V Technologies, University of Sheffield, UK, as per §4.3. High efficiency soft X-ray detection requires a very thin entrance window and a suitably thick absorption (depletion) layer; the GaAs wafer was designed to have a 2  $\mu\text{m}$  thick  $i$  layer and a thin  $p^+$  layer (0.2  $\mu\text{m}$ ). **Table 5.1** shows the GaAs wafer layer thicknesses and doping densities. Circular mesa diodes of radii 25, 50, 100 and 200  $\mu\text{m}$  were fabricated from this wafer by researchers at University of Sheffield using

photolithography. The diode layout was the same as the  $\text{Al}_{0.8}\text{Ga}_{0.2}\text{As}$  diode layout (Fig. 4.3). The GaAs wafers were passivated with SU-8 (an epoxy-based material commonly used for passivation and photoresist applications) (Chollet, 2009) to minimise surface leakage current.

Layer	Material	Thickness ( $\mu\text{m}$ )	Dopant	Type	Doping Density ( $\times 10^{18} \text{ cm}^{-3}$ )
1	GaAs	0.01	Be	$\text{p}^{++}$	10
2	GaAs	0.2	Be	$\text{p}^+$	2.0
3	GaAs	2	Undoped		< 0.01
4	GaAs	0.1	Si	$\text{n}^+$	2.0
5	GaAs	0.2	Si	$\text{n}^+$	2.0
Substrate	$\text{n}^+$ GaAs	500			

**Table 5.1.** Layer details of the GaAs wafer used in this work.

A graph showing the quantum efficiency of the devices, assuming only charge generated in the i layer (layer 3) is collected, is shown in Fig. 5.1, along with the calculated quantum efficiency if the same structure of diode were made from silicon, for comparison. The calculated efficiencies of the GaAs diodes at 5.9 keV ( $\text{Mn K}\alpha$ ) and 22.16 keV ( $\text{Ag K}\alpha_1$ ) are calculated to be 0.152 and 0.034, respectively. These are much better than for the same structure made from silicon (0.067 at 5.9 keV, 0.001 at 22.16 keV). However, the efficiency of the GaAs diodes is lower than may be achievable with a thicker (40  $\mu\text{m}$ , ~0.95 efficiency at 5.9 keV) GaAs diode, perhaps grown by CVD or LPE, or a very thick (500  $\mu\text{m}$ ) silicon device (~0.99 efficiency at 5.9 keV). At very soft X-ray energies, it is the thickness of the  $\text{p}^+$  layer (0.21  $\mu\text{m}$ ) rather than the thinness of the i layer that reduces the quantum efficiency of the GaAs devices. At an X-ray energy of 2 keV, an efficiency of 0.7 is predicted for GaAs diodes of the current design, but if the thickness of the  $\text{p}^+$  layer were halved, this would increase to 0.81.

The high field region is considered to be restricted to the i layer at normal operating bias; the high doping concentrations in the  $\text{p}^+$  and  $\text{n}^+$  layers limit the extension of the depletion region into these layers to a total of  $3.6 \times 10^{-3} \mu\text{m}$  at 10 V (Eq. 2.3 using Table 5.1), which is small compared with the thickness of the i layer (2  $\mu\text{m}$ ). The diodes were mounted in a TO-5 package (gold plated, 9 mm diameter, 12 pins,

see **Fig. 4.1**). The capacitance of the 100  $\mu\text{m}$  radius GaAs detectors was measured at University of Sheffield as 1.94 pF at 10 V.

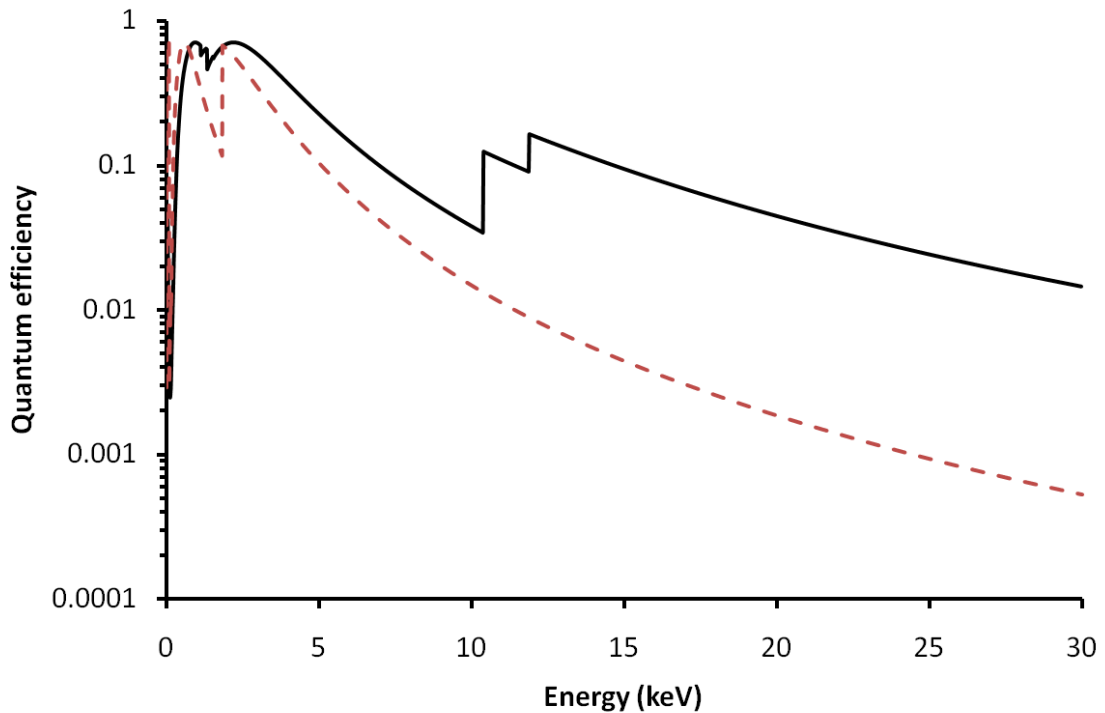


**Fig. 5.1.** The calculated quantum efficiency of the GaAs  $p^+i-n^+$  diodes with varying X-ray energy (solid black line). The discontinuities are the Ga and As K L edges (see **Tables 1.1a and 1.2a**). For comparison the calculated quantum efficiency of the same structure of diode made from silicon (K edge = 1.839 keV) is also shown (dashed red line).

### 5.3 Leakage current measurements

Using the same equipment and techniques as §4.4, leakage current verses reverse bias ( $I$ - $V$ ) measurements of nine 100  $\mu\text{m}$  radius GaAs diodes were made at room temperature (20 °C). The  $I$ - $V$  data ( $\leq 40$  V) for the diodes is shown in **Fig. 5.2**. For the reverse bias range shown, the leakage current's dependence on reverse bias is broadly linear (coefficient of determination,  $R^2 > 0.99$ ) for all devices with the exception of diode D6 which shows a slight exponential trend at higher reverse biases, possibly due to slight imperfections in this device which may have arisen during fabrication or wire bonding.

At a typical operating reverse bias of 10 V at 20 °C, the spread of leakage currents was from 5.9 pA (current density =  $1.878 \times 10^{-8}$  A/cm<sup>2</sup>) to 19.4 pA (current density =  $6.175 \times 10^{-8}$  A/cm<sup>2</sup>). The cause of such a wide spread of leakage currents is currently

unknown but probably attributable to a combination of wafer quality and/or small variations in individual diode fabrication. The current densities at 10 V for the diodes reported here are higher at 20 °C than for some GaAs pixel detectors previously reported at 10 V at 30 °C ( $\sim 4 \times 10^{-9}$  A/cm<sup>2</sup>) (Bertuccio et al., 2003).

The temperature,  $T$ , dependence of the leakage current of GaAs diode D9, which had a leakage current (12.2 pA) close to the mean (11.5 pA) at 10 V, is shown in **Fig. 5.3**. For comparison, the figure also shows data from two previously reported Al<sub>0.8</sub>Ga<sub>0.2</sub>As diodes (Chapter 4). Although there are some differences in the measured leakage current at high temperatures, the trend is very similar in the Al<sub>0.8</sub>Ga<sub>0.2</sub>As and GaAs diode types. At the nominal operating voltage, 10 V, the temperature dependence of the leakage current for the GaAs devices is similar to that reported for the Al<sub>0.8</sub>Ga<sub>0.2</sub>As devices (§4.4).

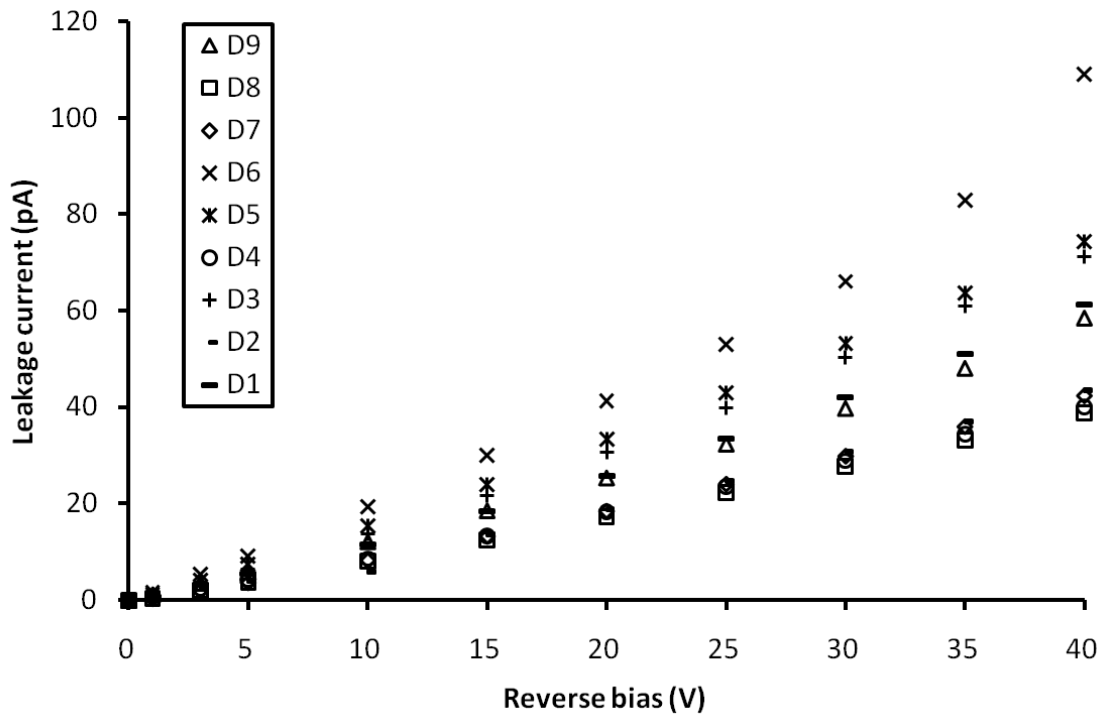


**Fig. 5.2.**  $I$ - $V$  data for nine (D1 – D9) 100  $\mu$ m radius GaAs diodes at room temperature.

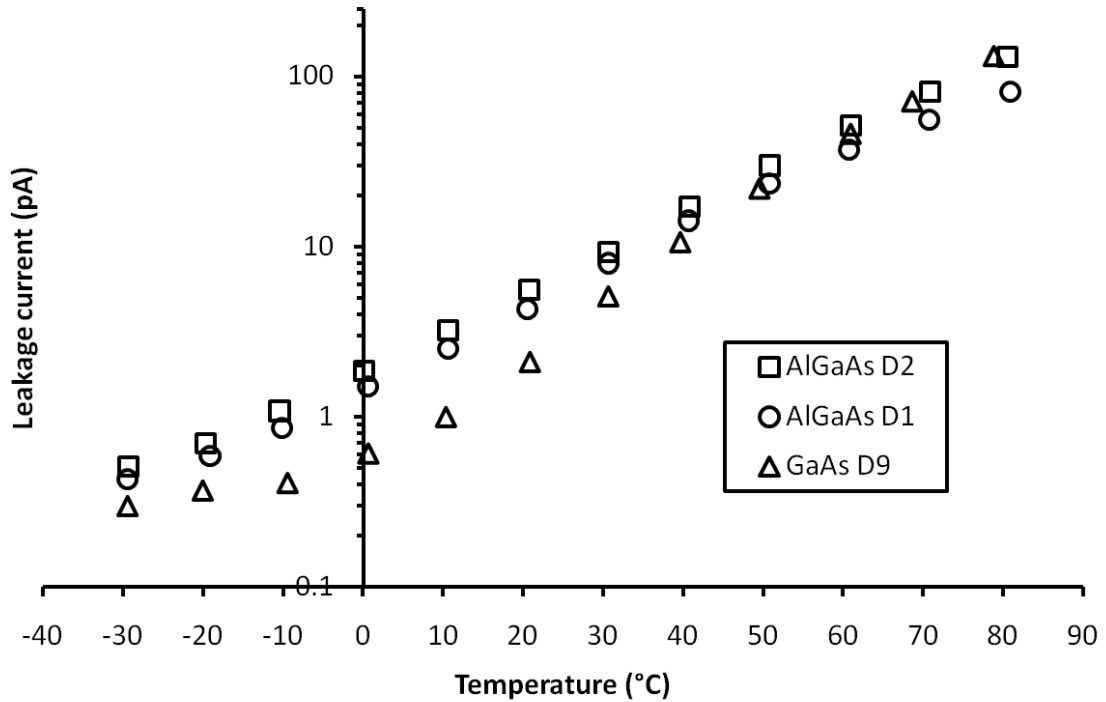


**Fig. 5.3.** The temperature dependence of the leakage current at 10 V of GaAs diode D9 (triangles), compared with the two previously reported  $Al_{0.8}Ga_{0.2}As$  diodes, D1 (circles) and D2 (squares) (Chapter 4).

#### 5.4 $^{55}Fe$ X-ray spectral measurements

The GaAs diodes were individually reverse biased at 10 V and X-ray spectral measurements were obtained at temperatures from +80 to -30 °C in the same manner as §4.5. The input discriminator level of the MCA was adjusted (1.4 keV) to minimise the number of events from the zero energy noise peak.

An  $^{55}Fe$  spectrum taken at 20 °C using GaAs diode D9 is shown in **Fig. 5.4** along with a comparable spectrum from  $Al_{0.8}Ga_{0.2}As$  diode D2 (**Fig. 4.8**). The peak-to-valley ( $P/V$ ) ratio for the GaAs D9 spectrum is 0.04. This is the same as that seen by Owens et al. (2001, 2002a) and Erd et al. (2002) with their GaAs diodes at -40, -20 and +5 °C respectively ( $P/V = 0.04$ , in each case). There is less low energy tailing with GaAs D9 than there was with the  $Al_{0.8}Ga_{0.2}As$  diodes ( $Al_{0.8}Ga_{0.2}As$  diode  $P/V$  ratio = 0.13). The increase in counts above the low energy tail continuum between 4 keV and 2 keV seen in the  $Al_{0.8}Ga_{0.2}As$  D1 spectrum is from the tail of the zero energy noise peak which has not been entirely eliminated by the low energy cut off (§4.5).

The improvement in low energy tailing for the GaAs diodes compared with that reported for  $\text{Al}_{0.8}\text{Ga}_{0.2}\text{As}$  D1 is hypothesised to be primarily due to more complete charge collection in GaAs D9 as a result of better crystal quality. However, the less significant tail from the zero energy noise peak in the GaAs spectrum also serves to reduce counts in the valley. The zero energy noise peak tail is less significant in the GaAs spectrum because GaAs has a lower electron-hole pair creation energy (4.2 eV, (Owens and Peacock, 2004) than  $\text{Al}_{0.8}\text{Ga}_{0.2}\text{As}$  (5.25 eV). This improves the system gain (charge generated per eV of photon energy) leading to a greater separation between the 5.9 keV peak and zero energy noise peak.

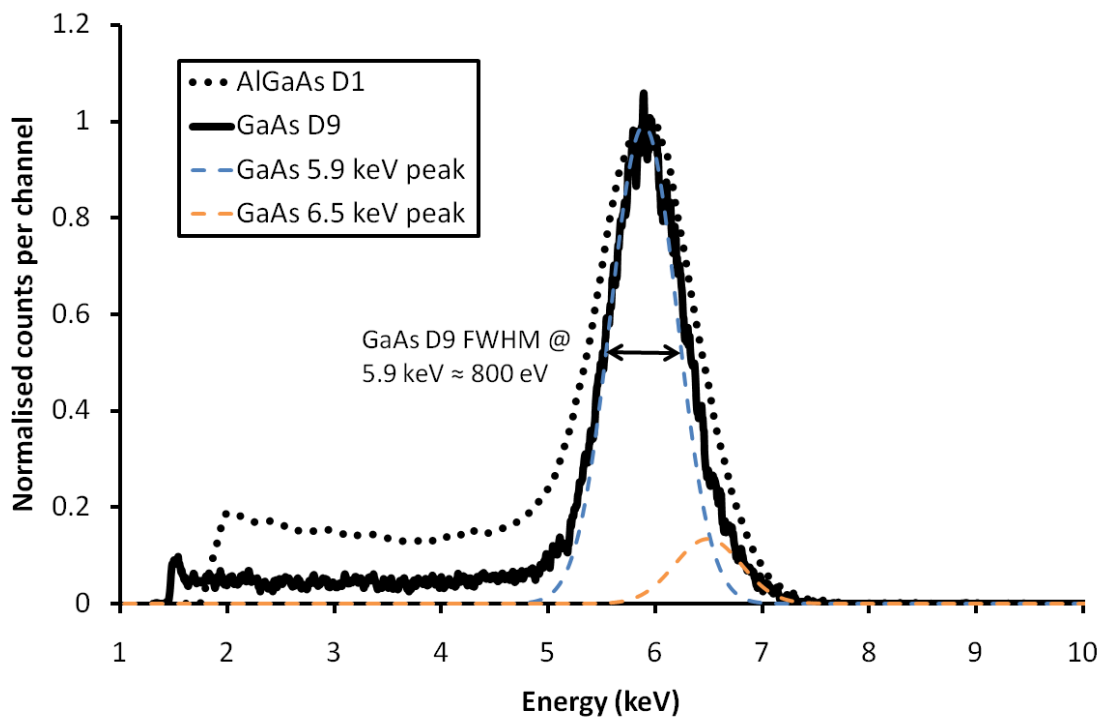


**Fig. 5.4.** Typical  $^{55}\text{Fe}$  spectra taken at 20 °C with GaAs diode D9 (black solid line) and  $\text{Al}_{0.8}\text{Ga}_{0.2}\text{As}$  D1 (black dotted line). The two Gaussian peaks fitted to the GaAs data representing the Mn  $K\alpha$  (5.9 keV) and  $K\beta$  (6.5 keV) X-ray lines (blue and orange dashed lines, respectively) are not resolved and so contribute to a single peak.

The temperature dependence of the spectral resolution (FWHM) for GaAs diode D9 is shown in **Fig. 5.5**. Data from GaAs devices previously reported (Owens et al., 2001) (Owens et al., 2002a) (Erd et al., 2002) are also presented in the figure along with the data for  $\text{Al}_{0.8}\text{Ga}_{0.2}\text{As}$  D1 (§4.5). The spectral resolution of the GaAs diodes in Owens et al. (2001) was reported for two different preamplifiers; both data sets are reproduced in **Fig. 5.5**.

Over the temperature range, +80 to -30 °C, the spectral resolution measured with GaAs D9 is better than that measured with the  $\text{Al}_{0.8}\text{Ga}_{0.2}\text{As}$  diodes (Chapter 4). For example, at 20 °C the FWHM at 5.9 keV with GaAs diode D9 is 0.8 keV compared to 1.07 keV for  $\text{Al}_{0.8}\text{Ga}_{0.2}\text{As}$  diode D1.

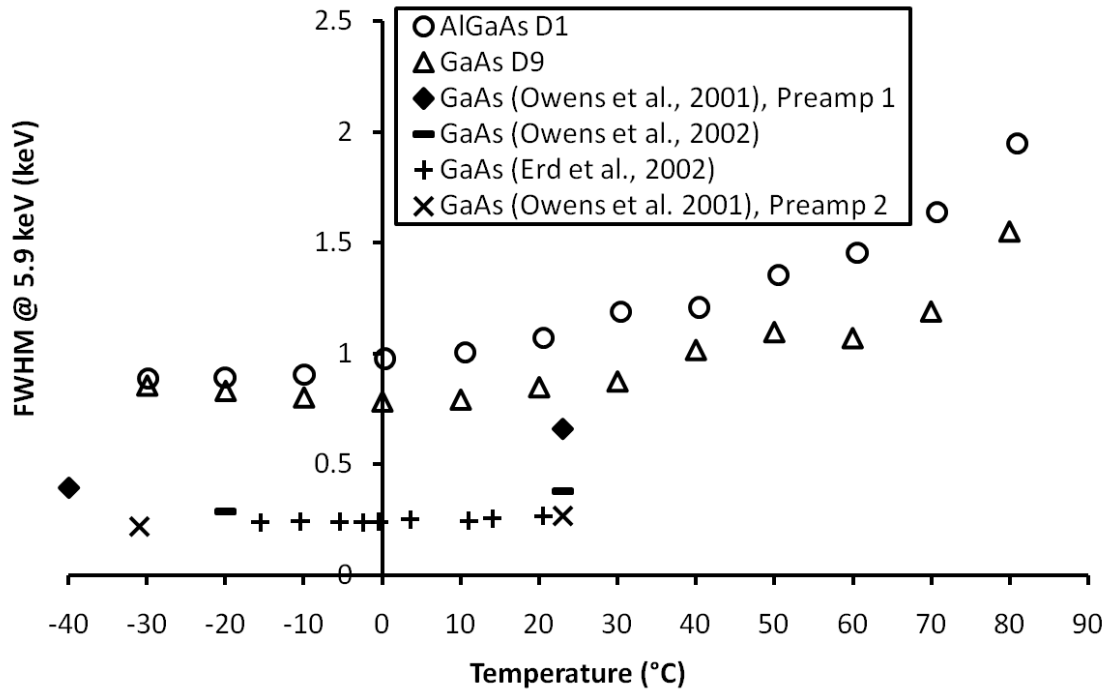


**Fig. 5.5.** The mean spectral resolution (FWHM at 5.9 keV) measured at each temperature with GaAs diode D9 (open triangles),  $\text{Al}_{0.8}\text{Ga}_{0.2}\text{As}$  diode D1 (open circles) and previously reported GaAs data: Owens et al. (2001) with preamplifier 1 (solid diamonds), Owens et al. (2001) with preamplifier 2 (x symbols), Owens et al. (2002a) (dashes), Erd et al. (2002) (+ symbols).

The spectral resolutions reported by Owens et al. and Erd et al. for their GaAs devices are significantly better (0.66 keV and 0.266 keV (Owens et al., 2001), 0.380 keV (Owens et al., 2002a), and 0.267 keV (Erd et al., 2002) at 23 °C) than the GaAs diodes reported here. Their improved resolution is primarily attributed to the lower electronics noise associated with their devices' readout electronics; the pulser line FWHM (see §5.5.2) used to measure the electronics noise as reported by Owens et al. and Erd et al. were 0.470 keV and 0.163 keV (Owens et al., 2001), 0.340 keV (Owens et al., 2002a) and 0.220 keV (Erd et al., 2002) compared with 0.760 keV at 20 °C for the GaAs diodes reported here, thus showing the importance of low noise electronics in achieving good spectral resolutions with semiconductor detectors.

The improvement in spectral resolution of GaAs D9 compared with  $\text{Al}_{0.8}\text{Ga}_{0.2}\text{As}$  D1 can be attributed primarily to the increased gain of the GaAs system; GaAs has a lower electron-hole pair creation energy (4.2 eV) than  $\text{Al}_{0.8}\text{Ga}_{0.2}\text{As}$  (5.25 eV) which leads to larger numbers of charge carriers generated for the same input X-ray photon energy. This improves the gain of the system and, consequently, the spectral resolution. As is the case for the  $\text{Al}_{0.8}\text{Ga}_{0.2}\text{As}$  diodes, the spectral resolution achieved with the GaAs diodes is much poorer than would be expected if the system were Fano limited. For GaAs, given a Fano factor of 0.12 (Bertuccio et al., 2003), the Fano limited resolution at 5.9 keV would be 129 eV FWHM, which is better than  $\text{Al}_{0.8}\text{Ga}_{0.2}\text{As}$  (155 eV FWHM at 5.9 keV, assuming  $F = 0.14$ ).

## 5.5 Noise analysis

### 5.5.1 Initial measurements

The noise contributions to the GaAs diode spectra FWHM total noise,  $N_T$ , were assessed similarly to those for the  $\text{Al}_{0.8}\text{Ga}_{0.2}\text{As}$  spectra (§4.6): the detector's parallel white noise contribution,  $N_{PW}$ , was calculated for each temperature (Eqs. 2.16 and 2.17, with  $A_3 = 2$ ) and subtracted in quadrature. The expected Fano noise contribution,  $N_F$ , was similarly subtracted. Assuming broadening of the FWHM due to charge trapping noise is insignificant (**Fig. 5.4**), the remainder can be attributed to the rest of the electronics noise contribution,  $N_E$ . The contributions and total for GaAs D1 are shown in **Fig. 5.6** together with the data for  $\text{Al}_{0.8}\text{Ga}_{0.2}\text{As}$  D2 for comparison. The noise contribution from the Fano noise is small compared with  $N_E$ , as is the detector's parallel white noise, which is even less significant at lower temperatures ( $< 40$  °C) than the Fano noise. From the relative insignificance of the detector's parallel white noise, we can see that the detector's leakage current (which contributes to the parallel white noise) is not presently a limiting factor in the spectral resolution achievable with the detectors in this temperature range. Rather, it appears that it is one or more of the noise sources remaining in  $N_E$  which is limiting the spectral resolution.

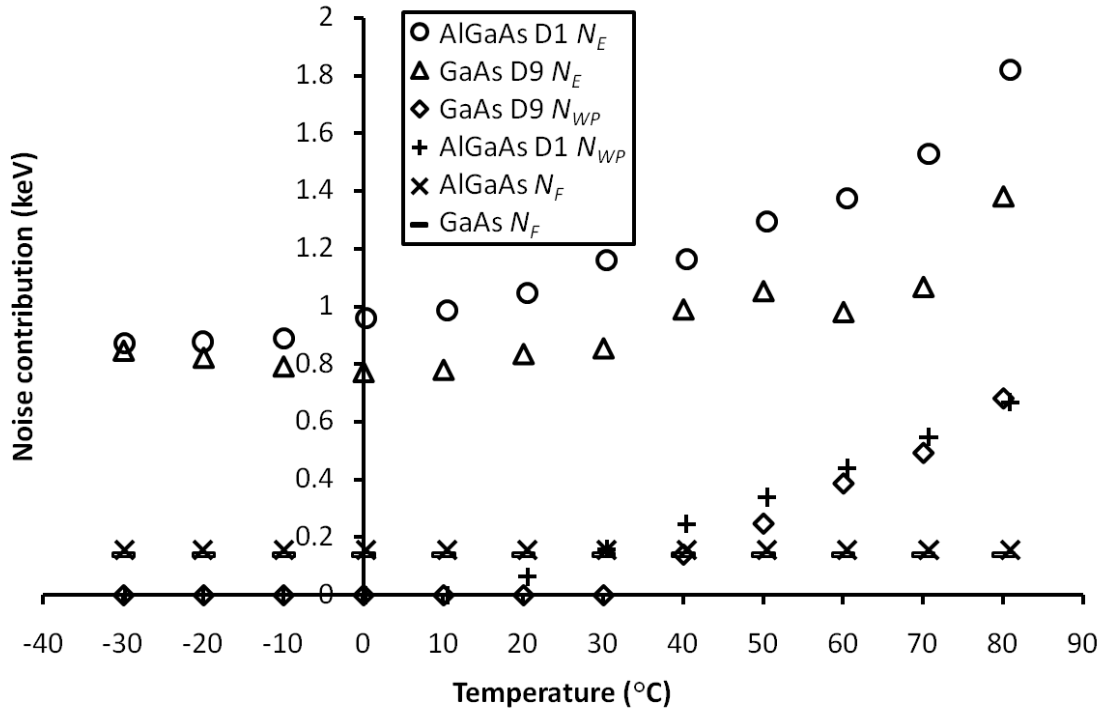


**Fig. 5.6.** The calculated noise contributions for the system as a function of operating temperature for both GaAs D9 and  $Al_{0.8}Ga_{0.2}As$  D1 diodes. GaAs D9: remaining electronics ( $N_E$ ) (open triangles), detector parallel white noise ( $N_{PW}$ ) (open diamonds), Fano noise ( $N_F$ ) (open dashes).  $Al_{0.8}Ga_{0.2}As$  D1: remaining electronics ( $N_E$ ) (open circles), detector parallel white noise ( $N_{PW}$ ) (+ symbols), Fano noise ( $N_F$ ) (× symbols).

### 5.5.2 Shaping time measurements

To analyse the electronics noise contributions further and deduce their origins, the same method was used as was employed for the  $Al_{0.8}Ga_{0.2}As$  devices (§4.6.2): a pulse generator was connected to the system (**Fig. 4.7**). By measuring the FWHM of the peak produced by the pulse generator, the performance of the preamplifier electronics coupled to the GaAs detector can be measured. The performance of the electronics depends on the leakage current and capacitance of the detector (Chapter 2), so it was necessary to keep the GaAs diode connected and reverse biased. As per §4.6.2, spectra at 50, 20 and  $-10$  °C were accumulated with shaping times of 0.5, 1, 2, 3, 6 and 10  $\mu s$  and energy calibrated using the zero energy noise peak and the combined Mn  $K\alpha$  Mn  $K\beta$  peaks (**Fig. 5.4**) from the  $^{55}Fe$  source which was used to illuminate the diode. The same values were used for the parameters characterising the electronics as were used in §4.6.2 (Bertuccio, Pullia & DeGeronimo, 1996) (Gatti et al., 1990). The total

capacitance at the preamplifier input,  $C_T$ , was assumed to be dominated by the capacitance of the detector ( $C_d = 1.94$  pF) and JFET ( $C_i = 2$  pF).

The FWHM of the pulser peak,  $N_T$ , along with the calculated contributions to this overall noise, arising from total (detector and JFET) parallel white noise,  $N_{PW}$  (§2.6.3), series white noise including induced gate current noise,  $N_{SWC}$  (§2.6.4 and §2.6.7),  $1/f$  noise,  $N_{1/f}$  (§2.6.5) and dielectric noise ( $N_D^2 = N_T^2 - N_{PW}^2 - N_{SWC}^2 - N_{1/f}^2$ ) components can be seen in **Fig. 5.7**. The JFET's white parallel noise contribution was estimated to be 0.10, 0.11 and 0.50 keV at -10, 20 and 50 °C, respectively (Siliconix, 1997). Even though the preamplifier electronics are the same as were used in Chapter 4, their measured performance is different with the GaAs detector because of the diode's different properties (compare **Fig. 5.7** and **Fig. 4.12**). As expected from their  $\tau$  dependences, the parallel white contribution (Eqs. 2.16 and 2.17) still reduces with increasing shaping time, the series white contribution (Eqs. 2.18 and 2.19) increases and the  $1/f$  contribution (Eq. 2.20) remains constant. The shaping time at which the parallel white and series white noise contributions intersect lengthens with decreasing temperature ( $\tau = 2$   $\mu$ s at 50 °C,  $\tau = 5.4$   $\mu$ s at 20 °C,  $\tau = 7.8$   $\mu$ s at -10 °C) similarly to that found with the  $\text{Al}_{0.8}\text{Ga}_{0.2}\text{As}$  detector, but the GaAs system's optimum shaping time dependence on temperature is less clear because the minima representing the optimum shaping time at 20 °C and -10 °C are not so well defined. However, the parallel white and series white data suggest a lengthening of optimum shaping time with decreasing temperature similarly to the  $\text{Al}_{0.8}\text{Ga}_{0.2}\text{As}$  data (**Fig. 4.12**).

The calculated dielectric noise contribution is broadly constant with varied shaping time as expected (Eq. 2.21 and §4.6.2), although there are slight increases in the calculated component at short shaping times. This trend is consistent with an underestimate of the series white noise and  $1/f$  noise contributions as a consequence of an underestimate of  $C_T$ . That  $C_T$  is underestimated in this way (it had been assumed that  $C_T = C_d + C_i$ ) is not surprising given the significance of the estimated dielectric noise contribution and the stray capacitance that such a contribution presupposes. As was the case for the  $\text{Al}_{0.8}\text{Ga}_{0.2}\text{As}$  diode system, a computer model which varies parameters such as the stray capacitance to fit the experimental data, may enable the dielectric noise contribution to be better calculated. Nevertheless, the analysis presented here is sufficient to show that the dielectric noise contribution is significant and that future work to improve the spectral resolution would be well targeted by improving the diode and JFET packaging.

A graph showing the expected spectral resolution (FWHM) at 5.9 keV (with  $\tau = 3 \mu\text{s}$ ), if the dielectric noise could be eliminated, is shown in **Fig. 5.8** and compared with the same data for  $\text{Al}_{0.8}\text{Ga}_{0.2}\text{As}$  D1 (**Fig. 4.11**) and those presented in **Fig. 5.5**.

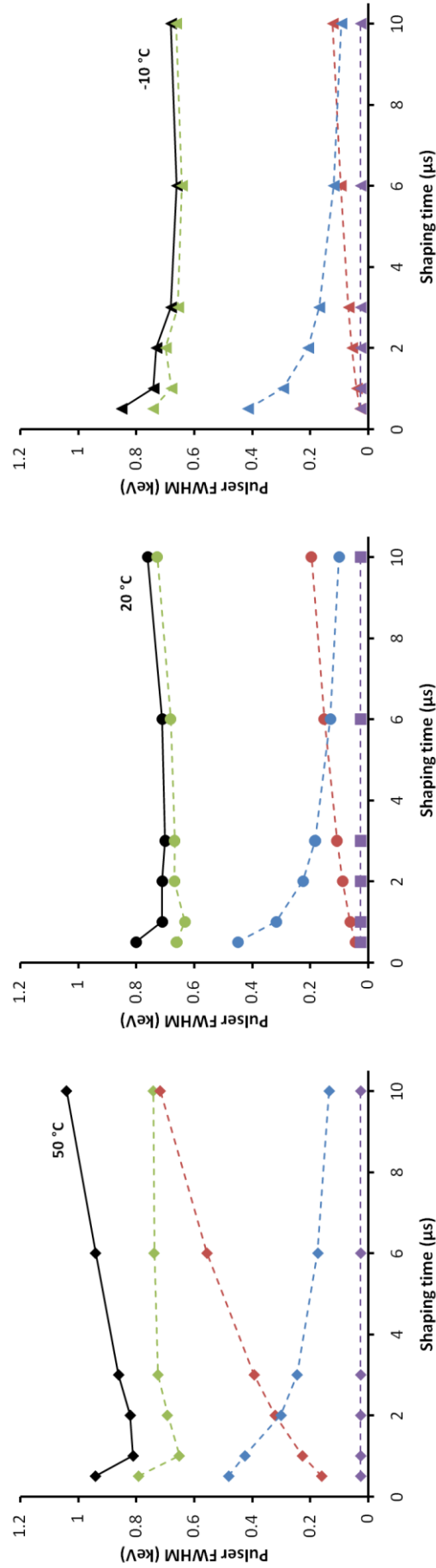


**Fig. 5.7.** Shaping time dependence of the pulser's FWHM (black symbols) at 50 °C (diamonds), 20 °C (circles) and -10 °C (triangles) with calculated noise components: dielectric noise (olive symbols), series white noise including induced gate current noise (blue symbols), total parallel white noise (red symbols) and I/f noise (mauve symbols).

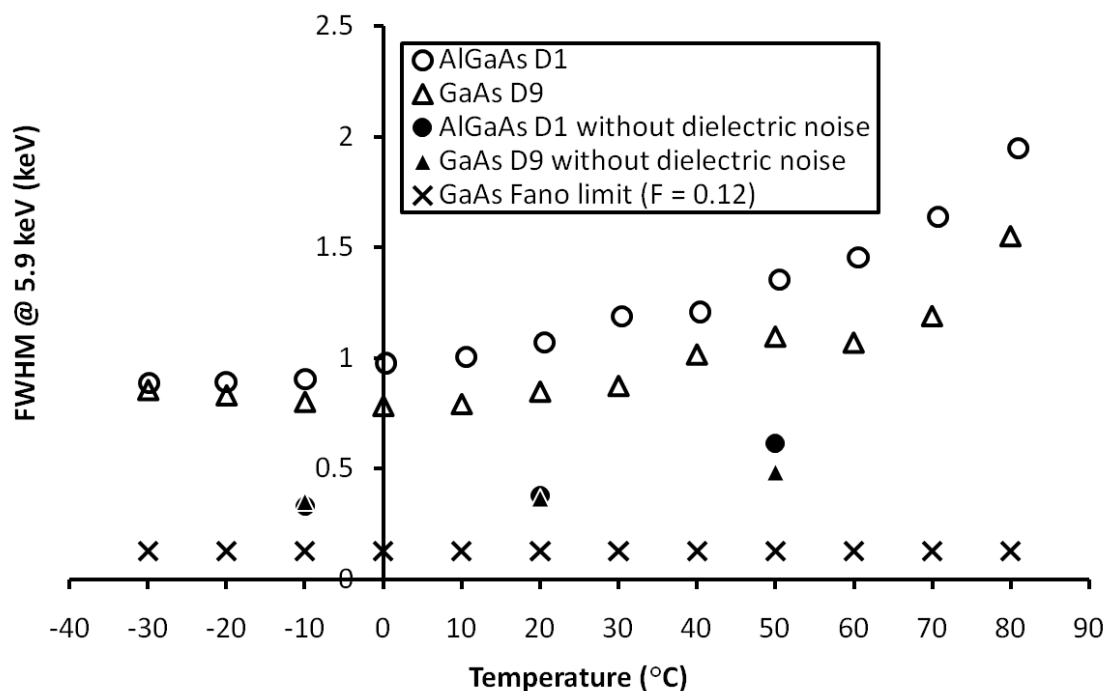


**Fig. 5.8.** The temperature dependence of the expected spectral resolution (FWHM) at 5.9 keV of GaAs diode D9 if the estimated dielectric noise was eliminated (filled triangles). Also shown are the measured spectral resolution of GaAs diode D9 including dielectric noise (open triangles), the expected spectral resolution (FWHM) at 5.9 keV of diode D1 if the dielectric noise was eliminated (filled circles) and the measured spectral resolution (FWHM) of  $Al_{0.8}Ga_{0.2}As$  diode D1 including dielectric noise (open circles). The GaAs Fano limit (assuming  $F = 0.12$  and  $\omega_{EHP} = 4.2$  eV across the measured temperature range) is also shown ( $\times$  symbols).

## 5.6 $^{109}Cd$ spectra and GaAs diode internal X-ray fluorescence

To measure the performance of the GaAs diodes at higher X-ray energies, spectra were accumulated at 20 °C using a  $^{109}Cd$  (~0.06 MBq) source with a 254  $\mu m$  thick beryllium window, giving characteristic Ag  $K\alpha$  (22.16 and 21.99 keV) and Ag  $K\beta$  (24.94, 24.99 and 25.46 keV) X-ray lines. The majority of the Ag  $L\alpha$  (2.984 and 2.978 keV) X-ray emissions from the  $^{109}Cd$  are screened from the detector by the source's beryllium window (transmission through 254  $\mu m$  thick Be at 2.9 keV = 0.007). A typical spectrum obtained at 20 °C with the  $^{109}Cd$  source is shown in **Fig. 5.9**. The efficiency of the GaAs diodes is low at Ag  $K\alpha$  and  $K\beta$  energies (see **Fig. 5.1**); the accumulation time for this spectrum was 14 days. The low energy threshold was set at 2 keV to minimise counts from the tail of the zero energy noise peak. Ag  $K\alpha$  and  $K\beta$  photons

emitted from the source are able to fluoresce the Ga and As atoms in the detector (the energies of the Ag K $\alpha$  and K $\beta$  lines is greater than the K shell electron binding energies of Ga and As). Consequently the Ga K $\alpha$  and As K $\alpha$  fluorescence and escape peaks (§2.2.2) can be seen in the spectrum in addition to the characteristic Ag K emission lines of  $^{109}\text{Cd}$ . The Ag K $\alpha_1$  and K $\alpha_2$  peaks are too similar in energy to be individually resolved so they both contribute to a single peak. The same is true for the Ag K $\beta$  lines which also contribute to a single peak. The peak from the small proportion of Ag L $\alpha$  photons which were transmitted through the window is obscured by noise, so a distinct Ag L $\alpha$  peak does not appear in the spectrum. Three small peaks (Ni K $\alpha$ , Fe K $\alpha$  and Cr K $\alpha$ ) from fluorescence of the stainless steel source capsule are visible at 7.47, 6.4 and 5.4 keV, respectively. The FWHM of the combined Ag K $\alpha_1$  and K $\alpha_2$  peak is  $\approx 850$  eV, implying individual FWHMs for Ag K $\alpha_1$  and K $\alpha_2$  = 800 eV (**Fig. 5.9**).

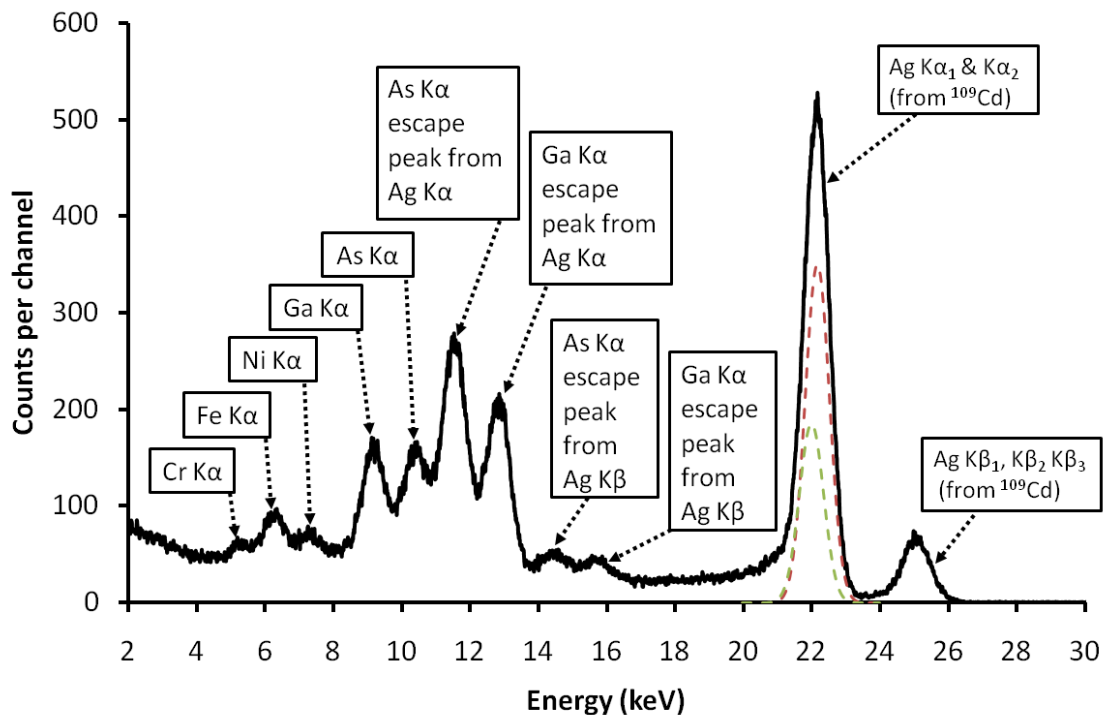


**Fig. 5.9.** A  $^{109}\text{Cd}$  spectrum accumulated with GaAs D1 at 20 °C over 14 days. Peaks from the characteristic groups of Ag K $\alpha$  and K $\beta$  X-ray lines from the source are visible, but the individual Ag K $\alpha$  (K $\alpha_1$  – red dashed line; K $\alpha_2$  – olive dashed line) and K $\beta$  lines are not resolved. Fluorescence and escape peaks from Ag K photon interactions with Ga and As atoms of the detector are apparent as are fluorescence peaks (Ni K $\alpha$ , Fe K $\alpha$  and Cr K $\alpha$ ) from the stainless steel source capsule. The K edges and fluorescence yields of Cr, Fe, Ni, Ga and As are given in **Table 5.2**, and emission lines and radiative rates for each element in **Tables 5.3a-e**.

Element	Cr	Fe	Ni	Ga	As
<b>K edge (keV)</b>	5.989	7.112	8.333	10.367	11.867
<b>K fluorescence yield</b>	0.281	0.336	0.410	0.543	0.581

*Table 5.2. K shell fluorescence yields and edges for Cr, Fe, Ni, Ga and As (Brunetti et al., 2004).*

	<b>K<math>\alpha_1</math></b>	<b>K<math>\alpha_2</math></b>	<b>K<math>\beta_1</math></b>	<b>K<math>\beta_3</math></b>
<b>Line energy (keV)</b>	9.252	9.225	10.264	10.260
<b>Radiative rate</b>	0.577	0.294	0.083	0.043

*Table 5.3a. Gallium X-ray fluorescence lines and fractional radiative rates (Brunetti et al., 2004).*

	<b>K<math>\alpha_1</math></b>	<b>K<math>\alpha_2</math></b>	<b>K<math>\beta_1</math></b>	<b>K<math>\beta_3</math></b>
<b>Line energy (keV)</b>	10.543	10.507	11.726	11.720
<b>Radiative rate</b>	0.571	0.294	0.086	0.044

*Table 5.3b. Arsenic X-ray fluorescence lines and fractional radiative rates (Brunetti et al., 2004).*

	<b>K<math>\alpha_1</math></b>	<b>K<math>\alpha_2</math></b>	<b>K<math>\beta_1</math></b>	<b>K<math>\beta_3</math></b>
<b>Line energy (keV)</b>	7.478	7.461	8.265	8.265
<b>Radiative rate</b>	0.580	0.297	0.081	0.041

*Table 5.3c. Nickel K emission line energies and radiative rates (Brunetti et al., 2004).*

	<b>K<math>\alpha_1</math></b>	<b>K<math>\alpha_2</math></b>	<b>K<math>\beta_1</math></b>	<b>K<math>\beta_3</math></b>
<b>Line energy (keV)</b>	6.404	6.391	7.058	7.058
<b>Radiative rate</b>	0.581	0.297	0.081	0.041

*Table 5.3d. Iron K emission line energies and radiative rates (Brunetti et al., 2004).*

	<b>K<math>\alpha_1</math></b>	<b>K<math>\alpha_2</math></b>	<b>K<math>\beta_1</math></b>	<b>K<math>\beta_3</math></b>
<b>Line energy (keV)</b>	5.415	5.406	5.947	5.947
<b>Radiative rate</b>	0.585	0.298	0.078	0.040

*Table 5.3e. Chromium K emission line energies and radiative rates (Brunetti et al., 2004).*

The Monte Carlo model described in Chapter 3 was used to simulate a GaAs p<sup>+</sup>-i-n<sup>+</sup> diode illuminated with a <sup>109</sup>Cd radioisotope X-ray source. In the simulation, the X-ray

source was defined to emit the photons shown in **Table 5.4**. These numbers take into account the relative emission probabilities of  $^{109}\text{Cd}$  (**Table 5.5**) and the attenuation of the X-rays through the Be window of the source capsule. The model was configured so that the X-ray source uniformly illuminated the face of a square  $200\ \mu\text{m} \times 200\ \mu\text{m}$  diode with  $p^+$  layer thickness =  $0.21\ \mu\text{m}$ ,  $i$  layer thickness =  $2\ \mu\text{m}$  and  $n^+$  layer thickness =  $500.3\ \mu\text{m}$  (consisting of  $0.3\ \mu\text{m}$  of  $n^+$  epilayer and  $500\ \mu\text{m}$  of  $n^+$  substrate) (**Table 5.1**). The model simulates noise (§2.6) totalling  $81\ e^-$  r.m.s., giving a FWHM of  $800\ \text{eV}$  at  $22.16\ \text{keV}$ , as experimentally measured. In the simulation it was assumed that all charge in the  $i$  layer was collected, whereas all charge in the  $n^+$  layer was lost ( $r_h = 0$ , see §3.4). The electron recombination length,  $r_e$ , used for the  $p^+$  layer was  $0.16\ \mu\text{m}$  (assumed to be similar to that for  $\text{Al}_{0.8}\text{Ga}_{0.2}\text{As}$   $p^+$  (Chapter 6)). The fluorescence yields and X-ray edges of Ga and As, given in **Table 5.2**, along with their X-ray lines and radiative rates in **Tables 5.3a & 5.3b** (Brunetti et al., 2004) were entered into the model. For simplicity, only K shell fluorescence is currently included in the model; L shell fluorescence will be included in future versions. **Fig. 5.10** compares the simulated spectra which resulted from the simulation and experiment. The spectra have been normalised to the height of the Ag  $K\alpha$  peak in the experimental spectrum.

Energy (keV)	Number of photons	Simulating
22.16	$4 \times 10^5$	Ag $K\alpha_1$
21.99	$2.11964 \times 10^5$	Ag $K\alpha_2$
25.00	$1.30298 \times 10^5$	Combined Ag $K\beta$
2.98	584	Combined Ag $L\alpha$

**Table 5.4.** Emissions from the  $^{109}\text{Cd}$  X-ray source in the computer simulation (see text).

Emission	Energy (keV)	Relative emission probability
Ag $K\alpha_1$	22.16	1
Ag $K\alpha_2$	21.99	0.530
Combined Ag $K\beta$	25.00	0.325
Combined Ag $L\alpha$	2.98	0.189

**Table 5.5.** Relative emission probabilities of  $^{109}\text{Cd}$  (Xiaolong et al., 2010).

The experimentally observed Ag  $K\alpha$ ,  $K\beta$  peaks are very well reproduced by the model. The locations of the Ga  $K\alpha$  and As  $K\alpha$  fluorescence and escape peaks in the simulated spectrum match the experimental data, but there are differences in the magnitude of the peaks. There are proportionally fewer fluorescence and escape events in the simulated case than in the experimental case. In the experimental case the source illuminated the whole wafer chip (**Fig. 4.1**) rather than a single diode as the model assumes. Part of the fluorescence in the experimental spectrum is hypothesised to be due to fluorescence of the substrate located to the sides of the investigated diode and fluorescence of other (non-active) diodes on the chip being detected by the investigated diode. Currently, for simplicity, only the portion of the substrate directly below the operational diode is included in the model and the effects of the other diodes are not included at present, but these effects will be included in future versions of the model.

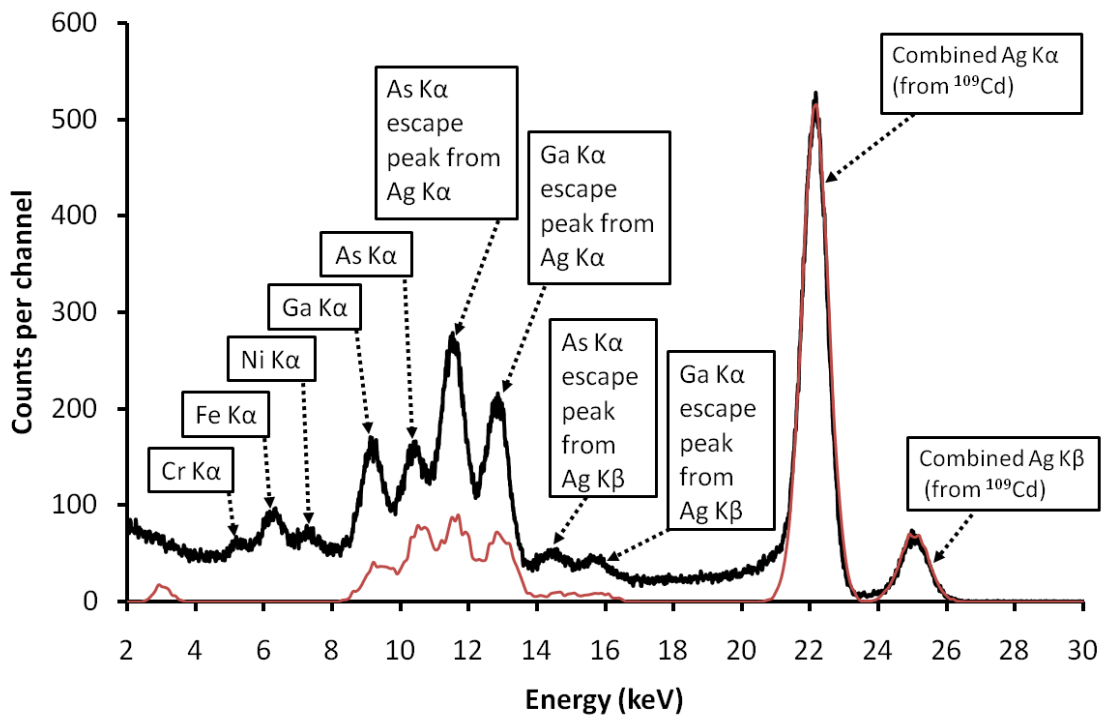


**Fig. 5.10.** Comparison of  $^{109}\text{Cd}$  spectra obtained experimentally with GaAs DI (black line) and simulated with the model (red line), see text.

Additionally, the larger than predicted escape peaks in the experimental spectrum suggest that the experimental detector may be collecting charge from photoelectrons created outside of the active region ( $i$  layer width +  $r_e$  of  $p^+$  layer) of the detector. For simplicity, it had been assumed in the model that the range of the photoelectrons was negligible i.e. they were considered to be localised to the atom from which they

originated. However, the actual range of photoelectrons at 10 keV in GaAs is  $\sim 0.42 \mu\text{m}$  (Everhart & Hoff, 1971). Photoelectrons that do reach the active region of the detector will contribute to the escape peaks, but their contribution is expected to be small and may not entirely explain the difference between the experimental and simulated spectra. The effect of non-localised photoelectrons, along with the effect of fluorescence from the substrate and other diodes will be explored and quantified in future modelling work. This may help achieve better agreement between the experimental and modelled spectrum in the region of the Ga and As fluorescence and escape peaks. Tailing on the low energy sides of the peaks is also visible in the experimental spectrum but not present in the simulated spectrum. This is consistent with the tailing being due to partial charge collection which is not presently included in the simple model, but will be included in future work.

## 5.7 Conclusions and discussion

Circular mesa GaAs  $p^+i-n^+$  diodes for photon counting X-ray spectroscopy have been fabricated and their performance characterised at temperatures from  $+80 \text{ }^\circ\text{C}$  to  $-30 \text{ }^\circ\text{C}$ . The performance of these diodes has been compared to  $\text{Al}_{0.8}\text{Ga}_{0.2}\text{As}$  devices of similar geometry using identical signal electronics (§4.3) and GaAs diodes previously reported at  $\leq 24 \text{ }^\circ\text{C}$  (Owens et al., 2001) (Owens et al., 2002a) (Erd et al., 2002).

The investigations reported in this chapter have extended the high temperature range at which GaAs diodes have been characterised beyond that previously reported and have shown that GaAs diodes can work as photon counting X-ray detectors at temperatures between  $+80 \text{ }^\circ\text{C}$  and  $-30 \text{ }^\circ\text{C}$  with modest spectral resolution (FWHM at 5.9 keV: 780 eV at  $0 \text{ }^\circ\text{C}$ , 1.55 keV at  $+80 \text{ }^\circ\text{C}$ ).

Examination of the noise contributions has shown that the spectral resolution (FWHM) at 5.9 keV of the detectors is primarily limited by dielectric noise, which is thought to arise primarily from the diode and JFET packaging, as was the case for the  $\text{Al}_{0.8}\text{Ga}_{0.2}\text{As}$  detectors (Chapter 4). The contribution from dielectric noise is significant; if it could be reduced to negligible levels, the data suggest that spectral resolutions (FWHM) at 5.9 keV of 480, 370 and 350 eV at 50, 20 and  $-10 \text{ }^\circ\text{C}$  respectively, may be possible (**Fig. 5.8**).

Higher energy X-ray spectra have been obtained experimentally using a  $^{109}\text{Cd}$  radioisotope X-ray source (providing Ag  $K\alpha_1 = 22.16$  keV, Ag  $K\alpha_2 = 21.99$  keV and Ag  $K\beta \approx 25$  keV X-ray emission lines). These spectra demonstrate that although the quantum efficiency is low at higher energies (0.034 at 22.16 keV) the diodes are still able to operate as photon counting spectroscopic devices at low count rates ( $\sim 0.3$  counts/sec for **Fig. 5.9**) without the signal being swamped by noise. The spectra also demonstrate the X-ray fluorescence of the diode itself which occurs when X-rays of energy greater than the binding energies of the Ga and As K shell electrons illuminate the detector. If the detector was to be used for X-ray fluorescence analysis of samples containing elements with emission lines between  $\sim 9$  keV and  $\sim 13.5$  keV (the region covered by the detector's Ga and As  $K\alpha$  and  $K\beta$  lines and associated escape peaks, assuming a  $^{109}\text{Cd}$  source was used to excite the sample), such as gold (Au  $L\alpha_1 = 9.713$  keV,  $L\alpha_2 = 9.628$  keV) or lead (Pb  $L\alpha_1 = 10.552$  keV,  $L\alpha_2 = 10.450$  keV), this internal fluorescence may obscure the fluorescence from the sample and would have to be subtracted from the spectra in order to reveal counts from emission lines in this region.

Simulated  $^{109}\text{Cd}$  radioisotope X-ray spectra have been produced using the Monte Carlo model detailed in Chapter 3. Good agreement between the model and experiment was achieved with regard to the positions and sizes of the Ag  $K\alpha$  and  $K\beta$  emission peaks from the X-ray source, and the positions of the fluorescence peaks (and associated escape peaks) from the GaAs detector itself. However, the sizes of the Ga and As fluorescence and escape peaks predicted by the model are smaller than those measured experimentally. This is possibly a result of the model not currently including fluorescence of the non-active diodes and substrate located to the sides of the investigated diode, and assuming that all photoelectrons generated in the non-active portions of the detector are reabsorbed before reaching the diode's active region. These assumptions, which were included for simplicity in the present model, will be re-examined, their effects quantified and the simulations extended to include the phenomena they represent, in future versions of the model.

Whilst the currently achieved spectral resolutions are modest, the new measurements reported here hint that further development of GaAs X-ray  $p^+ - i - n^+$  photodiodes will lead to devices that can operate in spectroscopic photon counting mode at temperatures ( $> 50$  °C) where silicon detectors cannot operate without cooling.

# Chapter 6 Photon counting $\text{Al}_{0.8}\text{Ga}_{0.2}\text{As}$ avalanche photodiodes

## 6.1 Introduction

Room temperature  $\text{Al}_x\text{Ga}_{1-x}\text{As}$  avalanche photodiodes (APDs), which use impact ionisation (see §2.7) to multiply the charge created when a photon is absorbed in the device to increase the signal to noise ratio achieved, have been of interest to researchers investigating devices suitable for telecommunications for some years. Particular research emphasis has been placed on understanding  $\text{Al}_x\text{Ga}_{1-x}\text{As}$ 's impact ionisation properties (Ng et al., 2001, 2002) (Plimmer et al., 2000) (Tan et al., 2001) in order to exploit the charge multiplication effect fully. However, those devices have always been operated in current mode, rather than photon counting mode, and not at X-ray energies. Silicon X-ray photon counting APDs have been reported in the literature, and commercial reach-through devices (see §2.7.1) are available which can achieve a spectral resolution at 5.9 keV of 380 eV FWHM at  $-20^\circ\text{C}$  with an electron avalanche multiplication factor of 14, and that have a 130  $\mu\text{m}$  thick absorption layer giving a quantum efficiency of  $\sim 0.99$  at 5.9 keV (Yatsu et al., 2006) (Kataoka et al., 2005).

Prior to the work reported in this thesis, there had been some limited reports of X-ray detection with  $\text{Al}_x\text{Ga}_{1-x}\text{As}$  avalanche devices, both photon counting (Lauter et al., 1995, 1996) (Lees et al., 2008) and not photon counting (Silenas et al., 2002, 2003) (Dapkus et al., 2007). Of the two X-ray photon counting  $\text{Al}_x\text{Ga}_{1-x}\text{As}$  APDs reported in the literature, Lees et al.'s detector was an  $\text{Al}_{0.8}\text{Ga}_{0.2}\text{As}$   $\text{p}^+\text{-p}^-\text{-n}^+$  diode (**Table 6.1**) and Lauter et al.'s detector was a separate absorption and multiplication region (SAM) diode which had a 4.5  $\mu\text{m}$  GaAs absorber region with 12 very thin (0.045  $\mu\text{m}$ )  $x$ -graded ( $x = 0.01$  to  $x = 0.45$ )  $\text{Al}_x\text{Ga}_{1-x}\text{As}$  multiplication regions beneath it. Lauter et al.'s detector was reported to have spectral resolutions (FWHM) at 13.96 keV and 17.8 keV of 0.95 keV and 1.4 keV, respectively, when operated at room temperature.

Lees et al.'s device was reported as having a spectral resolution (FWHM) at 5.9 keV of 1.5 keV in non-avalanche mode which improved to 1.2 keV in avalanche mode

(reverse bias = 26 V) at room temperature. However, when the detector was operated in avalanche mode, an additional peak was reported to appear in the spectrum. The additional peak was observed by Lees et al. to separate from the expected Mn  $K\alpha$  &  $K\beta$  peak (produced by the  $^{55}\text{Fe}$  radioisotope source used to illuminate the device) with increasing reverse bias and avalanche multiplication factor (Lees et al., 2008).

Layer	Material	Thickness ( $\mu\text{m}$ )	Dopant	Type	Doping Density ( $\times 10^{18} \text{ cm}^{-3}$ )
1	GaAs	0.01	Be	$p^+$	2
2	$\text{Al}_{0.8}\text{Ga}_{0.2}\text{As}$	0.92	Be	$p^+$	0.4
3	$\text{Al}_{0.8}\text{Ga}_{0.2}\text{As}$	0.58	Undoped	$p^-$	0.05
4	$\text{Al}_{0.8}\text{Ga}_{0.2}\text{As}$	1.0	Si	$n^+$	2
5	GaAs	0.25	Si	$n^+$	2
Substrate	$n^+$ GaAs				

**Table 6.1.** Layer details of the  $\text{Al}_{0.8}\text{Ga}_{0.2}\text{As } p^+ - p^- - n^+$  wafer (Lees et al., 2008).

This chapter presents results both experimental and from the Monte Carlo model described in Chapter 3. The additional peak observed by Lees et al. is shown by these results to be a consequence of the unequal distributions of multiplications undergone by charge carriers created by photons absorbed in the  $p^+$  and  $p^-$  layers of the device. The effects of this phenomenon on future  $\text{Al}_x\text{Ga}_{1-x}\text{As}$  X-ray photon counting avalanche photodiode designs are discussed.

The additional peak effect was then exploited through further experimental and modelling results to derive the temperature dependence of  $\text{Al}_{0.8}\text{Ga}_{0.2}\text{As}$ 's electron and hole ionisation coefficients which had not previously been reported.

## 6.2 Diode fabrication, design and selection

The diodes used in this chapter were the same diodes used by Lees et al. (2008). They are circular mesa diodes fabricated by photolithography from wafers grown on a GaAs  $n^+$  substrate by molecular beam epitaxy at the National Centre for III-V Technologies, University of Sheffield, UK. An optical microscope photograph (**Fig. 4.3**) of a chip of the wafer shows the diode layout; 25, 50, 100 and 200  $\mu\text{m}$  radii devices can be seen in this figure, but only the 100  $\mu\text{m}$  radii devices were used in this work. The 100 and

200  $\mu\text{m}$  radii diodes have quasi-annular contacts as per the devices reported in Chapters 4 and 5. A table showing the wafer's layer properties is shown in **Table 6.1**.

## 6.3 Initial computer simulations

### 6.3.1 X-ray source definition

The Monte Carlo model described in Chapter 3 was used to simulate an  $\text{Al}_{0.8}\text{Ga}_{0.2}\text{As}$  avalanche photodiode illuminated with an  $^{55}\text{Fe}$  radioisotope source. For the simulations discussed in this chapter, the source defined in the model was configured to emit  $10^6$  photons per simulation with an energy of 5.9 keV and  $1.38 \times 10^5$  photons with an energy of 6.5 keV, representing the Mn  $K\alpha$  and Mn  $K\beta$  emission lines of  $^{55}\text{Fe}$  in the ratio measured by Schötzig (2000). All emissions from the source were normal to the  $y$ - $z$  surface of the diode (**Fig. 3.3**).

### 6.3.2 Detector properties definition

For simplicity, the detector was defined in the model to consist of a  $0.92 \mu\text{m}$   $\text{p}^+$  layer, a  $0.58 \mu\text{m}$   $\text{p}^-$  layer and a  $1.0 \mu\text{m}$   $\text{n}^+$  layer as shown in **Fig. 6.1**. The Fano factor,  $F$ , was assumed to be 0.14 and the electron-hole pair creation energy,  $\omega_{EHP} = 5.25 \text{ eV}$ . The electron recombination length,  $r_e$ , in the  $\text{p}^+$  layer was estimated to be  $0.16 \mu\text{m}$ . Hole recombination in the  $\text{n}^+$  layer was assumed to occur before the holes could travel a significant distance. The electron and hole recombination lengths in the  $\text{p}^-$  layer were assumed to be long enough to enable complete collection of the charge generated in this layer (see §3.4). The electron,  $\alpha$ , and hole,  $\beta$ , ionisation coefficients were calculated in the model from the parameterised functions reported by Ng et al. (2001), see **Fig. 6.2**. Following Tan et al. (2011), the noise contribution to the final spectrum from the variation in the multiplication factor between sibling electron-hole pairs was assumed to be insignificant compared with the other sources of noise contributing to the broadening of the spectral peaks (§2.7.4).

### 6.3.3 Initial simulation results

Initial simulations at  $1/E = 2.15 \times 10^{-6} \text{ cm/V}$  (reverse bias = 27 V) predicted that no significant avalanche multiplication would occur at this reverse bias because the field produced in a uniformly doped  $\text{p}^-$  layer (thickness =  $0.58 \mu\text{m}$ ) would be too small. Simulations using higher electric fields showed that at  $1/E = 1.796 \times 10^{-6} \text{ cm/V}$  (reverse

bias = 32.3 V), the electron multiplication factor,  $M_e$ , (Eq. 2.25) equalled 6.00 and the mean mixed carrier multiplication factor (Eq. 2.24) in the  $p^-$  layer,  $M_{mix}$ , equalled 4.64. A graph showing the electron, hole and mean mixed multiplication factors predicted by the model from Ng et al.'s parameterised ionisation coefficients is given in **Fig. 6.3**.

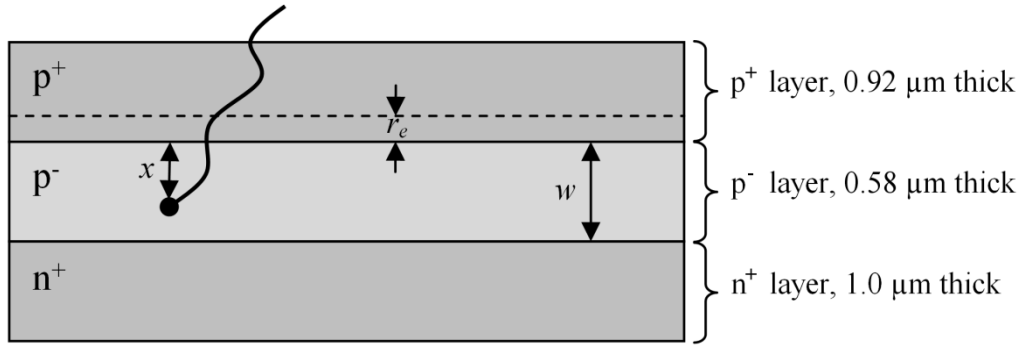


**Fig. 6.1.** A schematic cross-sectional diagram of the modelled diode. The depth,  $x$ , of the photon interaction in the  $p^-$  layer is shown, along with the thickness,  $w$ , of the  $p^-$  layer ( $0.58 \mu\text{m}$ ) and electron recombination length,  $r_e$ . The thicknesses of the  $p^+$  ( $0.92 \mu\text{m}$ ) and  $n^+$  ( $1.0 \mu\text{m}$ ) layers are also indicated.

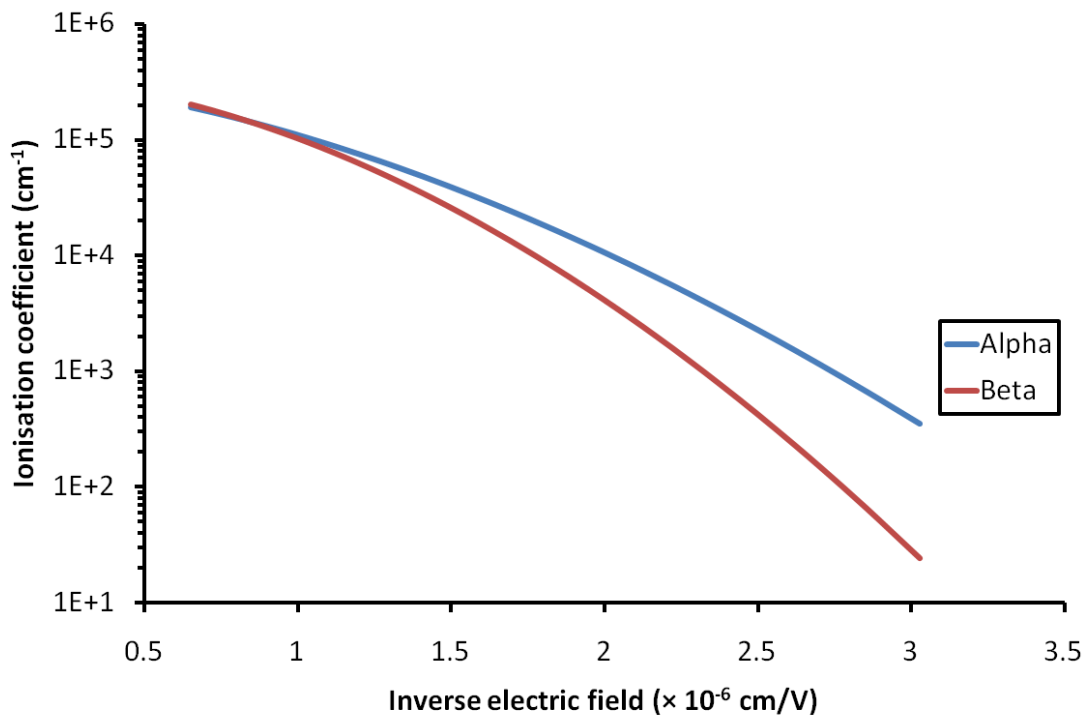


**Fig. 6.2.** Plots of the functions describing the electron ( $\alpha$ , blue line) and hole ( $\beta$ , red line) ionisation coefficients of  $\text{Al}_{0.8}\text{Ga}_{0.2}\text{As}$  (Ng et al., 2001).

The simulations showed that when the diode is in avalanche mode, the variation of the multiplication factor (§2.7.3) as a function of photon absorption depth (§3.3) in the  $p^-$

layer would lead to a significant variation in the post-avalanche charge read out from each event in this layer. The simulations predicted that this would result in events from the  $p^-$  layer forming a broad spectral peak in the spectrum.

However, electrons created by photons absorbed in the  $p^+$  layer within one recombination length of the  $p^+ - p^-$  boundary, would all receive the same multiplication since they all must pass through the whole of the  $p^-$  layer to be read out. Therefore events from photons absorbed in the  $p^+$  layer would be tightly clustered (with only the system noise (Eq. 2.31) and not any position dependence (Eq. 2.24) causing Gaussian spreading of their values).

A simulated spectrum from both layers showing the combination of the broad peak from the  $p^-$  layer and the tightly clustered peak from the  $p^+$  layer is shown in **Fig. 6.4**. A system noise (Eq. 2.31) (inc. parallel white (§2.6.3), series white (§2.6.4),  $1/f$  (§2.6.5), dielectric (§2.6.6), induced gate current (§2.6.7), Fano (Eq. 2.6) and excess (Eq. 2.30) noise contributions) = 105  $e^-$  r.m.s. ENC, equivalent to 1.3 keV FWHM at 5.9 keV (derived from comparable experimental spectra) is included.

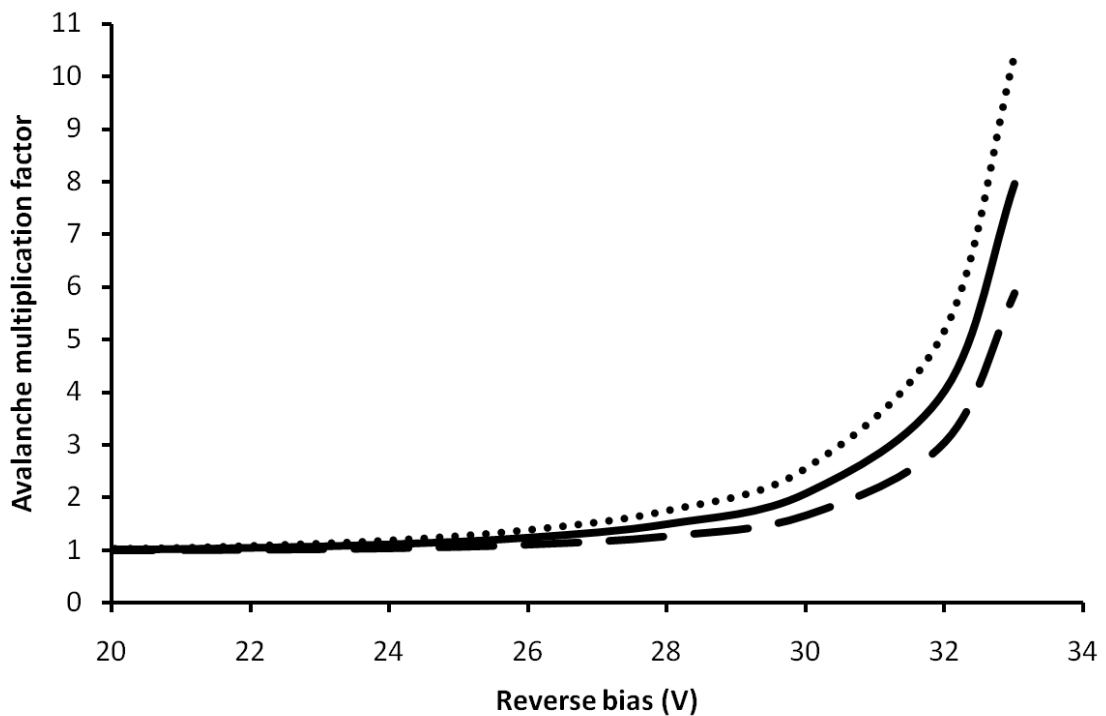


**Fig. 6.3.** Multiplications predicted by the simulation:  $M_e$  (dots),  $M_{mix}$   $p^-$  layer mean (solid line) and  $M_h$  (dashes).

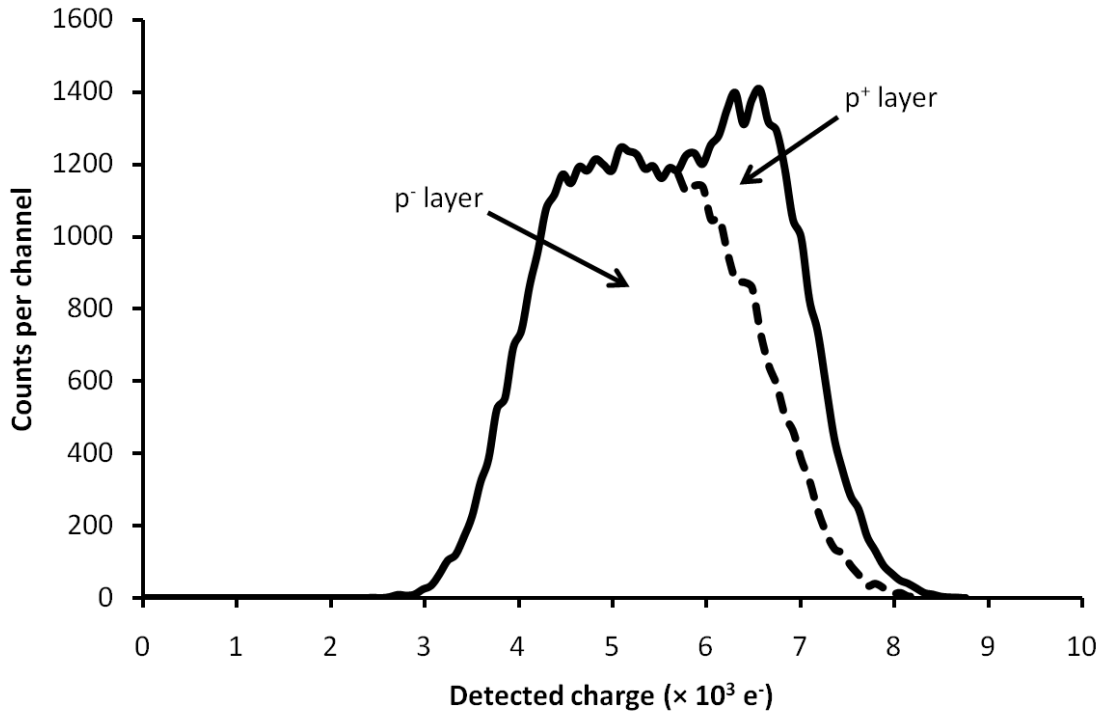


**Fig. 6.4.** Predicted spectrum from multiplications of  $M_e = 6.00$  and  $M_{mix} = 4.64$  ( $1/E = 1.796 \times 10^{-6}$  cm/V, reverse bias = 32.3 V). The dashed line shows the predicted shape of the spectrum without the  $p^+$  layer's contribution.

#### 6.4 Experimentally observed spectra

Experimental  $^{55}\text{Fe}$  X-ray spectra to compare with the simulation results were produced as per §4.5 and Lees et al. (2008). The diode was reverse biased at 24, 26 and 27 V in avalanche mode and at 10 V in non-avalanche mode. The diode, pre-amplifier, shaping amplifier (shaping time = 3  $\mu\text{s}$ ), multi-channel analyser (MCA) and power supplies were all kept at 20 °C.

The avalanche multiplication factors were calculated from the position of the additional and main peaks assuming Gaussian peak shapes for each main and additional peak (see **Figs. 6.5 & 6.7**). As per Lees et al. (2008), the experimental X-ray spectra showed significant avalanche multiplication (e.g.  $M_e = 3.47$ ,  $M_{mix} = 2.74$  at 24 V). The additional peak emerged when the diode was operated in avalanche mode. The gain of the main and additional peaks increased with reverse bias and the additional peak separated from the main peak (**Fig. 6.5**). The unity avalanche gain ( $M_e = M_h = M_{mix} = 1$ ) characteristics derived from the non-avalanche mode spectra taken at a reverse bias of 10 V were used to deduce the avalanche gains of the main and additional peaks (**Fig. 6.6**). As per Lees et al. (2008), the FWHM improved when the diode was

operated in avalanche mode (best FWHM = 1.21 keV at 5.9 keV, achieved at reverse bias = 24 V) compared with non-avalanche mode (reverse bias = 10 V, FWHM = 2.39 keV at 5.9 keV), see **Fig. 6.5**. However, as the reverse bias was increased above the optimum (24 V), the FWHM became poorer but still remained better than in non-avalanche mode. This degradation of the FWHM at high reverse biases (> 24 V) is hypothesised to be primarily a consequence of the leakage current and parallel white noise (§2.6.3) increasing rapidly as the diode approaches its breakdown voltage ( $\approx 29$  V).

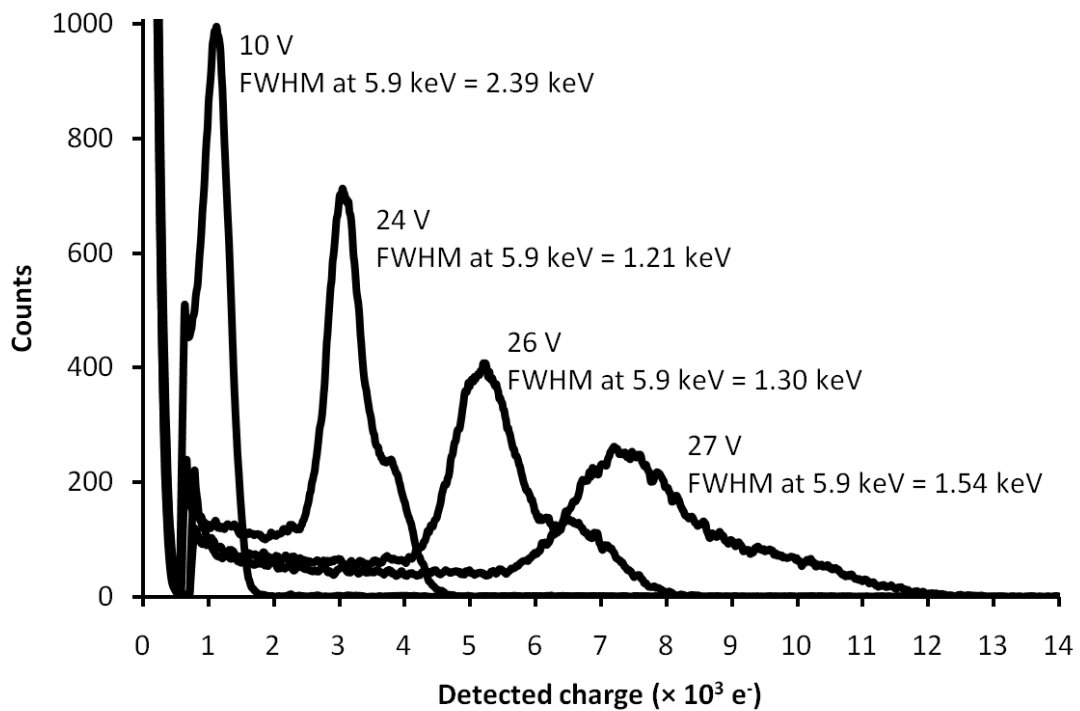


**Fig. 6.5.** Experimentally obtained  $^{55}\text{Fe}$  spectra at 10, 24, 26 and 27 V.

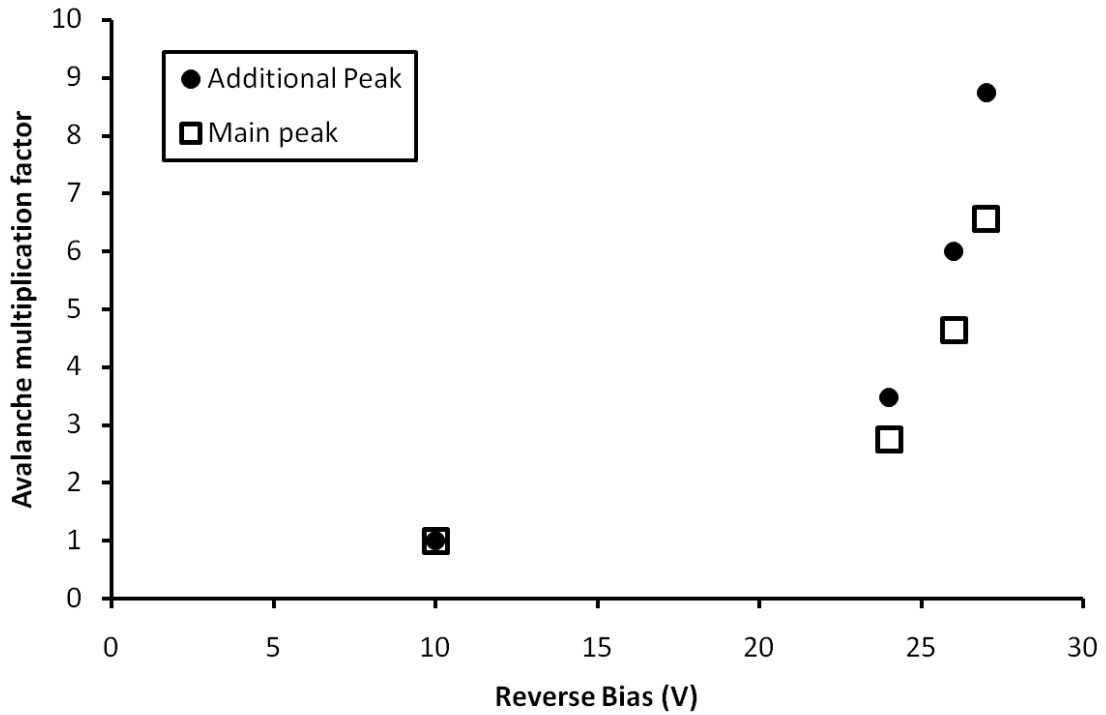


**Fig. 6.6.** Experimentally measured reverse bias dependence of the avalanche multiplication factor of the additional (filled circles) and main (open squares) peaks.

## 6.5 Interpretation of experimental results and model adaptation

The onset of avalanche multiplication in the experimentally investigated diode occurs at lower reverse bias ( $> 10$  V) than predicted from the model ( $> 22$  V). The reverse bias necessary to achieve a specific multiplication is larger in the model than required with the experimental diode (**Table 6.2**). In the experimental spectra, even with the diode operated in avalanche mode, both the main and additional peaks appeared Gaussian (see **Fig. 6.5** for the experimental spectra and **Fig 6.7** for an example spectrum with the fitted Gaussians shown) with no indication of the main peak being broadened by the position dependence of the multiplication (Eq. 2.24), as would be expected from the simulated spectra (**Fig. 6.4**).

Discussions with Dr J.S. Ng, Department of Electrical and Electronic Engineering, University of Sheffield, who supplied the diodes, indicated that the doping within the  $p^-$  layer of the devices may be non-uniform (Ng, 2009). This doping non-uniformity is postulated to allow higher fields to be achieved within the  $p^-$  region for a given reverse bias than would be expected in a diode with uniform doping. This leads to the onset of avalanche multiplication at lower reverse bias than the simulations predict and modifies the position dependence of the multiplication factor in the  $p^-$  layer. Consequently, with

the assumption that the ionisation coefficients (Ng et al., 2001) were correct, the simple model for an ideal p-i-n diode (§6.3.3) was extended to account for the doping non-uniformity.

The electric field required to match the multiplications seen experimentally (**Fig. 6.6**) was used in the model, see **Table 6.2**. The position variance (Eq. 2.24) of the multiplication factor in the p<sup>-</sup> layer was restricted by applying the mean multiplication to all charge carriers from the p<sup>-</sup> layer. The mean multiplication was calculated from the multiplications predicted by the model (using Eqs. 2.24 and 3.6a-b) for each individual charge carrier.

$M_e$	$M_{mix}$	Experimental reverse bias (V)	Equivalent simulated reverse bias (V)	Simulated inverse electric field ( $\times 10^{-6}$ cm/V)
3.47	2.74	24	31.1	1.865
6.00	4.64	26	32.3	1.796
8.74	6.56	27	32.8	1.770

**Table 6.2.** Reverse biases required to achieve specific multiplications in the experimentally measured diode and the simulated diode (see §6.3.3 and §6.5).

## 6.6 Adapted model results

The simple modifications to the model produced simulated spectra that are in good agreement with the experimentally obtained spectra (see **Fig. 6.7**, and compare **Fig. 6.8** with **Fig. 6.5**). The tail on the left of the experimental spectrum (**Fig. 6.7**) is due to partial charge collection in the device (for simplicity, this is not included in the model at present). For comparison, the simulated spectra were normalised in counts to the experimental spectra by normalising to the height of the main peak.

**Fig. 6.8** shows how, as the avalanche gain increases, the additional peak separates from the main peak in agreement with the separation that is observed in the experimental spectra (**Fig. 6.5**). The increasing separation of the main and additional peaks in the simulations is a result of increasing electric field (reverse bias) across the high field region.

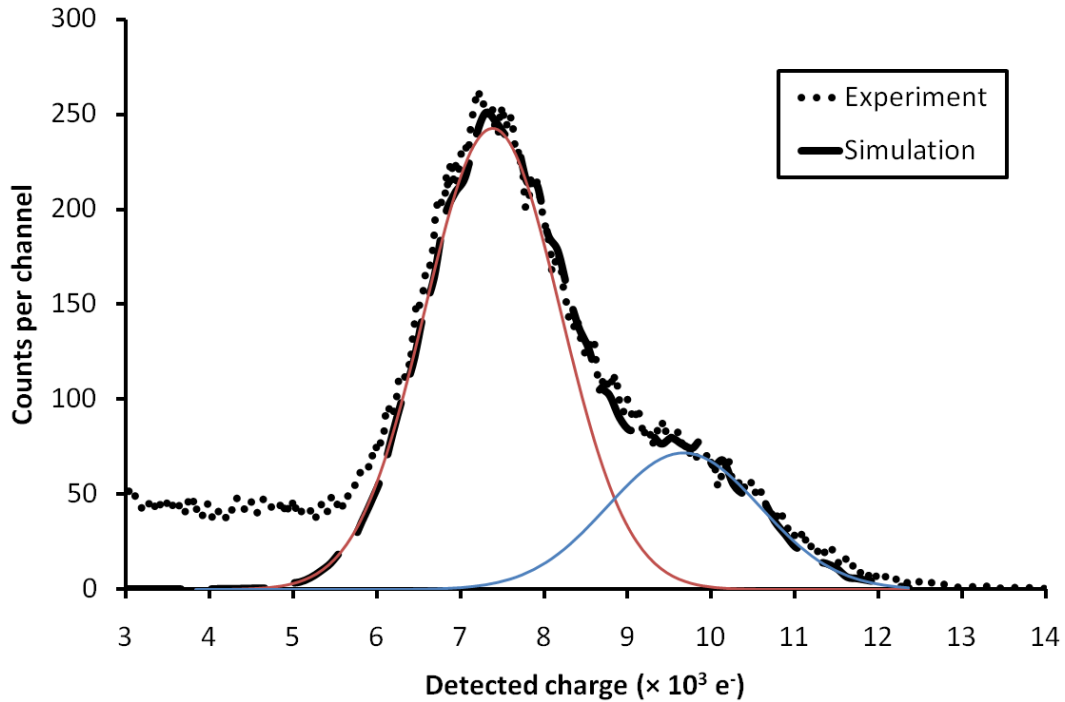


**Fig. 6.7.** Comparison between the experimentally obtained  $^{55}\text{Fe}$  spectrum (dotted line) and simulated  $^{55}\text{Fe}$  spectrum (dashed line) at  $M_e = 8.74$ ,  $M_{\text{mix}} = 6.56$  (Table 6.2). Two Gaussian peaks are shown which have been fitted to the experimental data representing the peaks from the  $p^-$  (red line) and  $p^+$  (blue line) layers (FWHM at 5.9 keV = 1.5 keV).

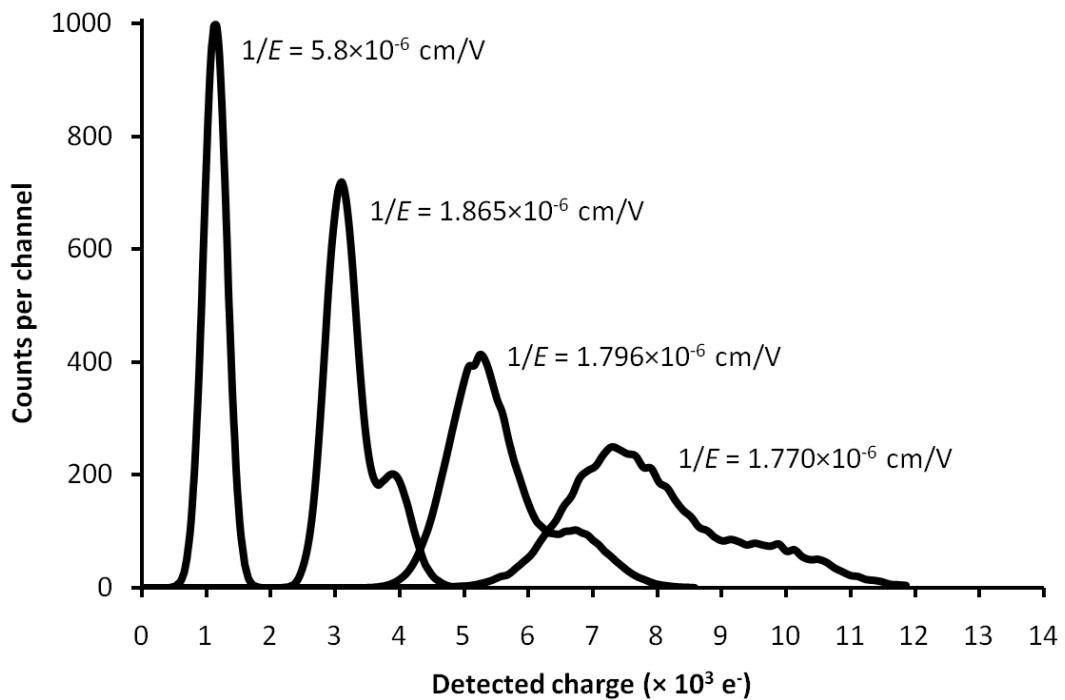


**Fig. 6.8.** Simulated  $^{55}\text{Fe}$  spectra at inverse electric fields of  $5.8 \times 10^{-6}$ ,  $1.865 \times 10^{-6}$ ,  $1.796 \times 10^{-6}$  and  $1.770 \times 10^{-6}$  cm/V (Table 6.2). Compare with the experimental spectra in Fig. 6.5.

## 6.7 Reduced $p^+$ layer thickness simulations

For many applications, such as X-ray fluorescence spectroscopy (XRF) of planetary surfaces, the low energy X-ray performance of the device is critical (Fraser, 2008). Three major rock forming elements (Mg, Al and Si) have  $K\alpha$  lines below 2 keV (**Table 6.3**). Sensitivity to X-rays at energies 0.4 – 1 keV makes the O  $K\alpha_1$  line (0.525 keV) detectable and allows the investigation of L shell emission from elements such as Ti (0.45 keV) and Fe (0.705 keV). Since the attenuation coefficients at these energies are high, it is essential to minimise the thickness of the  $p^+$  layer to ensure the photons interact in the active region of the device. The relatively simple modification to the existing design of reducing the thickness of the  $p^+$  layer to  $r_e$  will ensure all photons absorbed in the  $p^+$  layer are counted. Relative device efficiencies at reduced  $p^+$  layer thicknesses were calculated from Eq. 2.1 and are shown in **Fig. 6.9**.

Element	$K\alpha$ (keV)	$L\alpha$ (keV)
O	0.525	-
Mg	1.25	-
Al	1.49	-
Si	1.74	-
Ti	4.5	0.45
Fe	6.4	0.705

**Table 6.3.** Important low energy X-ray emission lines.

Reducing the thickness of the  $p^+$  layer is also necessary to minimize the degradation of the spectrum caused by the additional peak. To show this effect, the simulations were repeated with the thickness of the  $p^+$  layer reduced to 0.08  $\mu\text{m}$  (half the recombination length in the  $p^+$  layer) as well as 0.04 and 0.01  $\mu\text{m}$ . In the spectra resulting from these simulations, the number of counts in the additional peak is reduced (**Fig. 6.10**). The additional peak is reduced in size because thinning the  $p^+$  layer to less than one recombination length reduces the number of electrons generated in the  $p^+$  layer that can contribute to the spectrum.

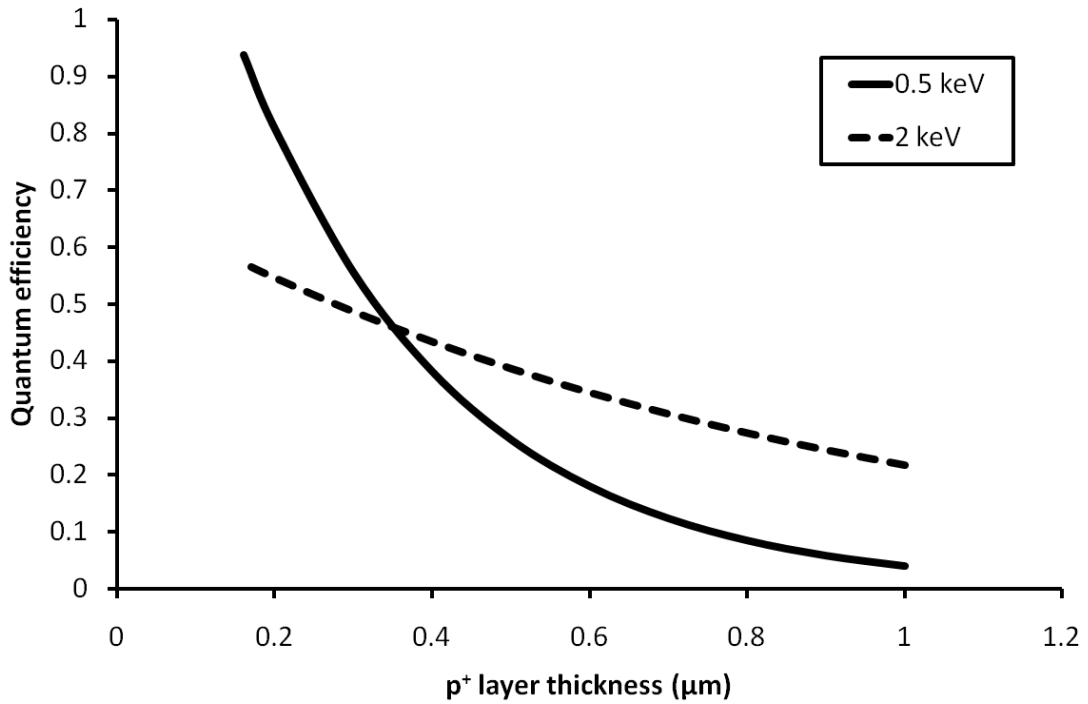


**Fig. 6.9.** Effect of  $p^+$  layer thickness on quantum efficiency of the device ( $p^-$  layer thickness =  $0.58 \mu\text{m}$ ) at  $0.5 \text{ keV}$  (solid line) and  $2 \text{ keV}$  (dashed line) with varying  $p^+$  layer thickness.

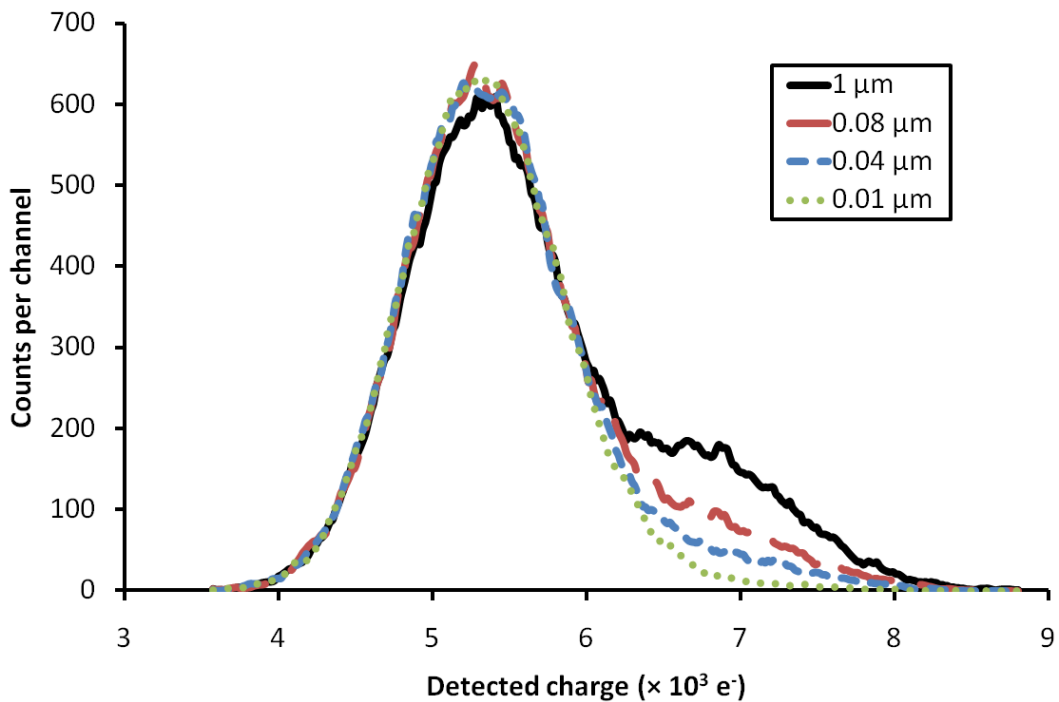


**Fig. 6.10.** Simulations of  $^{55}\text{Fe}$  spectra with  $p^+$  layer thickness of  $1 \mu\text{m}$  (solid black line) (Table 6.1),  $0.08 \mu\text{m}$  (long red dashes),  $0.04 \mu\text{m}$  (short blue dashes) and  $0.01 \mu\text{m}$  (olive dots). For clarity, only simulations for  $1/E = 1.796 \times 10^{-6} \text{ cm/V}$  ( $M_e = 6.00$ ,  $M_{\text{mix}} = 4.64$ ) are shown.

## 6.8 Temperature dependence of the impact ionisation coefficients in $\text{Al}_{0.8}\text{Ga}_{0.2}\text{As}$

The electric field dependence of the electron and hole impact ionisation coefficients had previously been reported for  $\text{Al}_x\text{Ga}_{1-x}\text{As}$  with  $x = 0.15, 0.3, 0.6$  (Plimmer et al., 2000),  $x = 0.2, 0.4$  (Zheng et al., 2000) and  $x = 0.8$  (Ng et al., 2000, 2001). However, the temperature dependence of the impact ionisation coefficients had only been reported for  $x = 0.2, 0.4$  (Zheng et al., 2000) and  $x = 0.6$  (Harrison et al., 2002). Knowing how the ionisation coefficients vary with temperature is essential to understanding how APDs operate at high, and varied, temperature.

### 6.8.1 Experimental measurements

To obtain the measurements necessary to determine the temperature dependence of the ionisation coefficients in  $\text{Al}_{0.8}\text{Ga}_{0.2}\text{As}$ , the diode was housed with, and connected to, a Si charge sensitive preamplifier with a Si JFET (Vishay Siliconix 2N4416) front end transistor, as per §6.4 and Chapter 4. The APD, Si JFET and preamplifier electronics were all placed inside a Design Environmental FS55-65 temperature test chamber (TTC) (Design Environmental, N.D.) and subject to temperature control. The temperature of the APD, Si JFET and preamplifier was monitored by thermocouple (positioned adjacent to the diode) to ensure temperature equalisation between APD environment and TTC environments. The temperature dependent performance of the system was investigated from  $+80\text{ }^\circ\text{C}$  to  $-20\text{ }^\circ\text{C}$ . The preamplifier was connected to an EG&G Ortec® 571 shaping amplifier (EG&G Ortec, N.D.) (shaping time =  $3\text{ }\mu\text{s}$ ) located outside of the TTC. The shaping amplifier was connected to an Ortec MCA (Advanced Measurement Technology, Inc., 2008). The diode was reverse biased and the preamplifier powered by externally located power supplies.

A  $10\text{ MBq }^{55}\text{Fe}$  radioisotope X-ray source was positioned 3 mm above the diode. Spectra were taken from high temperature to low temperature in  $10\text{ }^\circ\text{C}$  steps. The system was allowed to stabilise at each temperature before spectrum accumulation was started and multiple spectra were accumulated at each temperature. Spectra were accumulated at each temperature with the diode reverse biased at 26 V (avalanche mode) and 10 V (non-avalanche mode) to obtain unity avalanche gain spectra to enable calculation of multiplication factors as per §6.4.

For each avalanche mode spectrum, the position of the additional peak and main peak relative to the spectrum's zero energy noise peak were recorded. The positions of the main and additional peaks were determined by fitting Gaussians to the data in the software package MicroCal Origin®. The non-avalanche peak's position relative to the zero energy noise peak's position was recorded for each non-avalanche spectrum to give the system's gain calibration in non-avalanche mode. The positions of the main and additional peaks in the avalanche mode spectra were divided by the position of the non-avalanche mode peak to determine  $M_{mix}$  and  $M_e$  at each temperature. The measured  $M_{mix}$  and  $M_e$  can be seen in **Fig. 6.11**.

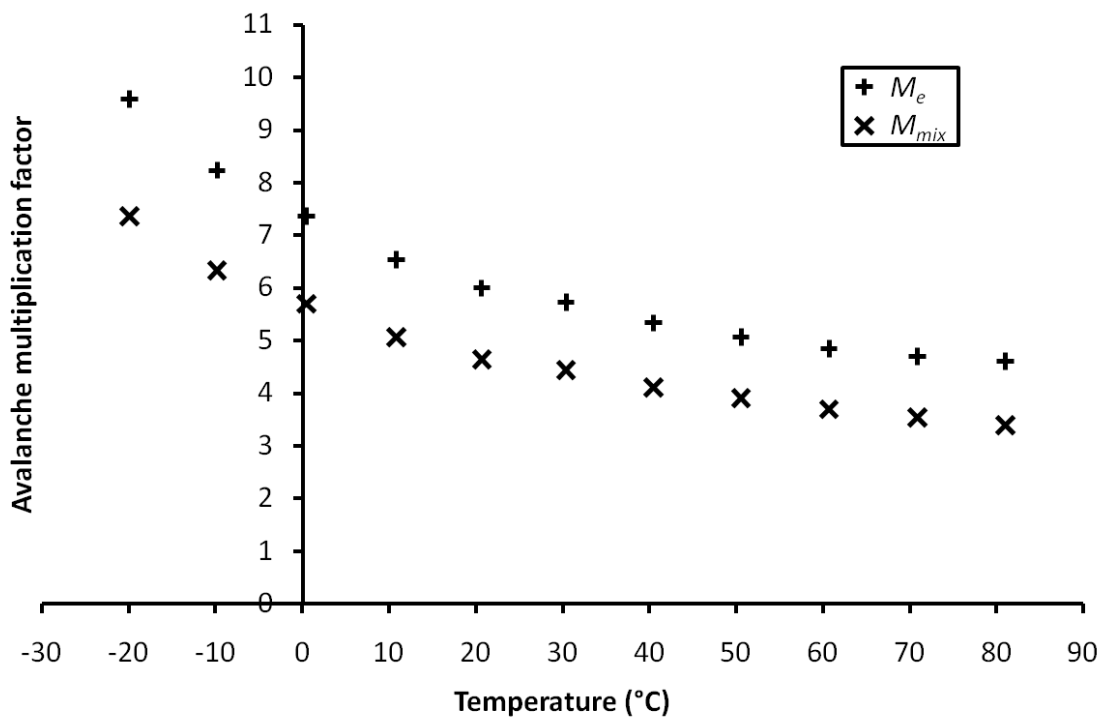


**Fig. 6.11.** The experimentally measured temperature dependence of  $M_{mix}$  (x symbols) and  $M_e$  (+ symbols) at 26 V.

### 6.8.2 Computer modelling and the determination of $\alpha$ and $\beta$

The computer model (Chapter 3) with the simple modifications described in §6.5 was used with the electric field and multiplication dependent ionisation coefficients from Ng et al. (2001) to determine the ionisation coefficients required to produce the  $M_{mix}$  and  $M_e$  that were experimentally observed at each temperature. As previously reported for room temperature, since the doping in the p<sup>-</sup> layer of the investigated diodes was non-uniform, an electric field greater than would be expected in a uniformly doped p<sup>-</sup> layer was produced within the diode. The inverse electric field expected in a uniformly

doped  $p^-$  layer of width, ( $w = 0.58 \mu\text{m}$ ), at a reverse bias of 26 V was  $2.23 \times 10^{-5} \text{ cm/V}$ ; however the inverse electric field implied by the experimentally observed multiplication factors  $M_e$  and  $M_{mix}$  was  $1.796 \times 10^{-6} \text{ cm/V}$ . To correct for the doping non-uniformity in the  $p^-$  layer, the same approach was taken and the inverse electric field observed to be present in the device (i.e.  $1/E = 1.796 \times 10^{-6} \text{ cm/V}$ ) was used.

For each temperature, the computer model was used to determine the inverse electric field at which the ionisation coefficients produced the  $M_e$  and  $M_{mix}$  experimentally observed. Simulated and experimental  $M_e$  and  $M_{mix}$  matched extremely well ( $\pm \leq 5\%$  over the full range). Having determined the corresponding ionisation coefficients for each temperature in this manner,  $M_h$  was computed for each temperature.

The temperature dependence of the measured  $M_e$  and  $M_{mix}$ , together with the simulated  $M_e$ ,  $M_{mix}$  and  $M_h$  are shown in **Fig. 6.12**. The temperature dependence of the electron,  $\alpha$ , and hole,  $\beta$ , ionisation coefficients corresponding to these multiplications are shown in **Fig. 6.13**. The inverse electric field for the data presented in **Fig. 6.12** and **Fig. 6.13** is  $1.796 \times 10^{-6} \text{ cm/V}$ .

The temperature dependence of the  $k$ -ratio ( $= \beta/\alpha$ ) is shown in **Fig. 6.14** along with  $k$ -ratio data for  $\text{Al}_x\text{Ga}_{1-x}\text{As}$   $x = 0, 0.2$  and  $0.4$  (Zheng et al., 2000). However, it should be noted that Zheng et al.'s data were measured at different electric field strengths and are only shown for interest.

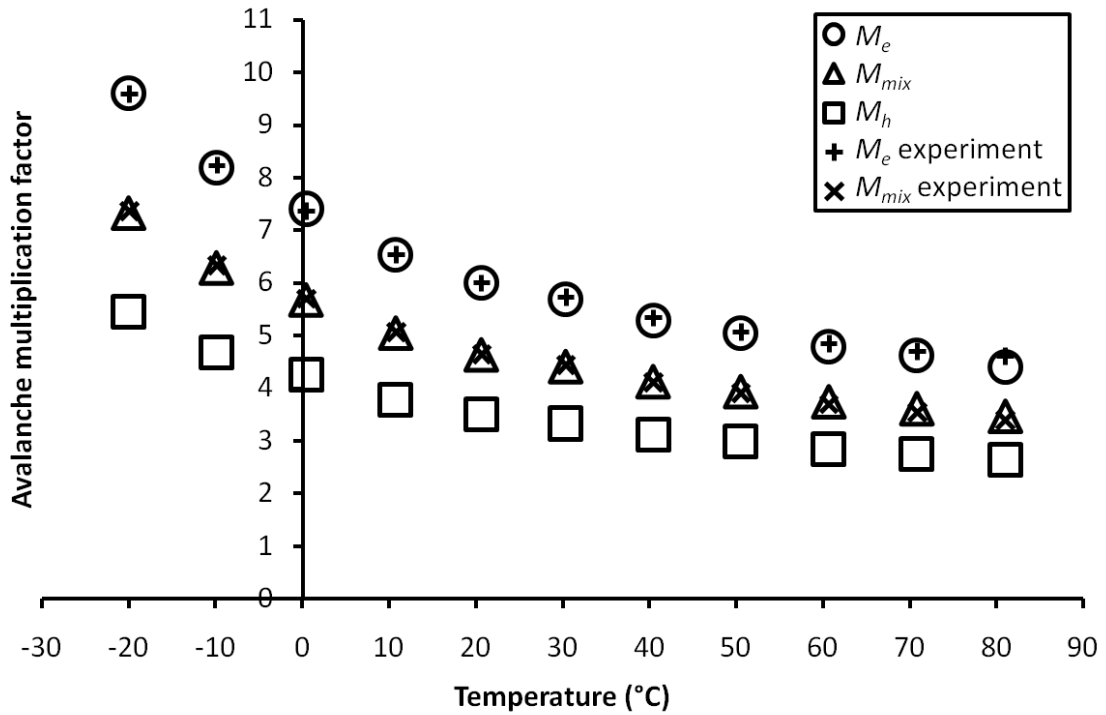


**Fig. 6.12.** The temperature dependence of the multiplication factors. Experimentally measured:  $M_e$  (+ symbol),  $M_{mix}$  (× symbol). Simulated:  $M_e$  (open circles),  $M_{mix}$  (open triangles),  $M_h$  (open squares). All data at  $1/E = 1.796 \times 10^{-6} \text{ cm/V}$ .

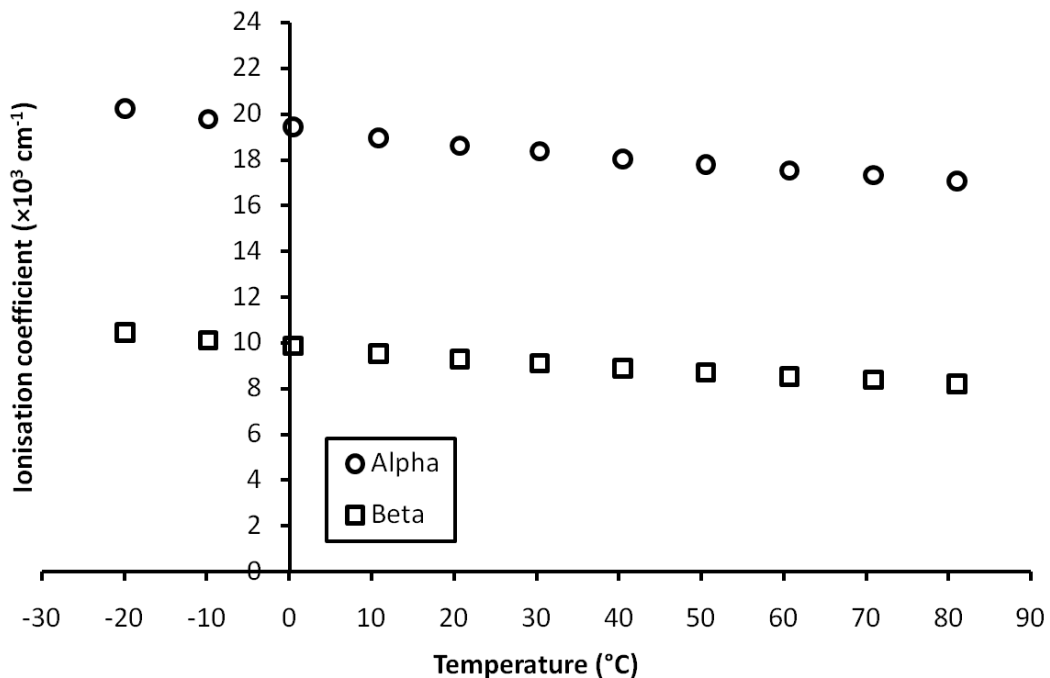


**Fig. 6.13.** The determined temperature dependence of the electron ionisation coefficient,  $\alpha$ , (open circles) and hole ionisation coefficient,  $\beta$ , (open squares) at  $1/E = 1.796 \times 10^{-6} \text{ cm/V}$ .

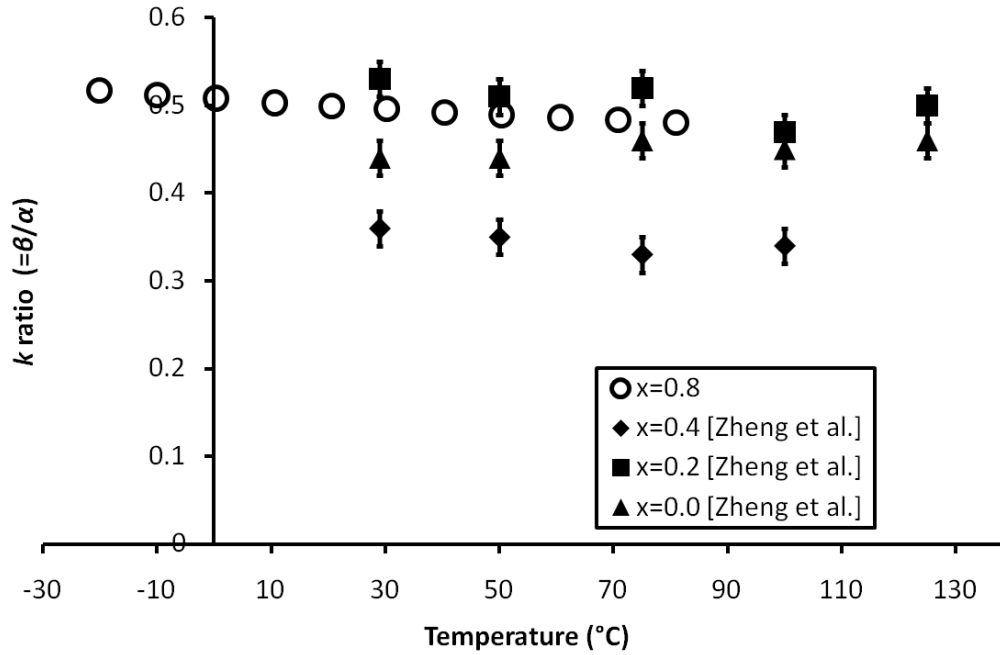


**Fig. 6.14.** The temperature dependence of the determined  $Al_{0.8}Ga_{0.2}As$   $k$ -ratio ( $= \beta/\alpha$ ) at  $1/E = 1.796 \times 10^{-6} \text{ cm/V}$  (open circles). Also plotted are the  $k$ -ratios for  $GaAs$  at  $1/E = 2.8 \times 10^{-6} \text{ cm/V}$  (filled triangles),  $Al_{0.2}Ga_{0.8}As$  at  $1/E = 2.402 \times 10^{-6} \text{ cm/V}$  (filled squares), and  $Al_{0.4}Ga_{0.6}As$  at  $1/E = 2.04 \times 10^{-6} \text{ cm/V}$  (filled diamonds) (Zheng et al., 2000).

## 6.9 Conclusions and discussion

The additional peak observed here and by Lees et al. (2008), is formed by electrons generated in the  $p^+$  layer within one recombination length of the  $p^+-p^-$  boundary, and is predicted by the model described in Chapter 3 with the simple modifications described in §6.5. The avalanche multiplication received by electrons generated in the  $p^+$  layer is equal to the maximum electron-initiated avalanche multiplication achievable at the applied electric field. The charge carriers forming the additional peak receive the maximum electron-initiated avalanche multiplication because they pass through the whole of the  $p^-$  layer before being collected. The additional peak separates from the main peak (which has avalanche gain equal to  $M_{mix}$ ) with increasing applied electric field because the ionisation coefficients of  $Al_{0.8}Ga_{0.2}As$  are such that  $M_e$  rises more rapidly than  $M_{mix}$  (Fig. 6.2) (Ng et al., 2001).

Reducing the  $p^+$  layer to a thickness less than one electron recombination length decreases the size of the additional peak and improves the device's efficiency at low

(< 2 keV) energies. Practicalities of wafer growth may limit the  $p^+$  layer thickness to values larger than 0.01  $\mu\text{m}$ . With such a thin  $p^+$  layer, impurities from the ohmic contact may penetrate through the layer and into the low doping, high field region. This would adversely affect the doping and field characteristics.

Increasing the efficiency of an abrupt  $p^+p^-n^+$  or  $p^+i-n^+$  type diode to be operated in avalanche mode by growing a thicker  $p^-$  (or  $i$ ) layer will lead to degraded spectral resolution in avalanche mode because the mixed avalanche gain is a function of photon interaction depth,  $x$ , (Eqs. 2.24 – 2.26 and **Fig. 6.4**), except in the special case when  $M_e(x)$  balances with  $M_h(x)$  to give constant  $M_{mix}(x)$ . To operate in avalanche mode and maintain the spectral resolution, it is necessary to use a graded doping profile across the region or adopt a reach-through/SAM APD design.

The temperature,  $T$ , dependence of the electron and hole ionisation coefficients in  $\text{Al}_{0.8}\text{Ga}_{0.2}\text{As}$  were determined using soft energy X-ray measurements on  $\text{Al}_{0.8}\text{Ga}_{0.2}\text{As}$   $p^+p^-n^+$  APDs operated at  $1/E = 1.796 \times 10^{-6}$  cm/V for  $+80\text{ }^\circ\text{C} \leq T \leq -20\text{ }^\circ\text{C}$ . For the full temperature range,  $M_e$  and  $M_{mix}$ , were measured from experimental X-ray spectra and  $M_h$  was predicted from the model. The change in avalanche multiplication factors within that temperature range was found to be significant ( $M_e$ ,  $M_{mix}$  and  $M_h$  at  $-20\text{ }^\circ\text{C}$  are approximately a factor of two larger than at  $+80\text{ }^\circ\text{C}$ ). The variation of multiplication factor with temperature suggests that whilst  $\text{Al}_{0.8}\text{Ga}_{0.2}\text{As}$   $p^+p^-n^+$  APDs can successfully operate uncooled for photon counting X-ray detection at temperatures between  $+80\text{ }^\circ\text{C}$  and  $-20\text{ }^\circ\text{C}$ , it is important to maintain a constant temperature during spectrum accumulation to prevent variation of the multiplication factors and degradation of the spectrum.

# Chapter 7 High temperature semi-transparent 4H-SiC Schottky photodiodes

## 7.1 Introduction

Previously, silicon carbide diodes have been investigated as detectors for applications in many sensing fields including UV (Hu et al., 2008),  $\alpha$ -particle detection (Nava et al., 1999) (Ruddy et al., 2006) and X-ray spectroscopy (Lees et al., 2007) (Bertuccio, 2005) (Bertuccio et al., 2001, 2003, 2004a, 2004b, 2011) (Nava et al., 2008). There has been much interest in SiC for radiation detectors in recent years because its wide band gap (3.23 eV for 4H-SiC) (Goldberg et al., 2001), radiation hardness (Lees et al., 2009) (Ruddy & Siedel, 2006) and commercial availability make it attractive for the manufacture of sensors for extreme (high temperature, intense radiation) environments. It is also suitable as a material for capacitive gas sensors (see the review by Wright & Horsfall (2007)) for the detection of rapidly varying concentrations of gases at temperatures of hundreds of degrees Celsius in, for example, vehicle exhausts, and for the monitoring of volcanoes (Weng et al., 2007). There are also efforts to manufacture SiC JFETs (Neudeck et al., 2009), (Bhatnagar et al., 2007), (Wright and Horsfall, 2007); if JFETs suitable for use in ultra-low noise charge sensitive preamplifiers could be produced so that signal amplification could be integrated on chip with SiC detectors, this would potentially reduce electronic noise (by reducing the parallel white noise component (§2.6.3) from the JFET's leakage current) and eliminate the temperature sensitive silicon preamplifier electronics currently used, improving detector performance. SiC exists in many different polytypes, including 4H and 6H, which are the two polytypes most commonly researched because they are available commercially. All the SiC diodes in this thesis are 4H-SiC; 4H-SiC has a wider band gap (3.23 eV) than 6H-SiC (3.0 eV (Goldberg et al., 2001)) so this should result in lower leakage current at high temperatures.

At the University of Leicester, the SiC detector development programme in collaboration with Newcastle University has produced X-ray sensitive semi-transparent silicon carbide Schottky photodiodes, see §2.3 and Lees et al. (2007). X-ray photon

counting SiC photodiodes from this programme have already been reported operating at room temperature and have been shown to function as photon counting X-ray spectrometers after proton irradiation (total dose =  $10^{13}$  cm<sup>-2</sup> at 50 MeV) (Lees et al., 2009).

In this chapter, reports are made of experiments with semi-transparent silicon carbide Schottky photodiodes illuminated by <sup>55</sup>Fe and <sup>109</sup>Cd radioisotope X-ray sources investigating the suitability of these diodes as detectors for X-ray photon counting spectroscopy in high temperature environments. The detectors are shown to operate as X-ray spectrometers at energies between 5.9 keV and 25 keV at temperatures from -30 °C to +80 °C with spectral resolutions (FWHM) between 1.6 keV and 2.5 keV.

## 7.2 Diode fabrication and design

Square (250 μm × 250 μm) semi-transparent silicon carbide Schottky diodes in 2 × 2 and 3 × 3 arrays of varying pixel separation (10 – 50 μm) were fabricated at Newcastle University from commercial wafers from Cree Inc. (Cree Inc., 2011) as per Lees et al. (2007). The devices were fabricated in array form to enable future research into pixel arrays. The layout of the diodes fabricated is shown in **Fig. 7.1**. The wafers had a 45 μm 4H-SiC epitaxial layer (n type doping (nitrogen), density =  $7.7 \times 10^{14}$  cm<sup>-3</sup>) on top of a 370 μm 4H-SiC n<sup>+</sup> substrate (doping density =  $2 \times 10^{18}$  cm<sup>-3</sup>). A 25 nm thick thermal oxide passivation layer was grown on the epitaxial layer. Ti/Ni ohmic contacts were deposited on the opposite side of the substrate and annealed at 1100 °C for 800 seconds to form the rear contact of each diode. Windows were etched in the front side passivation layer and 3 nm of titanium and 12 nm of nickel were deposited by e-beam evaporation and annealed at 600 °C to form 18 nm thick NiSi Schottky contacts. A gold bond pad and square annular contact (200 nm thick) were deposited on top of a 4 nm chromium adhesion layer for each pixel.

When a reverse bias is applied to a Schottky diode, the epitaxial layer depletes from the Schottky contact to form the active detection region of the device. The depletion depth is dependent on the applied reverse bias (Eq. 2.4). A graph showing the calculated thickness of depletion layer with reverse bias for the devices reported in this chapter is given in **Fig. 7.2**. The quantum efficiency of the devices is discussed in §7.6.

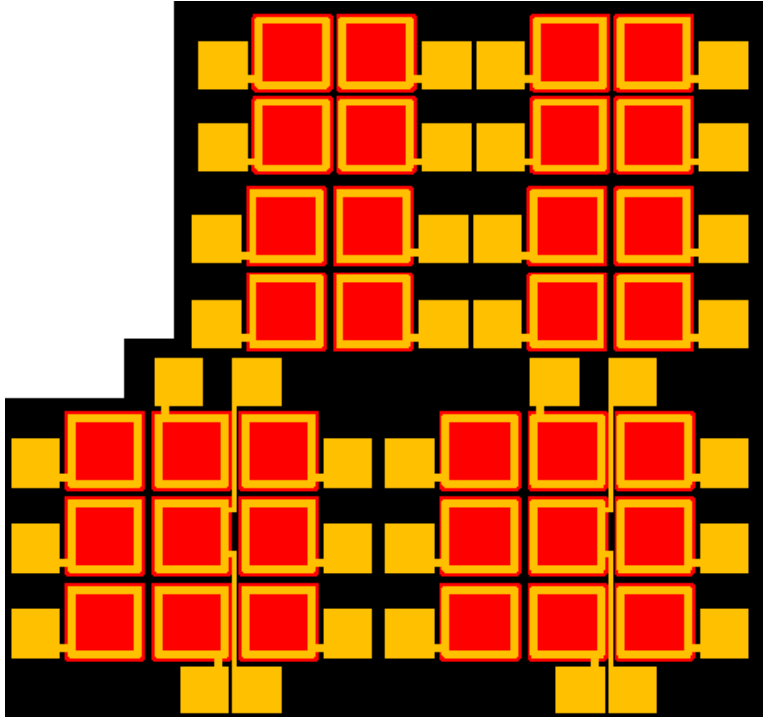


**Fig. 7.1.** Diagram of a section of the SiC wafer layout showing the  $2 \times 2$  and  $3 \times 3$   $250 \mu\text{m} \times 250 \mu\text{m}$  diode arrays. In the diagram, black represents the passivation layer, red represents the Schottky contact and gold represents the bond pads and top contacts.

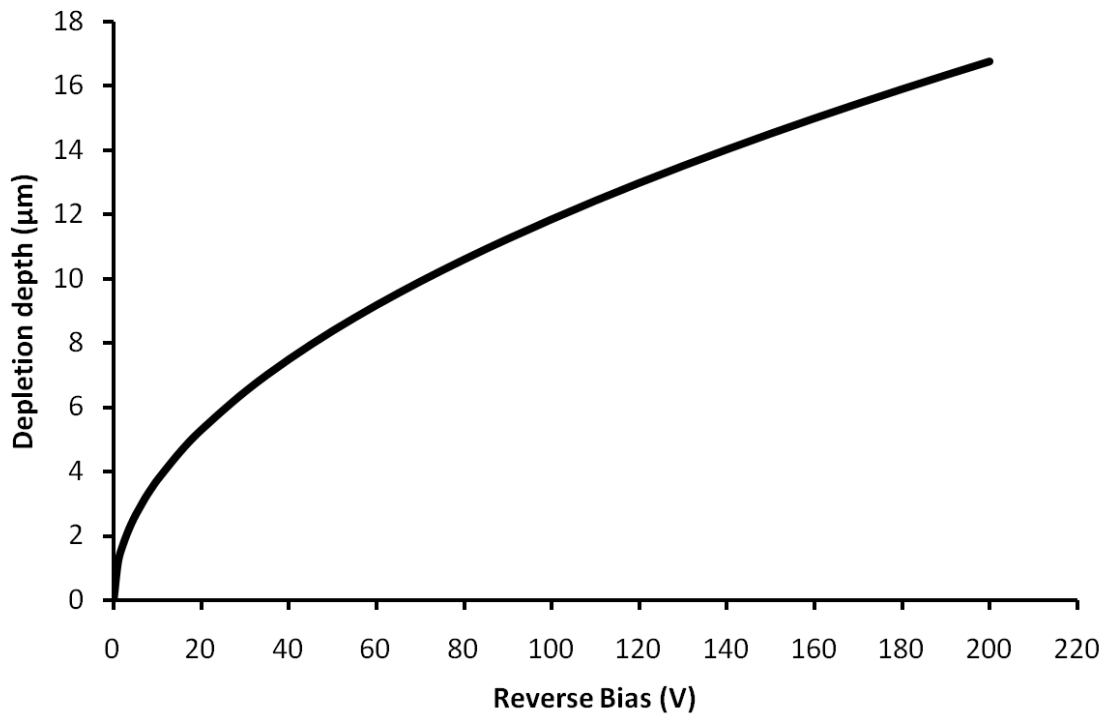


**Fig. 7.2.** The calculated depletion depth as a function of reverse bias for the SiC diodes used in this work.

### 7.3 Leakage current measurements

The leakage current characteristics of the SiC diodes were investigated as described in §4.4. After initial room temperature (20 °C)  $I$ - $V$  testing, a representative diode, D1, was selected for more extensive varied temperature characterisation. The  $I$ - $V$  curve obtained with diode D1 at 20 °C is shown in **Fig. 7.3**. The leakage current was measured for reverse biases up to 120 V, inclusive. While reverse biases  $> 80$  V were achievable when the diodes were new, after a few months the diodes became unstable at reverse biases  $> 80$  V (resulting in breakdown), even though their performance at reverse biases  $\leq 80$  V remained the same. Because of this failure mode, the X-ray measurements reported in this chapter were taken with the diodes reverse biased at 80 V. At reverse biases  $\leq 50$  V, the leakage currents were not measurable because they were smaller than the limit ( $\sim 0.05$  pA) of the current amplifier (Keithley Instruments Inc., 1975). At a reverse bias of 80 V (electric field = 75.5 kV/cm), the leakage current was 1.5 pA (leakage current density = 2.4 nA/cm<sup>2</sup>).

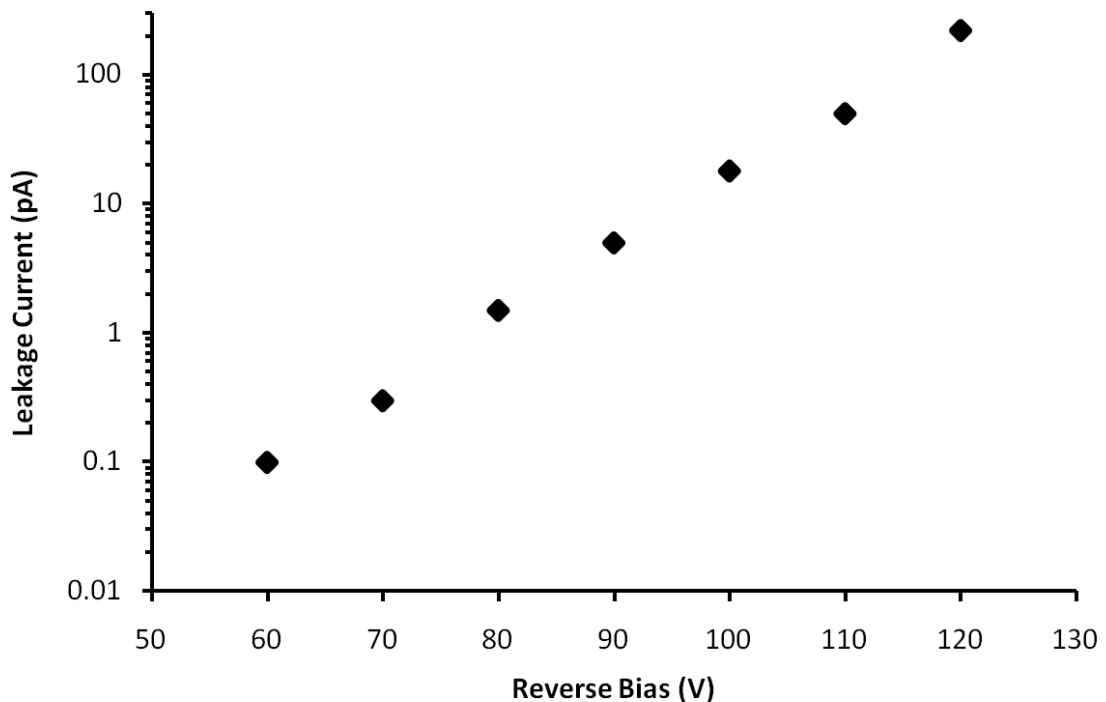


**Fig. 7.3.** The variation of leakage current with reverse bias for SiC diode D1 operated at 20 °C.

To measure the temperature dependence of the leakage current of diode D1 when reverse biased at 80 V, measurements were taken from 80 °C to -30 °C using the procedure and equipment described in §4.4. The results are shown in **Fig. 7.4**. It can

be seen that by starting at 80 °C and reducing the temperature in 10 °C steps, the leakage current recorded at 20 °C had reduced to 0.6 pA (0.96 nA/cm<sup>2</sup>) from 1.5 pA as recorded at 20 °C and 80 V in the room temperature *I-V* testing. The reason for this reduction in leakage current is presently unknown, but it is possibly due to the evaporation of moisture from the diodes and mountings, which may have occurred at high temperature; when the diodes were left unbiased in laboratory air (relative humidity ~ 40%) at room temperature for a few days and then measured again without heating, the leakage current would return to its original value of 1.5 pA. At 80 °C the leakage current was 8.1 pA (12.96 nA/cm<sup>2</sup>), 13.5 times greater than at 20 °C (0.96 nA/cm<sup>2</sup>).

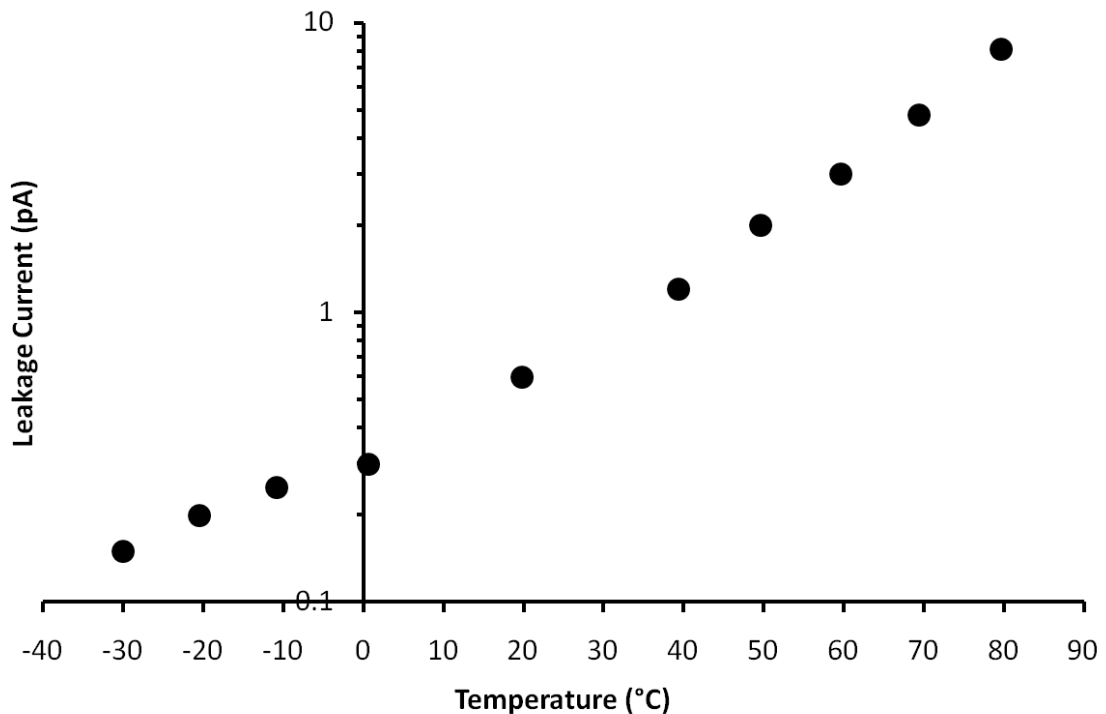


*Fig. 7.4. The temperature dependence of the leakage current of SiC diode D1 reverse biased at 80 V (filled circles).*

#### 7.4 X-ray spectral resolution measurements

To characterise the spectroscopic performance of the diodes, measurements were obtained as per §4.5 except that the radioisotope X-ray source was positioned 5 mm above the diode, instead of 3 mm. <sup>55</sup>Fe (~10 MBq) and <sup>109</sup>Cd (~0.06 MBq) radioisotope X-ray sources were used to characterise the spectral performance of the diodes reverse biased at 80 V at 5.9 keV (Mn K $\alpha$  from <sup>55</sup>Fe) and 22.16 keV (Ag K $\alpha_1$  from <sup>109</sup>Cd), at temperatures from 80 °C to -30 °C and 80 °C to 20 °C, respectively. Example spectra

from the  $^{55}\text{Fe}$  radioisotope X-ray source (accumulation time 1000 sec) and  $^{109}\text{Cd}$  radioisotope source (accumulation time = 345000 sec) at 20 °C are shown in **Fig. 7.5** and **Fig. 7.6**.  $^{109}\text{Cd}$  spectra were acquired at only three temperatures (80, 50 and 20 °C) due to the long accumulation time required for each spectrum.

The peak shown in **Fig. 7.5** from the  $^{55}\text{Fe}$  radioisotope X-ray source, is a combined peak composed of the Mn  $K\alpha$  (5.9 keV) and Mn  $K\beta$  (6.5 keV) emissions from the  $^{55}\text{Fe}$  X-ray source; the present spectral resolution of the system is insufficient to individually resolve these lines so they contribute to a single peak. The individually fitted Mn  $K\alpha$  and Mn  $K\beta$  components are shown with dashed lines in the figure. The Mn  $K\alpha$  and  $K\beta$  peaks were fitted assuming their emissions were in the ratio measured by Schötzig (2000) and that the FWHM of the  $K\alpha$  and  $K\beta$  peaks were identical. The FWHM were adjusted to give good agreement between the combined fitted lines and the peak in the measured spectrum (see **Fig. 7.5**). In the experimentally obtained spectrum, the low energy threshold was set at 2.6 keV to minimise counts from the zero energy noise peak. For the  $^{109}\text{Cd}$  spectrum in **Fig. 7.6**, the peak shown at 22 keV is the combined Ag  $K\alpha_1$  (22.16 keV) and Ag  $K\alpha_2$  (21.99 keV) peak. The peak at 25 keV is the combined Ag  $K\beta_1$  (24.94 keV), Ag  $K\beta_2$  (25.46 keV) and Ag  $K\beta_3$  (24.91 keV) peaks, which are too close together to be individually resolved by the detector. The individual Ag  $K\alpha_1$  and  $K\alpha_2$  peaks were fitted as for the  $^{55}\text{Fe}$  Mn  $K\alpha$  and  $K\beta$  peaks (above) except that the Ag  $K\alpha$  peaks were assumed to be in the ratio measured by Xiaolong et al. (2010). The peak at  $\approx 6$  keV is hypothesised to be a combination of Cr  $K\alpha$ , Fe  $K\alpha$  and Ni  $K\alpha$  fluorescence lines from the interaction of the  $^{109}\text{Cd}$  Ag  $K\alpha$  and  $K\beta$  X-rays with the stainless steel capsule of the source. The Ag peaks in the spectrum are emissions from the  $^{109}\text{Cd}$  source. The low energy threshold was set higher (3.5 keV) in this spectrum because the low activity of the source means a longer accumulation time is required. This longer accumulation time results in a larger zero energy noise peak and more counts from the noise peak's tail encroaching on the spectrum. The spectral resolution (FWHM) measured at each temperature for 5.9 keV and 22.16 keV is shown in **Fig. 7.7**. The spectral resolution (FWHM) measured with the diodes at 5.9 keV and 22.16 keV, at temperatures  $\leq 20$  °C, is  $\approx 1.6$  keV. When the temperature of the diode and preamplifier is increased to 80 °C, the spectral resolution increases to 2.5 keV FWHM at 5.9 keV and 2.27 keV FWHM at 22.16 keV.

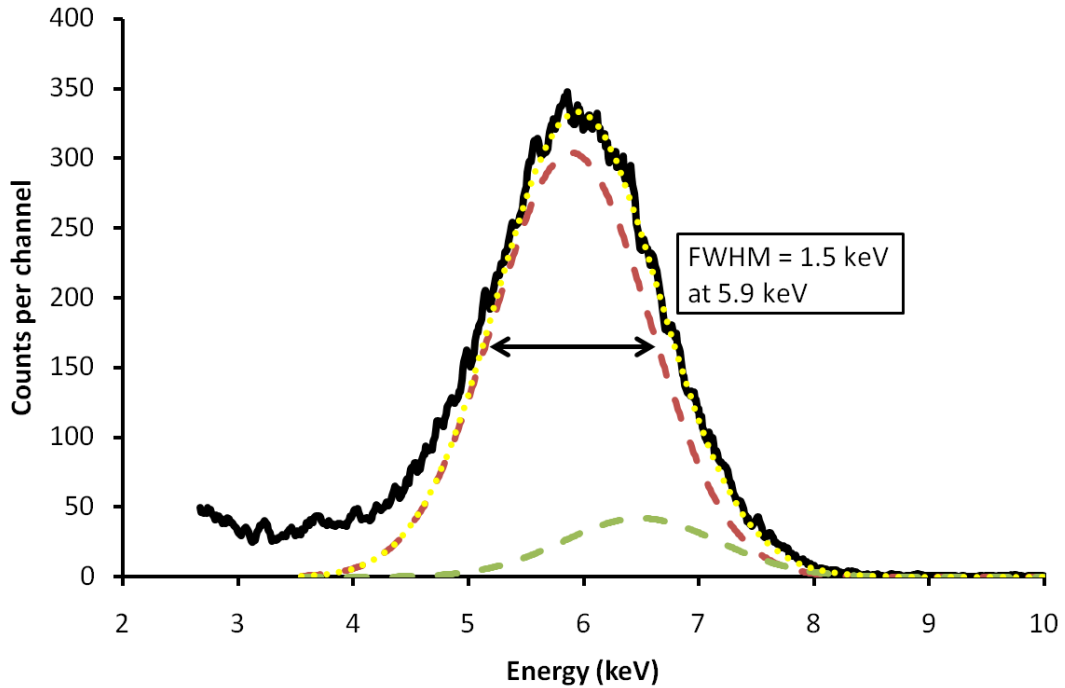


**Fig. 7.5.** An  $^{55}\text{Fe}$  X-ray spectrum obtained with SiC diode D1 at 20 °C (solid black line). The individually fitted Mn  $\text{K}\alpha$  (5.9 keV) (dashed red line) and Mn  $\text{K}\beta$  (6.5 keV) (dashed olive line) peaks, along with their combination (dotted yellow line) are also shown.

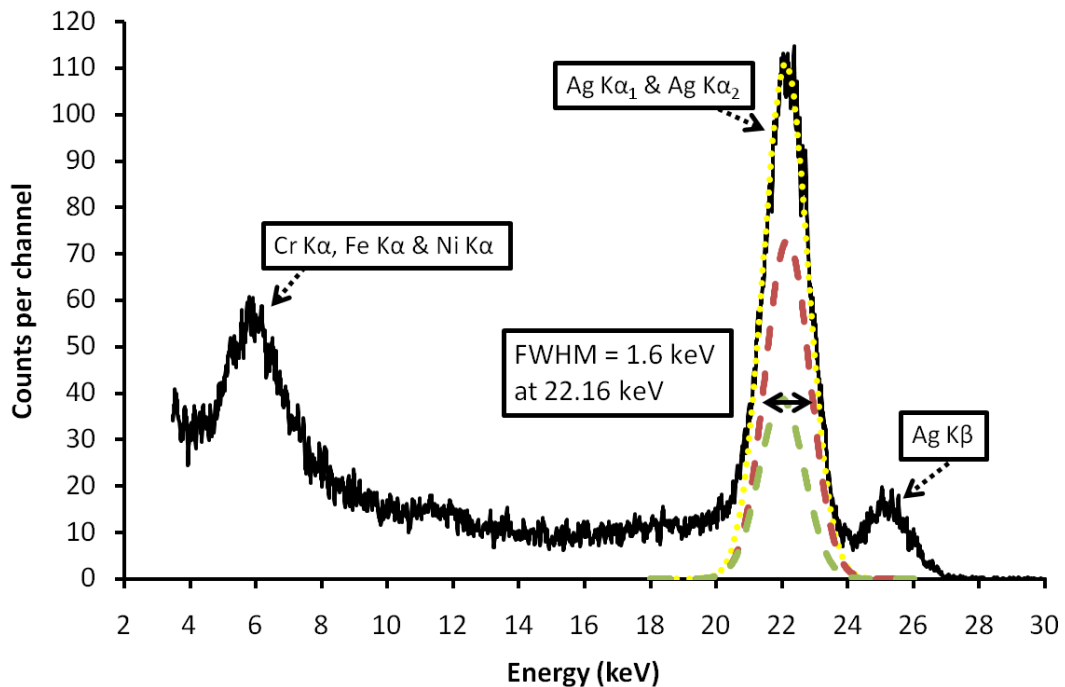


**Fig. 7.6.** A typical  $^{109}\text{Cd}$  X-ray spectrum obtained with SiC diode D1 at 20 °C (solid black line), see text. The individually fitted Ag  $\text{K}\alpha_1$  (22.16 keV) (dashed red line) and Ag  $\text{K}\alpha_2$  (21.99 keV) (dashed olive line) peaks, along with their combination (dotted yellow line) are also shown.

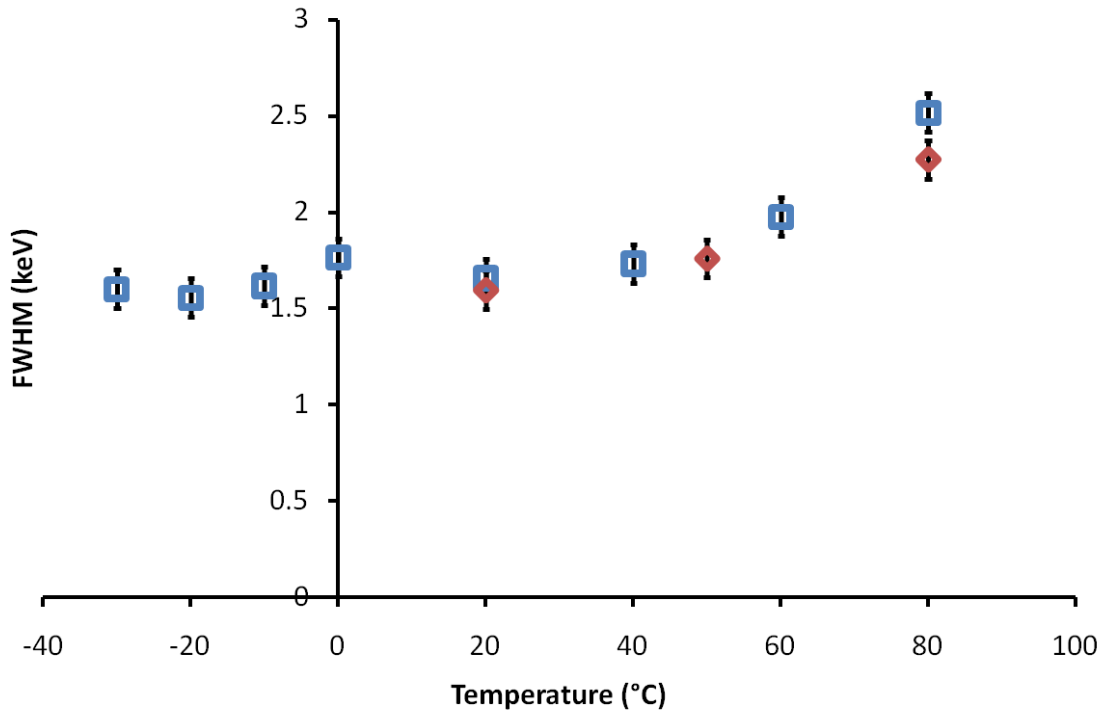


**Fig. 7.7.** The temperature dependence of the spectral resolution (FWHM) at 5.9 keV (open blue squares) and 22.16 keV (open red diamonds).

## 7.5 Noise analysis

The spectral resolution obtained with the semi-transparent SiC Schottky photodiodes reported in this thesis is much poorer across the whole of the temperature range than the Fano limited spectral resolution (FWHM) of SiC (160 eV at 5.9 keV at 30 °C, 166 eV at 5.9 keV at 100 °C) (Fano factor = 0.100 and 0.108 at 30 °C and 100 °C, respectively (Bertuccio et al., 2011)). To assess the components of the noise leading to the measured spectral resolution of the SiC detectors reported here, the relations given in Chapter 2 were used. The detector's parallel white noise contribution,  $N_{PW}$ , was calculated for each temperature (Eqs. 2.16 and 2.17, with  $A_3 = 2$ ) and subtracted in quadrature, along with the Fano noise (Bertuccio et al., 2011), from the total system noise measured in §7.4. **Fig. 7.8** shows the noise contributions from the Fano statistics,  $N_F$ , detector parallel white noise,  $N_{PW}$ , and the noise from the remaining components,  $N_E$ , i.e. series white noise, induced gate current noise,  $1/f$  noise, dielectric noise and JFET parallel white noise (which was estimated to be 0.10, 0.11 and 0.50 keV at -10, 20 and 50 °C, respectively (Siliconix, 1997)). From this analysis it can be seen that it is  $N_E$  which gives rise to the bulk of the total noise.

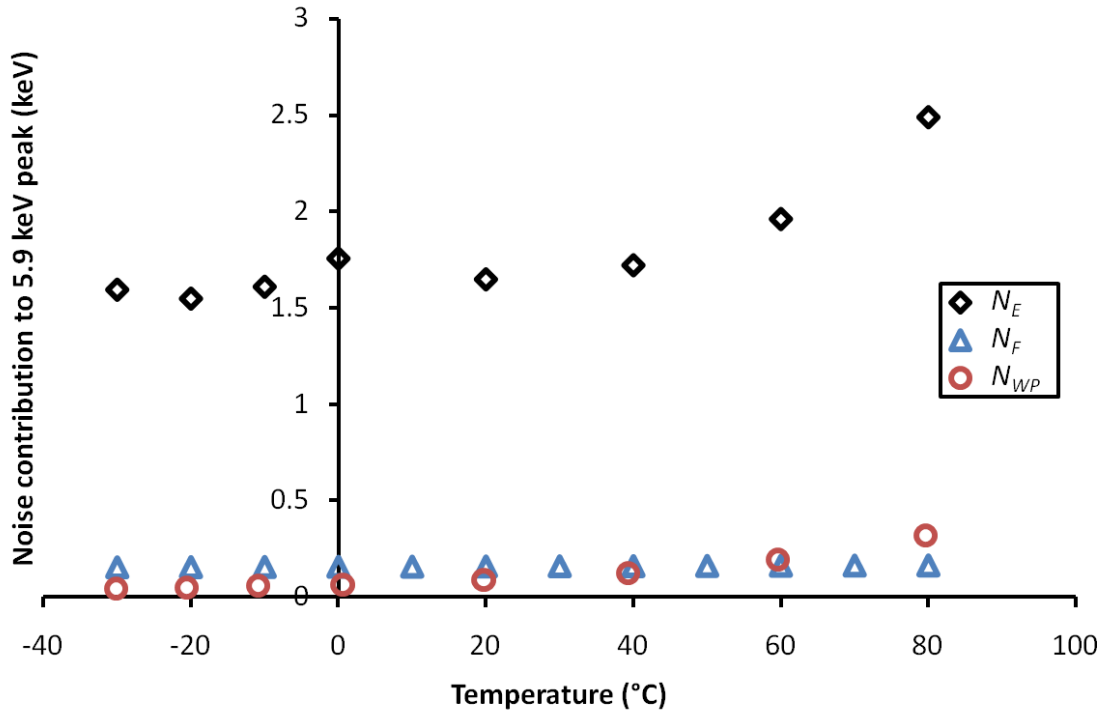


**Fig. 7.8.** The calculated noise contributions of the Fano noise ( $N_F$ , blue open triangles), detector parallel white noise ( $N_{PW}$ , red open circles) and the remaining noise of the system (see text),  $N_E$  (black open diamonds), at 5.9 keV over the temperature range 80 °C to -30 °C.

When the measured spectral resolutions (FWHMs at 5.9 keV at 20 °C) of the SiC ( $\omega_{EHP} = 7.8$  eV),  $\text{Al}_{0.8}\text{Ga}_{0.2}\text{As}$  ( $\omega_{EHP} = 5.25$  eV) (Chapter 4) and GaAs ( $\omega_{EHP} = 4.2$  eV) (Chapter 5) diodes are compared in units of  $e^-$  r.m.s. (these units normalise the effect of different electron-hole pair creation energies), the resolutions are similar (**Table 7.1**). From this, it can be seen that in the same way the bulk of the improvement in spectral resolution (measured in keV) of the GaAs diodes over the  $\text{Al}_{0.8}\text{Ga}_{0.2}\text{As}$  diodes is primarily attributed to the lower electron-hole pair creation energy of GaAs (§5.4), so can the poorer spectral resolution of the SiC diodes be attributed to SiC's higher electron-hole pair creation energy. This greater electron-hole pair creation energy reduces the number of electron-hole pairs generated per keV of input photon energy. This leads to a poorer spectral resolution in units of keV (FWHM) but similar spectral resolutions,  $\Delta E$ , in units of  $e^-$  r.m.s. For the temperature range investigated, with the presently used preamplifier electronics, the benefit of the lower leakage current of the SiC diodes is outweighed by the higher electron-hole pair creation energy of SiC in the balancing of terms to achieve the best spectral resolution.

	<b>Electron-hole pair creation energy (eV)</b>	<b>FWHM at 5.9 keV (keV)</b>	<b><math>\Delta E</math> at 5.9 keV (e<sup>-</sup> r.m.s.)</b>
<b>GaAs</b>	4.2	0.80	80.71
<b>Al<sub>0.8</sub>Ga<sub>0.2</sub>As</b>	5.25	1.07	86.36
<b>SiC</b>	7.8	1.60	86.91

**Table 7.1.** The spectral resolutions (in FWHM keV and e<sup>-</sup> r.m.s.) achieved at 20 °C with the GaAs, Al<sub>0.8</sub>Ga<sub>0.2</sub>As and SiC detectors reported in this thesis.

## 7.6 Detector quantum efficiency

The depletion depth of the Schottky diodes varies with applied reverse bias (see Eq. 2.4, §7.2 and **Fig. 7.2**). The calculated quantum efficiency (Eq. 2.1, given Eq. 2.4) of the devices at 5.9 keV and 22.16 keV with varied reverse bias is shown in **Fig. 7.9**. At 80 V (the reverse bias used for the X-ray spectral measurements in §7.4), the calculated depletion depth is 10.6  $\mu\text{m}$ . The quantum efficiency (for X-ray energies up to 30 keV) of the devices operated at 80 V is shown in **Fig. 7.10**. At 5.9 keV and 22.16 keV the calculated quantum efficiencies are 0.31 and 0.007, respectively. At 5.9 keV, the efficiency of the SiC devices is much greater than the efficiency of the GaAs diodes (2  $\mu\text{m}$  i layer, 0.2  $\mu\text{m}$  p<sup>+</sup> layer, 0.152 quantum efficiency) (Chapter 5) and Al<sub>0.8</sub>Ga<sub>0.2</sub>As diodes (1  $\mu\text{m}$  i layer, 1  $\mu\text{m}$  p<sup>+</sup> layer, 0.033 quantum efficiency) (Chapter 4). However, at 22.16 keV, despite the thicker depletion layer (10.6  $\mu\text{m}$ ), the calculated efficiency of the SiC devices (0.007) is lower than for the GaAs (0.034) and Al<sub>0.8</sub>Ga<sub>0.2</sub>As (0.011) diodes at this energy because of SiC's lower density (3.21 g cm<sup>-3</sup>, **Table 2.1**). The quantum efficiency of the SiC devices reported here is lower than for some other SiC diodes which operate at higher reverse biases (e.g. 300 V) with greater depletion depths (e.g. 25  $\mu\text{m}$ ) and correspondingly greater quantum efficiencies (0.54 at 5.9 keV, 0.016 at 22.16 keV) (Bertuccio et al., 2011). However, it is notable that at 22.16 keV, even with a 25  $\mu\text{m}$  depletion depth, SiC devices still have only half the calculated quantum efficiency of a much thinner (2  $\mu\text{m}$ ) GaAs diode (Chapter 5). In each case, the quantum efficiency is still less than that achievable with a very thick (500  $\mu\text{m}$ ) silicon diode (0.29 at 22.16 keV).

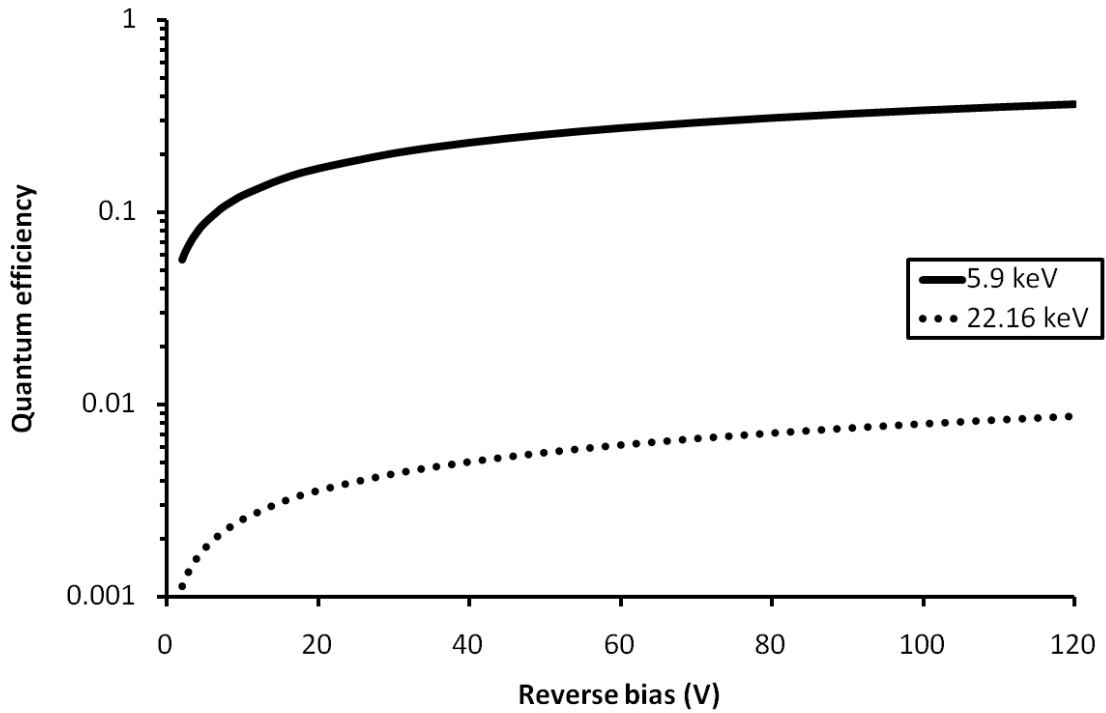


**Fig. 7.9.** Calculated quantum efficiency for the SiC devices at 5.9 keV (solid line) and 22.16 keV (dashed line) with varied reverse bias.

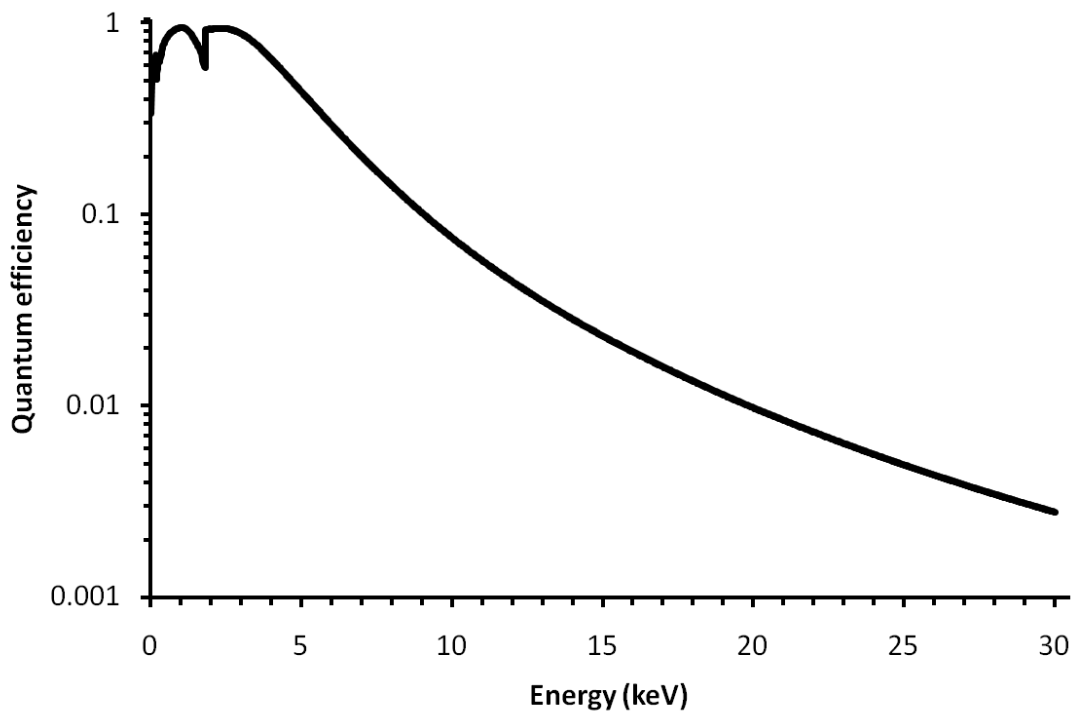


**Fig. 7.10.** Quantum efficiency with varying energy (up to 30 keV) of the SiC devices reverse biased at 80 V (depletion depth = 10.6  $\mu\text{m}$ ). The discontinuity at 1.839 keV is the silicon K edge.

Since the depletion depth (and hence quantum efficiency) of the SiC device varies with reverse bias, it was possible to measure the relative change in efficiency by operating the diode at different reverse biases. To perform these measurements, the same experimental conditions as §7.4 were used, except that the temperature was held constant at 20 °C. The diode was illuminated with the  $^{55}\text{Fe}$  radioisotope source and reverse biased at 40, 80 and 120 V, corresponding to calculated depletion depths of 7.5, 10.6 and 13.0  $\mu\text{m}$  and calculated quantum efficiencies at 5.9 keV of 0.23, 0.31 and 0.36, respectively. Four  $^{55}\text{Fe}$  spectra were accumulated at each reverse bias. The number of counts under the combined Mn  $K\alpha$  (5.9 keV) and  $K\beta$  (6.5 keV) peak in each spectrum was counted and the mean was calculated at each reverse bias. The number of counts under the peak at each reverse bias was divided by the number of counts under the peak with the diode reverse biased at 40 V to obtain efficiencies relative to this value. The results are shown in **Fig. 7.11** along with the calculated 5.9 keV data from **Fig. 7.9** replotted as efficiencies relative to 40 V. The experimentally obtained data suggest that the efficiency of the diodes increases more rapidly than predicted, possibly as a result of the doping in the epilayer not being constant with depth, but more measurements would be required in order to verify this as the cause.

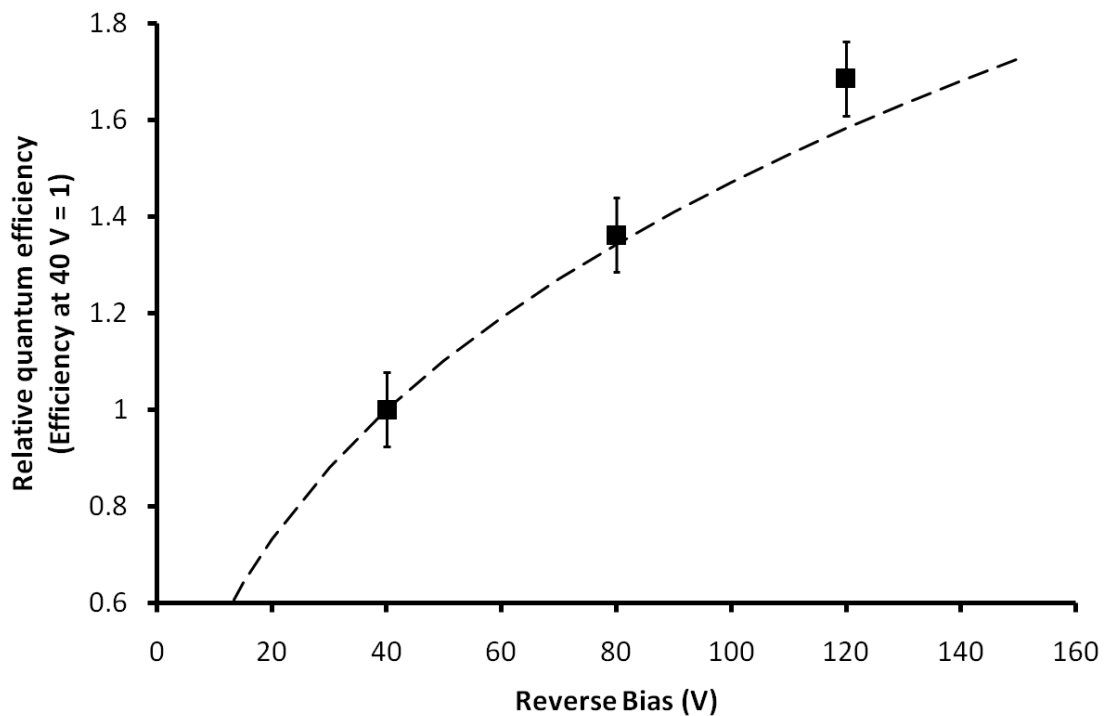


**Fig. 7.11.** The measured relative efficiency of the SiC diodes at 5.9 keV with varied reverse bias (filled squares) compared with calculated efficiencies (dashed line).

## 7.7 Conclusions and discussion

The spectroscopic X-ray performance of semi-transparent silicon carbide Schottky photodiodes as measured by the FWHM of peaks from  $^{55}\text{Fe}$  and  $^{109}\text{Cd}$  radioisotope X-ray sources has been investigated at temperatures from +80 °C to -30 °C. The diodes have been shown to operate at high temperature (up to 80 °C) with low leakage current (8.1 pA at 80 °C) and to operate as photon counting spectrometers sensitive to X-ray radiation in the range 5.9 keV to 25 keV, with promising spectral resolution (1.6 – 2.5 keV FWHM) over the measured temperature range.

The larger band gap and higher electron-hole pair creation energy of SiC (compared to  $\text{Al}_{0.8}\text{Ga}_{0.2}\text{As}$  and GaAs) reduces the leakage current of the devices, but also makes the energy resolution obtained using the detector with the current preamplifier electronics poorer than that achieved with the other devices reported in this thesis;  $\text{Al}_{0.8}\text{Ga}_{0.2}\text{As}$  (Chapter 4), 1.07 keV FWHM at 5.9 keV at 20 °C; GaAs (Chapter 5), 0.8 keV FWHM at 5.9 keV at 20 °C). However, Bertuccio et al. (2011) have shown that with ultra-low noise preamplifier electronics, SiC X-ray detectors are able to achieve excellent spectral resolution even at high temperature (FWHM at 5.9 keV: 233 eV at 100 °C, 196 eV at 30 °C). These results, along with those reported in this thesis, suggest that SiC Schottky diodes are promising devices for X-ray detection in high temperature environments. The benefit of SiC's larger electron-hole pair creation energy over materials with lower electron-hole pair creation energy (such as  $\text{Al}_{0.8}\text{Ga}_{0.2}\text{As}$  or GaAs) may become increasingly significant at even higher temperatures where the spectral resolution may be limited by device leakage current rather than preamplifier noise. Advancements in SiC JFET technology (Neudeck et al., 2009) (Bhatnagar et al., 2007) (Wright & Horsfall, 2007) may also open the possibility of integrating the front end JFET of the preamplifier with the detector, potentially reducing noise and the temperature sensitivity of preamplifier by removing the highly temperature sensitive silicon based preamplifier components. The potential for high temperature operation of SiC detectors together with their radiation tolerance (Lees et al., 2009) and the possibility of SiC based preamplifiers are likely to make SiC detectors attractive options in future for sensors that need to survive in extreme environments.

## Chapter 8 Summary, conclusions and further work

### 8.1 Summary and conclusions

$\text{Al}_{0.8}\text{Ga}_{0.2}\text{As}$ , GaAs and SiC photodiodes have been investigated for their suitability as spectroscopic soft X-ray (< 25 keV) detectors at high temperature.

$\text{Al}_{0.8}\text{Ga}_{0.2}\text{As}$  non-avalanche mesa  $\text{p}^+\text{-i-n}^+$  photodiodes have been shown to function as X-ray photon counting detectors over a temperature,  $T$ , range,  $-30\text{ }^\circ\text{C} \leq T \leq 90\text{ }^\circ\text{C}$ , with promising energy resolution of the full system (0.9 – 2.5 keV, FWHM at 5.9 keV). At 20 °C, the measured spectral resolution was ~1.1 keV FWHM at 5.9 keV. The main source of noise contributing to the measured spectral resolution has been determined, by amplifier shaping time noise analysis, to be dielectric noise. This is suspected to be from the packaging material surrounding the detector and input JFET of the preamplifier. It has been predicted that if this noise could be eliminated, the spectral resolutions (FWHM at 5.9 keV) achievable at -10, +20 and +50 °C would improve to 332, 380 and 615 eV from the currently achievable 0.90, 1.07 and 1.35 keV, at a shaping amplifier time constant of 3  $\mu\text{s}$  (**Fig. 4.13**).

GaAs non-avalanche mesa  $\text{p}^+\text{-i-n}^+$  diodes of similar design have also been investigated. They have been shown to have better spectral resolution (0.80 – 1.55 keV, FWHM at 5.9 keV) than the  $\text{Al}_{0.8}\text{Ga}_{0.2}\text{As}$  devices over the measured temperature range,  $-30\text{ }^\circ\text{C} \leq T \leq 80\text{ }^\circ\text{C}$ . At 20 °C, the measured spectral resolution was ~0.8 keV FWHM at 5.9 keV. The GaAs detectors were also shown to have a lower low energy threshold (1.4 keV) than the  $\text{Al}_{0.8}\text{Ga}_{0.2}\text{As}$  detectors (~2 keV). These better characteristics are primarily attributed to the lower electron-hole pair creation energy of GaAs (4.2 eV (Owens & Peacock, 2004)) compared with  $\text{Al}_{0.8}\text{Ga}_{0.2}\text{As}$  (5.25 eV (NSM Archive, 2004)) resulting in the production of larger numbers of charge carriers in GaAs for a given X-ray photon energy. The characterisation of the GaAs devices was extended to higher energies (< 25 keV) with experiments using a  $^{109}\text{Cd}$  radioisotope X-ray source and simulations from the Monte Carlo model (Chapter 3). This higher energy work demonstrated the

internal detector K shell fluorescence that results when the incident X-ray photon's energy is greater than the Ga and As K shell electron binding energies. The primary noise source contributing to the spectral resolution achievable with the GaAs detectors is, as for the  $\text{Al}_{0.8}\text{Ga}_{0.2}\text{As}$  detectors, the dielectric noise which can be attributed to the packaging of the diode and preamplifier input JFET. At -10, +20 and +50 °C if the dielectric noise was eliminated, the spectral resolutions achievable with the GaAs detectors have been estimated to be 351, 367 and 484 eV FWHM at 5.9 keV, respectively (**Fig. 5.8**).

The research conducted with the  $\text{p}^+\text{-i-n}^+$  non-avalanche photodiodes has advanced the state of the art for both  $\text{Al}_{0.8}\text{Ga}_{0.2}\text{As}$  and GaAs high temperature X-ray detectors. Devices of both materials have been shown to have potential for soft X-ray spectroscopy at high temperatures. If the quantum efficiency of the detectors can be increased by growing thicker devices and the electronic noise sources reduced (the spectral resolution improved) through redesign of the packaging of diode and preamplifier input JFET, as well as through improvements to the diode design and fabrication to reduce leakage currents,  $\text{Al}_{0.8}\text{Ga}_{0.2}\text{As}$  and GaAs based spectrometers are likely to find rapid adoption in both space based and terrestrial applications, where their tolerance of high temperatures will result in cost savings and simpler, more robust instrument design.

$\text{Al}_{0.8}\text{Ga}_{0.2}\text{As}$  soft X-ray photon counting avalanche photodiodes (APDs) were investigated experimentally and using the Monte Carlo model. A spectral anomaly which had previously been reported in X-ray spectra obtained with  $\text{Al}_{0.8}\text{Ga}_{0.2}\text{As}$  X-ray APDs (Lees et al., 2008) was predicted using the model and explained. Through new experimental and computer modelling results, it was shown that the additional peak reported by Lees et al., that emerged from the expected Mn  $K\alpha$  and  $K\beta$  peak from an  $^{55}\text{Fe}$  radioisotope source, when the  $\text{Al}_{0.8}\text{Ga}_{0.2}\text{As}$  APDs devices were operated in avalanche mode, was a consequence of the diode structure and the different multiplication factors achieved by charge carriers generated by X-ray photons absorbed at different positions in the diode. Understanding this phenomenon allowed a new method to be developed for determining the impact ionisation coefficients in semiconductor devices. This enabled the electron and hole impact ionisation coefficients of  $\text{Al}_{0.8}\text{Ga}_{0.2}\text{As}$  to be determined at X-ray energies, and their temperature dependence to be reported for the first time.

The derivation of the temperature dependence of the impact ionisation coefficients in  $\text{Al}_{0.8}\text{Ga}_{0.2}\text{As}$  has led to a better understanding of the properties of  $\text{Al}_{0.8}\text{Ga}_{0.2}\text{As}$  APDs in environments of high or fluctuating temperature, and prompted the discovery (Tan et al., 2011) that the established understanding of impact ionisation was incomplete and that the avalanche excess noise factor is inversely proportional to the number of charge carriers generated (**Fig. 2.7**). Determination of the temperature dependence of the ionisation coefficients of  $\text{Al}_{0.8}\text{Ga}_{0.2}\text{As}$  has shown that whilst APDs made of this material can operate at high temperature, and avalanche multiplication can be used to improve the signal to noise ratio at X-ray energies, it is essential that the temperature of the detector remains stable throughout the spectrum accumulation period in order to prevent the ionisation coefficients from varying and smearing the spectrum.

As part of an on-going SiC photodiode development programme, the high temperature X-ray spectral properties of Semi-Transparent SiC Schottky Diodes (STSSDs) were characterised. The temperature dependence of the X-ray spectral performance was investigated at energies from 5.9 keV to 25 keV. Over a temperature range  $-30\text{ }^{\circ}\text{C} \leq T \leq 80\text{ }^{\circ}\text{C}$ , it was found that the FWHM varied from 1.6 keV to 2.5 keV. At  $20\text{ }^{\circ}\text{C}$ , the measured spectral resolution was  $\sim 1.5\text{ keV}$  FWHM at 5.9 keV. The poorer resolutions achieved (compared with the  $\text{Al}_{0.8}\text{Ga}_{0.2}\text{As}$  and GaAs devices) were attributed to the greater electron-hole pair creation energy of SiC (7.8 eV) reducing the number of charge carriers generated. The relative increase in efficiency brought by increasing the reverse bias of the devices was investigated theoretically and experimentally. It was found that the relative efficiency increased more rapidly than theoretically predicted, possibly because of a non-uniform doping in the epilayer of the devices, although more measurements would be required to confirm this.

The work presented in this thesis has shown that compound semiconductor X-ray photodiodes made from  $\text{Al}_{0.8}\text{Ga}_{0.2}\text{As}$ , GaAs and SiC are all promising detectors for high temperature X-ray spectroscopy. The spectral resolutions reported here for these materials with the present preamplifier electronics are currently poorer at room temperature than have been reported with silicon drift detectors at  $20\text{ }^{\circ}\text{C}$  ( $\sim 0.3\text{ keV}$  FWHM at 5.9 keV) (Lechner et al., 2001) and silicon CCDs cooled to  $-90\text{ }^{\circ}\text{C}$  (130 eV FWHM at 5.9 keV) (Nakajima et al., 2005). However, the majority of the noise present with the  $\text{Al}_{0.8}\text{Ga}_{0.2}\text{As}$ , GaAs and SiC detectors appears to be from the packaging of the devices and the preamplifier electronics (see **Figs. 4.12, 5.7 & 7.8**) and improvements to

these aspects will result in much better spectral resolution (see **Figs. 5.8 & 4.13**). When coupled to ultra-low noise electronics (pulsar line FWHM = 113 eV at 30 °C, 163 eV at 100 °C), Bertuccio et al. (2011) have demonstrated SiC Schottky detectors with spectral resolutions (FWHM at 5.9 keV) of 196 eV at 30 °C and 233 eV at 100 °C, reinforcing a conclusion of this thesis that wide band gap compound semiconductor photon counting X-ray detectors are able to function at high temperature and with useful energy resolution.

Each material has advantages and disadvantages which must be must be balanced in order to select the most appropriate material for a specific application. The most notable example of such a trade-off is the balance that must be struck between selecting a material with a larger band gap to reduce thermally generated parallel white noise, and selecting a material with a low electron-hole pair creation energy to increase the number of charge carriers generated per keV of incoming photon energy. The trade-offs involved must be informed by the environment in which the instrument is intended to operate, as well the X-ray energy range of interest and preamplifier electronics and semiconductor material available.

With refinements to the diode packaging and preamplifier electronics to improve the spectral resolution, along with improvements in the quantum efficiencies of the detectors by the production of thicker devices, detectors made from  $\text{Al}_{0.8}\text{Ga}_{0.2}\text{As}$ , GaAs and SiC, will likely find use in applications where operation at high temperature is required. Real time in situ X-ray fluorescence condition monitoring of engine oil to detect signs of oil and engine wear in high value and high performance vehicles is one such potential terrestrial application. Space applications for wide band gap compound semiconductor detectors include X-ray fluorescence spectrometers for future planetary geology missions to high temperature environments such as Mercury, Venus and hydrothermal vents in the European Ocean (Thomson & Delaney, 2001), (Lowell & DuBose, 2005).

## **8.2 Further work**

Possibilities for continued work on  $\text{Al}_{0.8}\text{Ga}_{0.2}\text{As}$ , GaAs and SiC detectors abound. One area of research predicted to have an immediate payoff would be the development of low noise packaging for the detector and preamplifier input JFET. Custom packaging for the detector and JFET, perhaps using ceramic or Teflon, may reduce the noise

contribution from this area and improve the spectral resolution achievable with the detectors to such an extent that they become serious contenders for soft X-ray spectroscopy at room temperature and above, with comparable spectral resolution to a Silicon Drift Detector cooled to +20 °C (~300 eV FWHM at 5.9 keV) (Lechner et al., 2001). Development of FETs with lower leakage currents, ideally fabricated from the same material as the detector so that they can be integrated easily with the detector, would also be very beneficial as at higher temperatures the JFET leakage becomes increasingly significant.

In addition to obvious areas of future development such as thicker, more efficient devices, systematic studies of the processes used to manufacture the devices should be carried out to optimise the growth and quality of the wafers and the fabrication of the devices. The leakage currents of the GaAs and  $\text{Al}_x\text{Ga}_{1-x}\text{As}$  devices should be explored in more detail to reveal the relative importance of contributions from bulk and surface leakage. Trials investigating the suitability of various passivation materials (such as SU-8, SiN and SiO) (Hwang et al., 2001) for reducing surface leakage current should also be conducted.

Linear and two dimensional detector arrays should be fabricated and characterised to understand the pixel-to-pixel charge sharing and crosstalk effects that may be present in  $\text{Al}_x\text{Ga}_{1-x}\text{As}$ , GaAs and SiC detector arrays; this work will hopefully lead to the development of high temperature tolerant soft X-ray imaging devices. The model described in Chapter 3 could be extended to simulate these multi-pixel effects, and also include single-pixel partial charge collection and charge spreading. Larger area diodes should also be fabricated and characterised.

Synchrotron measurements, using very small spot size X-ray beams to measure the uniformity of response across the face of individual diodes and diodes in arrays would be useful to develop a better understanding of the material quality, electric field uniformity and charge collection in both avalanche and non-avalanche devices. The radiation hardness of photon counting  $\text{Al}_{0.8}\text{Ga}_{0.2}\text{As}$  and GaAs X-ray photodiodes should also be characterised, and the characterisation of semi-transparent silicon carbide (SiC) Schottky spectroscopic X-ray photon counting photodiodes extended beyond  $10^{13}$  protons/cm<sup>2</sup> at 50 MeV (Lees et al., 2009).

Through further laboratory experiments on the existing  $\text{Al}_{0.8}\text{Ga}_{0.2}\text{As}$  APDs, the temperature dependence of the ionisation coefficients at different electric fields could be measured using the method described in Chapter 6. This would enable the production of equations that parameterise ionisation coefficients in  $\text{Al}_{0.8}\text{Ga}_{0.2}\text{As}$  as a function of electric field and temperature. This technique could be extended to other  $\text{Al}_x\text{Ga}_{1-x}\text{As}$  alloys to characterise the temperature dependence of the ionisation coefficients with  $x$ , or even to different materials, subject to wafer and device availability. Further research into APDs could investigate more advanced device designs, such as separate absorption and multiplication region (SAM)  $\text{Al}_{0.8}\text{Ga}_{0.2}\text{As}$  APDs or even GaAs/ $\text{Al}_{0.8}\text{Ga}_{0.2}\text{As}$  SAM APDs which use GaAs for the absorber region (to take advantage of the lower electron-hole pair creation energy of GaAs) and  $\text{Al}_{0.8}\text{Ga}_{0.2}\text{As}$  in the avalanche region similarly to those of Lauter et al. (1995).

## Bibliography

**Abbey, A.F., Bennie, P.J., Turner, M.J.L., Altieri, B., Rives, S., 2003,** Cooling out the radiation damage on the XMM-Newton EPIC MOS CCDs, Nuclear Instruments and Methods in Physics Research A, Vol. 513, Iss. 1-2, pp. 136-142.

**Adachi, S., 1985,** GaAs, AlAs,  $\text{Al}_x\text{Ga}_{1-x}\text{As}$ : Material parameters for use in research and device applications, Journal of Applied Physics, Vol. 53, No. 3, pp. R1-R29.

**Advanced Measurement Technology Inc., 2008,** Ortec Easy-MCA-8k Digital Gamma-Ray Spectrometer Hardware User's Manual, Manual Revision A, Ortec Part No. 931044, Oak Ridge, TN, USA.

**Alig, R.C., Bloom, S., Struck, C.W., 1980,** Scattering by ionization and phonon emission in semiconductors, Physical Review B, Vol. 22, No. 12, pp. 5565-5582.

**Bentley Tribology Services, N.D.,** Sources of wear metals in oils analysis, <http://www.bentleytribology.com/publications/appnotes/app31.php>, last retrieved 28th April 2011.

**Bertuccio, G., 2005,** Prospect for energy resolving X-ray imaging with compound semiconductor pixel detectors, Nuclear Instruments and Methods A, Vol. 546, Iss. 1-2, pp. 232-241.

**Bertuccio, G. and Casiraghi, R., 2003,** Study of silicon carbide for X-ray detection and spectroscopy, IEEE Transactions on Nuclear Science, Vol. 50, No. 1, pp. 175-185.

**Bertuccio, G., Pullia, A., De Geronimo, G., 1996,** Criteria of choice of the front-end transistor for low noise preamplification of detector signals at sub-microsecond shaping times for X- and  $\gamma$ -ray spectroscopy, Nuclear Instruments and Methods A, Vol. 380, Iss. 1-2, pp. 301-307.

**Bertuccio, G., Casiraghi, R., and Nava, F., 2001,** Epitaxial Silicon Carbide for X-ray detection, IEEE Transactions on Nuclear Science, Vol. 48, No. 2, pp. 232-233.

**Bertuccio, G., Casiraghi, R., Maiocchi, D., Owens, A., Bavdaz, M., Peacock, A., Andersson, H., Nenonen, S., 2003**, Noise analysis of gallium arsenide pixel X-ray detectors coupled to ultra-low noise electronics, *IEEE Transactions on Nuclear Science*, Vol. 50, No. 3, pp. 723-728.

**Bertuccio, G., Casiraghi, R., Centronio, A., Lanzieri, C., Nava, F., 2004a**, A new generation of X-ray detectors based on silicon carbide, *Nuclear Instruments and Methods A*, Vol. 518, Iss. 1-2, pp. 433-435.

**Bertuccio, G., Casiraghi, R., Centronio, A., Lanzieri, C., Nava, F., 2004b**, Silicon carbide for high resolution X-ray detectors operating up to 100 °C, *Nuclear Instruments and Methods A*, Vol. 552, Iss. 3, pp. 413-419.

**Bertuccio, G., Caccia, S., Casiraghi, R., Lanzieri, C., 2006**, Possibility of Subelectron noise with room-temperature silicon carbide pixel detectors, *IEEE Transactions on Nuclear Science*, Vol. 53, No. 4, pp. 2421-2427.

**Bertuccio, G., Caccia, S., Puglisi, D., Macera, D., 2011**, Advances in silicon carbide X-ray detectors, *Nuclear Instruments and Methods A*, Vol. 652, Iss. 1, pp. 193-196.

**Bhatnagar, P., Wright, N.G., Horsfall, A.B., Vassilevski, K., Johnson, C.M., Uren, M.J., Hilton, K.P., Munday, A.G., Hydes, A.J., 2007**, High temperature characterisation of 4H-SiC VJFET, *Materials Science Forum*, Vol. 556-557, pp. 799-802.

**Brunetti, A., Sanchez del Rio, M., Golosio, B., Simionovici, A., Somogyi, A., 2004**, A library for X-ray matter interaction cross sections for X-ray fluorescence applications, *Spectrochimica Acta B*, Vol. 59, Iss. 10-11, pp. 1725-1731.

**Campbell, J.C., 2007**, Recent Advances in Telecommunications Avalanche Photodiodes, *Journal of Lightwave Technology*, Vol. 25, No. 1, pp. 109-121.

**Campbell, J.L., McDonald, L., Hopman, T., Papp, T., 2001**, Simulations of Si(Li) X-ray detector response, *X-ray Spectrometry*, Vol. 30, Iss. 4, pp. 230-241.

**Cappelletti, M.A., Cédola, A.P., Blancá, P., 2008**, Simulation of silicon PIN photodiodes for use in space-radiation environments, *Semiconductor Science and Technology*, Vol. 23, No. 2, 025007.

**Childs, P.A. and Leung, C.C.C., 1991**, An analysis of 'dead space' in semiconductors, *Journal of Physics: Condensed Matter*, Vol. 3, No. 41, pp. 8053-8057.

**Chollet, F., 2009**, SU-8: Thick photo-resist for MEMS, *Memscyclopedia*, <http://memscyclopedia.org/su8.html>, last retrieved 4th May 2011.

**Cree Inc., 2011**, Silicon carbide substrates and epitaxy, MAT-CATALOG.00P, Durham, North Carolina, USA.

**Cromer, D.T., and Liberman, D., 1970**, Relativistic calculation of anomalous scattering factors for X-rays, LASL Report LA-4403.

**Dapkus, L., Jasutis, C., Jucienė, V., Požela, J., Požela, K., Šilėnas, A., 2007**, A graded-gap X-ray detector with charge avalanche multiplication, *Lithuanian Journal of Physics*, Vol. 47, No. 1, pp. 37-40.

**David, J.P.R., and Tan, C.H., 2008**, Material Considerations for Avalanche Photodiodes, *IEEE Journal of Selected Topics in Quantum Electronics*, Vol. 14, No. 4, pp. 998-1009.

**Demeester, P., Ackaert, A., Coudenys, G., Moerman, I., Buydens, L., Pollentier, Van Daele, P., 1991**, *Progress in Crystal Growth and Characterization of Materials*, Vol. 22, Iss. 1-2, pp. 53-141.

**Design Environmental, N.D.**, Instruction Manual For Model FS55-65, Ebbw Vale, Gwent, UK.

**EG&G Ortec, N.D.**, Model 571 Spectroscopy Amplifier Operating and Service Manual, Rev. A, Part No. 733490, Oak Ridge, Tennessee, USA.

**Elsner, R.F., 2002**, Discovery of soft X-ray emission from Io, Europa, and the Io plasma torus, *The Astrophysical Journal*, Vol. 572, pp. 1077-1082.

**Erd, C., Owens, A., Brammertz, G., Bavdaz, M., Peacock, A., Lämsä, V., Nenonen, S., Andersson, H., Haack, N., 2002**, Hard X-ray test and evaluation of a prototype 32×32 pixel gallium-arsenide array, *Nuclear Instruments and Methods A*, Vol. 487, Iss. 1-2, pp. 78-89.

**Everhart, T.E., and Hoff, P.H., 1971**, Determination of kilovolt electron dissipation vs penetration distance in solid materials, *Journal of Applied Physics*, Vol. 42, No. 13, pp. 5837-5846.

**Fano, U., 1947**, Ionization Yield of Radiations. II. The Fluctuation of the Number of Ions, *Physical Review*, Vol. 72, No. 1, pp. 26-29.

**Farrell, R., Vanderpuye, K., Entine, G., Squillante, M.R., 1991**, High resolution low energy avalanche photodiode X-ray detectors, *IEEE Transactions on Nuclear Science*, Vol. 38, No. 2, pp. 144-147.

**Franklin, M., Fry, A., Gan, K.K., Han, S., Kagan, H., Kanda, S., Kania, D., Kass, R., Kin, S.K., Malchow, R., Morrow, F., Olsen, S., Palmer, W.F., Pan, L.S., Sannes, F., Schnetzer, S., Stone, R., Sugimoto, Y., Thomson, G.B., White, C., Zhao, S., 1992**, Development of diamond radiation detectors for SSC and LHC, *Nuclear Instruments and Methods A*, Vol. 315, Iss. 1-3, pp. 39-42.

**Fraser, G.W., 1989**, *X-ray detectors in Astronomy*, Cambridge University Press, Cambridge, UK, ISBN: 978-0-521-10603-0.

**Fraser, G.W., 2008**, *Extraterrestrial Analysis: Planetary X-Ray Fluorescence from Orbiting Spacecraft and Landers*, in Potts, P.J. & West, M., 2008, *Portable X-ray fluorescence spectroscopy: capabilities for in situ analysis*, RSC publishing, Cambridge, UK, ISBN: 978-0-854-04552-5.

**Fraser, G.W., Abbey, A.F. Holland, A., McCarthy, K., Owens, A., Wells, A., 1994**, The X-ray energy response of silicon Part A. Theory, *Nuclear Instruments and Methods A*, Vol. 350, Iss. 1-2, pp. 368-378.

**Fuke, S., Sano, K., Kuwahara, K., Takano, Y., Sato, M., Imai, T., 1995**, Lattice relaxation of AlGaAs layers grown on GaAs(100) substrate plane by organometallic vapour phase epitaxy, *Journal of Applied Physics*, Vol. 77, Iss. 1, pp. 420-422.

**Gatti, E., Rehak, P., 1984**, Semiconductor drift chamber – an application of a novel charge transport scheme, *Nuclear Instruments and Methods in Physics Research A*, Vol. 225, Iss. 3, pp. 608-614.

**Gatti, E., Manfredi, P.F., Sampietro, M., Speziali, V., 1990**, Suboptimal filtering of 1/f-noise in detector charge measurements, *Nuclear Instruments and Methods A*, Vol. 297, Iss. 3, pp. 467-478.

**Gladstone, G.R., Waite, J.H., Grodent, D., Lewis, W.S., Crary, F.J., Elsner, R.F., Weisskopf, M.C., Majeed, T., Jahn, J.-M., Bhardwaj, A., Clarke, J.T., Young, D.T., Dougherty, M.K., Espinosa, S.A., Cravens, T.E., 2002**, A pulsating auroral X-ray hot spot on Jupiter, *Nature*, Vol. 415, pp. 1000-1003.

**Goldberg, Yu., Levinshtein, M.E., Rumyantsev, S.L., 2001**, in Levinshtein, M.E., Rumyantsev, S.L., Shur, M.S., 2001, *Properties of Advanced Semiconductor Materials: GaN, AlN, SiC, BN, SiC, SiGe*, John Wiley & Sons, New York, USA, ISBN: 978-0-471-35827-5.

**Grande, M., Kellett, B.J., Howe, C., Perry, C.H., Swinyard, B., Dunkin, S., Huovelin, J., Alha, L., D'Uston, L.C., Maurice, S., Gasnault, O., Couturier-Doux, S., Barabash, S., Joy, K.H., Crawford, I.A., Lawrence, D., Fernandes, V., Casanova, I., Wiczorek, M., Thomas, N., Mall, U., Foing, B., Hughes, D., Alleyne, H., Russell, S., Grady, M., Lundin, R., Baker, D., Murray, C.D., Guest, J., Christou, A., 2007**, The D-CIXS X-ray spectrometer on the SMART-1 mission to the Moon – First results, *Planetary and Space Science*, Vol. 55, Iss. 4, pp. 494-502.

**Gutiérrez, M., Herrera, M., González, D., Aragón, G., Sánchez, J.J., Hopkinson, M., García, R., 2002**, Relaxation study of AlGaAs cladding layers in InGaAs/GaAs (111)B lasers designed for 1.0-1.1  $\mu\text{m}$  operation, *Microelectronics Journal*, Vol. 33, Iss. 7, pp. 553-557.

**Hall, D.J., & Holland, A., 2010**, Space radiation environment effects of X-ray CCD background, *Nuclear Instruments and Methods A*, Vol. 612, Iss. 2, pp. 320-327.

**Harrison, C., 2009**, *Railway Locomotive Oil Analysis*, Scientifics Ltd., Derby, UK, [Conversation] (Personal communication, 17th February 2009).

**Harrison, C.N., David, J.P.R., Hopkinson, M., Rees, G.J., 2002**, Temperature dependence of avalanche multiplication in submicron  $\text{Al}_{0.6}\text{Ga}_{0.4}\text{As}$  diodes, *Journal of Applied Physics* Vol. 92, Iss. 12, pp. 7684-7686.

**Heilbron, J. L., 1966**, The works of H. G. J. Moseley, *Isis*, Vol. 57, No. 3, pp. 336-364.

**Hu, J., Xin, X., Joseph, C.L., Li, X., Zhao, J.H., 2008**,  $1 \times 16$  Pt/4H-SiC Schottky photodiode array for low-level EUV and UV spectroscopic detection, IEEE Photonics Technology Letters, Vol. 20, No. 24, pp. 2030-20-32.

**Hwang, H.-P., Cheng, Y.-S., Shieh, J.-L., Chyi, J.-I., 2001**, A comparative study of the passivation films on AlGaAs/GaAs heterojunction diodes and bipolar transistors, IEEE Transactions on Electron Devices, Vol. 48, No. 2, pp. 185-189.

**Jenkins, R., Gould, R.W., Gedcke, D., 1995**, Quantitative X-ray Spectrometry, Marcel Dekker, Inc., New York, USA, ISBN: 978-0-824-79554-2.

**Kashiwagi, T., Hibino, K., Kitamura, H., Mori, K., Okuno, S., Takashima, T., Uchihori, Y., Yajima, K., Yokota, M., Yoshida, K., 2006**, Investigation of Basic Characteristics of Synthetic Diamond Radiation Detectors, IEEE Transactions on Nuclear Science, Vol. 53, No. 2, pp. 630-635.

**Kataoka, J., Saito, T., Kuramoto, Y., Ikagawa, T., Yatsu, Y., Kotoku, J., Arimoto, M., Kawai, N., Ishikawa, Y., Kawabata, N., 2005**, Recent progress of avalanche photodiodes in high-resolution X-rays and  $\gamma$ -rays detection, Nuclear Instruments and Methods A, Vol. 541, Iss. 1-2, pp. 398-404.

**Keister, J.W., Smedley, J., Dimitrov, D., Busby, R., 2010**, Charge Collection and Propagation in Diamond X-ray Detectors, IEEE Transactions on Nuclear Science, Vol. 57, Iss. 4, pp. 2400-2404.

**Keithley Instruments Inc, 1975**, Instruction Manual Model 427 Current Amplifier, Document Number 29103, Cleveland, Ohio, USA.

**Kemmer, J., Lutz, G., 1987**, New detector concepts, Nuclear Instruments and Methods A, Vol. 253, Iss. 3, pp. 365-377.

**Kemmer, J., Lutz, G., Prechtel, U., Schuster, K., Sterzik, M., Strüder, L., Ziemann, T., 1990**, Experimental confirmation of a new semiconductor detector principle, Nuclear Instruments and Methods A, Vol. 288, Iss. 1, pp. 92-98.

**Knoll, G., 2000**, Radiation Detection and Measurement, 3rd ed., John Wiley & Sons, Inc., New York, USA. ISBN: 978-0-471-07338-3.

**Lauter, J., Protić, D., Förster, A., Lüth, H., 1995**, AlGaAs/GaAs SAM-avalanche photodiode: An X-ray detector for low energy photons, *Nuclear Instruments and Methods A*, Vol. 356, Iss. 2-3, pp. 324-329.

**Lauter, J., Förster, A., Lüth, H., Müller, K.D., Reinartz, R., 1996**, AlGaAs/GaAs Avalanche Detector Array 1Gbit/s X-ray receiver for timing measurements, *IEEE Transactions on Nuclear Science*, Vol. 43, No. 3, pp. 1446-1451.

**Lechner, P., Eckbauer, S., Hartmann, R., Krisch, S., Hauff, D., Richter, R., Soltau, H., Strüder, L., Fiorini, C., Gatti, E., Longoni, A., Sampietro, M., 1996**, Silicon drift detectors for high resolution room temperature X-ray spectroscopy, *Nuclear Instruments and Methods A*, Vol. 377, Iss. 2-3, pp. 346-351.

**Lechner, P., Fiorini, C., Hartmann, R., Kemmer, J., Krause, N., Leutenegger, P., Longoni, A., Soltau, H., Stötter, D., Stötter, R., Strüder, L., Weber, U., 2001**, Silicon drift detectors for high count rate X-ray spectroscopy at room temperature, *Nuclear Instruments and Methods in Physics Research A*, Vol. 458, Iss. 1-2, pp. 281-287.

**Lees, J.E., 2010**, Spectroscopic model for SiC X-ray detectors, *Nuclear Instruments and Methods A*, Vol. 613, Iss. 1, pp. 98-105.

**Lees, J.E., Bassford, D.J., Fraser, G.W., Horsfall, A.B., Vassilevski, K.V., Wright, N.G., Owens, A., 2007**, Semi-transparent SiC Schottky diodes for X-ray spectroscopy, *Nuclear Instruments and Methods A*, Vol. 578, Iss. 1, pp. 226-234.

**Lees, J.E., Bassford, D.J., Ng, J.S., Tan, C.H., David, J.P.R., 2008**, AlGaAs diodes for X-ray spectroscopy, *Nuclear Instruments and Methods A*, Vol. 594, Iss. 2, pp. 202-205.

**Lees, J.E., Bassford, D.J., Bunce, E.J., Sims, M.R., Horsfall, A.B., 2009**, Silicon Carbide X-ray detectors for planetary exploration, *Nuclear Instruments and Methods A*, Vol. 604, Iss. 1-2, pp. 174-176.

**Lees, J.E., Barnett, A.M., Bassford, D.J., Stevens, R.C., Horsfall, A.B., 2011**, SiC X-ray detectors for harsh environments, *J. Inst.*, Vol. 6, C01032.

**Lowell, R.P., and Myesha DuBose, 2005**, Hydrothermal systems on Europa, *Geophysical Research Letters*, Vol. 32, Iss. 5, L05202.

**Marinelli, M., Milani, E., Morgada, M.E., Pucella, G., Rodriguez, G., Tucciarone, A., Verona-Rinati, G., Angelone, M., Pillon, M., 2004**, Separate measurement of electron and hole mean drift distance in CVD diamond, *Diamond and Related Materials*, Vol. 13, Iss. 4-8, pp. 929-933.

**McCarthy, K.J., Owens, A., Holland, A.D., Wells, A.A., 1995**, Modelling the X-ray response of charge coupled devices, *Nuclear Instruments and Methods A*, Vol. 362, Iss. 2-3, pp. 538-546.

**McGregor, D.S. and Hermon, H., 1997**, Room-temperature compound semiconductor radiation detectors, *Nuclear Instruments and Methods A*, Vol. 395, Iss. 1, pp. 101-124.

**McIntyre, R.J., 1966**, Multiplication noise in uniform avalanche photodiodes, *IEEE Transactions on Electron Devices*, Vol. ED-13, No. 1, pp. 164-168.

**Miyaguchi, K., 1999**, CCD developed for scientific application by Hamamatsu, *Nuclear Instruments and Methods A*, Vol. 436, Iss. 1-2, pp. 24-31.

**Miyaguchi, K., Suzuki, H., Dezaki, J., Yamamoto, K., 1999**, CCD developed for scientific application by Hamamatsu, *Nuclear Instruments and Methods A*, Vol. 436, Iss. 1-2, pp. 24-31.

**Molhave, K., 2006**, in “The Opensource Handbook of Nanoscience and Nanotechnology”,

[http://en.wikibooks.org/wiki/File:Bandgap\\_vs\\_Lattice\\_Const\\_for\\_Semiconductors\\_5.25-6.74\\_Angstrom.jpg](http://en.wikibooks.org/wiki/File:Bandgap_vs_Lattice_Const_for_Semiconductors_5.25-6.74_Angstrom.jpg), last retrieved 18th January 2011.

**Moroz, V. I., 2002**, Studies of the atmosphere of Venus by means of spacecraft: solved and unsolved problems, *Advances in Space Research*, Vol. 29, Iss. 2, pp. 215-225.

**Moseley, H., 1913**, The high-frequency spectra of the elements, *Philosophical Magazine*, Vol. 26, Iss. 156, pp. 1024-1034.

**Nakajima, H., Yamaguchi, H., Matsumoto, H., Tsuru, T.G., Koyama, K., Kissel, S., LaMarr, B., Bautz, M., 2005**, The ground calibration of X-ray CCD cameras (XIS) with front-illuminated chips onboard Astro-E2, Nuclear Instruments and Methods A, Vol. 541, Iss. 1-2, pp. 365-371.

**Nava, F., Bertuccio, G., Cavallini, A., Vittone, E., 2008**, Silicon carbide and its use as a radiation detector material, Measurement Science and Technology, Vol. 19, Iss. 10, pp. 102001-102026.

**Nava, F., Vanni, P., Lanzieri, C., Canali, C., 1999**, Epitaxial silicon carbide charge particle detectors, Nuclear Instruments and Methods A, Vol. 437, Iss. 2-3, pp. 354-358.

**Ness, J.-U., 2004**, X-ray emission from Saturn, Astronomy and Astrophysics, Vol. 418, pp. 337-345.

**Neudeck, P.G., Garverick, S.L., Spry, D.J., Chen, L.-Y., Beheim, G.M., Krasowski, M.J., Mehregany, M., 2009**, Extreme temperature 6H-SiC JFET integrated circuit technology, Physica Status Solidi A, Vol. 206, No. 10, pp. 2329-2345.

**Ng, B.K., David, J.P.R., Plimmer, S.A., Hopkinson, M., Tozer, R.C., Rees, G.J., 2000**, Impact ionization coefficients of  $\text{Al}_{0.8}\text{Ga}_{0.2}\text{As}$ , Applied Physics Letters, Vol. 77, No. 26, pp. 4374-4376.

**Ng, B. K., David, J.P.R., Plimmer, S.A., Rees, G.J., Tozer, R.C., Hopkinson, M., Hill, G., 2001**, Avalanche Multiplication Characteristics of  $\text{Al}_{0.8}\text{Ga}_{0.2}\text{As}$  Diodes, IEEE Transactions on Electronic Devices, Vol. 48, No. 10, pp. 2198-2204.

**Ng, B.K., David, J.P.R., Tozer, R.C., Hopkinson, M., Hill, G., Rees, G.J., 2002**, excess noise characteristics of  $\text{Al}_{0.8}\text{Ga}_{0.2}\text{As}$  Avalanche photodiodes, IEEE Photonics Technology Letters Vol. 14, No. 4, pp. 522-524.

**Ng, J.S., 2009**, Discussion of electric field profile, University of Sheffield, Sheffield, UK, (personal communication, 10th September 2009).

**NSM Archive, 2004**, Physical properties of semiconductors, NSM Archive, Ioffe, Russia, <http://www.ioffe.rssi.ru/SVA/NSM/Semicond/>, last retrieved 21st April 2011.

**Ochi, A., Nishi, Y., Tanimori, T., 1996**, Study of a large area avalanche photodiode as a fast photodiode and a soft X-ray detector, Nuclear Instruments and Methods A, Vol. 378, Iss. 1-2, pp. 267-274.

**Okada, T., Shirai, K., Yamamoto, Y., Arai, R., Ogawa, K., Hosono, K., Kato, M., 2006**, X-ray Fluorescence Spectrometry of Asteroid Itokawa by Hayabusa, Science, Vol. 312, No. 5778, pp. 1338-1341.

**Owens, A., and Peacock, A., 2004**, Compound semiconductor radiation detectors, Nuclear Instruments and Methods A, Vol. 531, Iss. 1-2, pp. 18-37.

**Owens, A., Bavdaz, M., Peacock, A., Poelaert, A., Anderson, H., Nenonen, S., Tröger, L., Bertuccio, G., 2001**, Hard X-ray spectroscopy using small format GaAs arrays, Nuclear Instruments and Methods A, Vol. 466, Iss. 1, pp. 168-173.

**Owens, A., Bavdaz, M., Peacock, A., Andersson, H., Nenonen, S., Krumrey, M., Puig, A., 2002a**, High resolution X-ray spectroscopy using a GaAs pixel detector, Nuclear Instruments and Methods A, Vol. 479, Iss. 2-3, pp. 531-534.

**Owens, A., Bavdaz, M., Andersson, H., Gagliardi, T., Krumrey, M., Nenonen, S., Peacock, A., Taylor, I., and Tröger, L., 2002b**, The X-ray response of CdZnTe, Nuclear Instruments and Methods A, Vol. 484, Iss. 1-3, pp. 242-250.

**Plimmer, S.A., David, J.P.R., Herbert, D.C., Lee, T.-W., Rees, G.J., Houston, P.A., Grey, R., Robson, P.N., Higgs, A.W., Wright, D.R., 1996**, Investigation of Impact Ionization in Thin GaAs Diodes, IEEE Transactions on Electron Devices, Vol. 43, No. 7, pp. 1066-1072.

**Plimmer, S.A., David, J.P.R., Rees, G.J., Robson, P.N., 2000**, Ionization coefficients in  $\text{Al}_x\text{Ga}_{1-x}\text{As}$  ( $x = 0-0.60$ ), Semiconductor Science and Technology, Vol. 15 No. 7, pp. 692-699.

**PNSensor GmbH, N.D.**, Silicon Drift Detector Development, <http://www.pnsensor.de/Welcome/Detector/SDD/index.html>, last retrieved 23rd March 2011.

**Potts, P.J. & West, M., 2008**, Portable X-ray fluorescence spectroscopy: Capabilities for in Situ Analysis, RSC publishing, Cambridge, UK, ISBN: 978-0-854-04552-5.

**Potts, P.J., 1987**, A handbook of silicate rock analysis, Blackie, Glasgow, Scotland, ISBN: 978-0-412-00881-8.

**Pullia, A., and Bertuccio, G., 1996**, Resolution limits of silicon detectors and electronics for soft X-ray spectroscopy at non cryogenic temperatures, Nuclear Instruments and Methods A, Vol. 380, Iss. 1-2, pp. 1-5.

**Ripamoni, G., Capasso, F., Hutchinson, A.L., Muehlner, D.J., Walker, J.F., Malik, R.J., 1990**, Realization of a staircase photodiode: Towards a solid-state photomultiplier, Nuclear Instruments and Methods A, Vol. 288, Iss. 1, pp. 99-103.

**Ruddy, F.H. and Siedel, J.G., 2006**, Effects of gamma irradiation on silicon carbide semiconductor radiation detectors, 2006 IEEE Nuclear Science Symposium Conference Record, pp. 583-587.

**Ruddy, F.H., Seidel, J.G., Chen, H., Dulloo, A.R., Ryu, S.-H., 2006**, High-resolution alpha-particle spectrometry using 4H silicon carbide semiconductor detectors, IEEE Transactions on Nuclear Science, Vol. 53, No. 3, pp. 1713-1718.

**Ruegg, H.W., 1967**, An optimized avalanche photodiode, IEEE Transactions on Electron Devices, Vol. 14, No. 5, pp. 239-251.

**Saleh, M.A., Hayat, M.M., Saleh, B.E.A., Teich, M.C., 2000**, Dead-space-based theory correctly predicts excess noise factor for thin GaAs and AlGaAs avalanche photodiodes, IEEE Transactions on Electron Devices, Vol. 47, No. 3, pp. 625-633.

**Salvatori, S., Rossi, M.C., Galluzzi, F., 1999**, Minority-carrier transport parameters in CVD diamond, Carbon, Vol. 37, Iss. 5, pp. 811-816.

**Schötzig, U., 2000**, Half-life and X-ray emission probabilities of  $^{55}\text{Fe}$ , Applied Radiation and Isotopes, Vol. 53, Iss. 3, pp. 469-472.

**Silenas, A., 2004**, Graded-gap  $\text{Al}_x\text{Ga}_{1-x}\text{As}$  analyzer of X-ray and alpha-particle spectra, Nuclear Instruments and Methods A, Vol. 531, Iss. 1-2, pp. 92-96.

**Silenas, A., Pozela, J., Smith, K.M., Pozela, K., Jasutis, V., Dapkus, L., Juciene, V., 2002**, Non-uniformly doped graded-gap  $\text{Al}_x\text{Ga}_{1-x}\text{As}$  X-ray detectors with high photovoltaic response, Nuclear Instruments and Methods A., Vol. 487, Iss. 1-2, pp. 54-59.

**Silenas, A., Pozela, K., Dapkus, L., Jasutis, V., Juciene, V., Pozela, J., Smith, K.M., 2003**, Graded-gap  $\text{Al}_x\text{Ga}_{1-x}\text{As}$  X-ray detector with collected charge multiplication, Nuclear Instruments and Methods A, Vol. 509, Iss. 1-3, pp. 30-33.

**Silenas, A., Dapkus, L., Pozela, K., Pozela, J., Juciene, V., Jasutis, V., 2005**, Radiation hardness of graded-gap  $\text{Al}_x\text{Ga}_{1-x}\text{As}$  X-ray detectors, Nuclear Instruments and Methods A, Vol. 546, Iss. 1-2, pp. 228-231.

**Silenas, A., Pozela, J., Pozela, K., Dapkus, L., Juciene, V., 2006**, High spatial resolution graded-gap  $\text{Al}_x\text{Ga}_{1-x}\text{As}$  X-ray detector, Nuclear Instruments and Methods A, Vol. 563, Iss. 1, pp. 21-23.

**Silenas, A., Miller, A., Pozela, J., Pozela, K., Dapkus, L., Juciene, V., 2011**, Graded-gap  $\text{Al}_x\text{Ga}_{1-x}\text{As}$  detector for high-energy electron beam dosimetry, Nuclear Instruments and Methods A, Vol. 633, Suppl. 1, pp. S62-S64.

**Siliconix, 1997**, 2N4416/2N4416A/SST4416 N-Channel JFETs, Data Sheet, S-52424, Rev. E, 14-Apr-97, Vishay Electronic GmbH, Selb, Germany.

**Spanovich, N., Smith, M.D., Smith, P.H., Wolff, M.J., Christensen, P.R., Squires, S.W., 2006**, Surface and near-surface atmospheric temperatures for the Mars Exploration Rover landing sites, Icarus, Vol. 180, Iss. 2, pp. 314-320.

**Squillante, M.R., Reiff, G., Entine, G., 1985**, Recent advances in large area avalanche photodiodes, IEEE Transactions on Nuclear Science, Vol. 32, No. 1, pp. 863-866.

**Sridharan, M.G., Mekaladevi, M., Rodriguez-Viejo, J., Narayandass, Sa.K., Mangalaraj, D., Lee, H.C, 2004**, Spectroscopic ellipsometry studies on polycrystalline  $\text{Cd}_{0.9}\text{Zn}_{0.1}\text{Te}$  thin films, Physica Status Solidi (a), Vol. 201, No. 4, pp. 782-790.

**Swinyard, B.M., Joy, K.H., Kellett, B.J., Crawford, I.A., Grande, M., Howe, C.J., Fernandes, V.A., Gasnault, O., Lawrence, D.J., Russell, S.S., Wieczorek, M.A., Foring, B.H., The SMART-1 team, 2009**, X-ray fluorescence observations of the moon by SMART-1/D-CIXS and the first detection of Ti  $K\alpha$  from the lunar surface, Planetary and Space Science, Vol. 57, Iss. 7, pp. 744-750.

**Tan, C.H., David, J.P.R., Plimmer, S.A., Rees, G.J., Tozer, R.C., Grey, R., 2001,** Low Multiplication Noise in Thin  $\text{Al}_{0.6}\text{Ga}_{0.4}\text{As}$  Avalanche Photodiodes, IEEE Transactions on Electron Devices Vol. 48, No. 7, pp. 1310-1317.

**Tan, C.H., Gomes, R.B., David, J.P.R., Barnett, A.M., Bassford, D.J., Lees, J.E., Ng, J.S., 2011,** Avalanche Gain and Energy Resolution of Semiconductor X-ray Detectors, IEEE Trans. Elect. Dev., Vol. 58, No. 6, pp. 1696-1701.

**Thurlby Thandar Instruments Ltd, N.D.,** PL Series Instruction Manual, Book Part No. 45811-0170, Iss. 12, Huntingdon, Cambridgeshire, UK.

**Thomson, R.E., and Delaney, J.R., 2001,** Evidence for a weakly stratified European ocean sustained by seafloor heat flux, Vol. 106, No. E6, pp. 12355-12365.

**Van Zeghbroeck, B., 2007,** Principles of Semiconductor Devices, University of Colorado, Boulder, USA, <http://ece-www.colorado.edu/~bart/book/>, last retrieved 23rd June 2011.

**Weng, M.H., Mahapatra, R., Horsfall, A.B., Wright, N.G., 2007,** Hydrogen sulphide detection in extreme environments, Journal of Physics: Conference Series, Vol. 76, No. 1, 012005.

**Withers, P., and Smith, M. D., 2006,** Atmospheric entry profiles from the Mars Exploration Rovers Spirit and Opportunity, Icarus, Vol. 198, Iss. 1, pp. 133-142.

**Wright, N.G., and Horsfall, A.B., 2007,** SiC sensors: a review, Journal of Physics D: Applied Physics, Vol. 40, No. 20, pp. 6345-6354.

**Xiaolong, H., Shenggui, Y., Chunsheng, D., 2010,** Evaluation of the decay data of  $^{109}\text{Cd}$ , Nuclear Instruments and Methods A, Vol. 621, Iss. 1-3, pp. 443-446.

**Yang, Z., Hou, X., Jones, B.T., 2003,** Determination of wear metals in engine oil by mild acid digestion and energy dispersive X-ray fluorescence spectrometry using solid phase extraction disks, Talanta, Vol. 59, Iss. 4, pp. 673-680.

**Yatsu, Y., Kuramoto, Y., Kataoka, J., Kotoku, J., Saito, T., Ikagawa, T., Sato, R., Kawai, N., Kishimoto, S., Mori, K., Kamae, T., Ishikawa, Y., Kawabata, N., 2006,** Study of avalanche photodiodes for soft X-ray detection below 20 keV, Vol. 564, Iss. 1, pp. 134-143.

**Zheng, X.G., Yaun, P., Kinsey, G.S., Holmes, A.L., Streetman, G.G., Campbell, J.C., 2000, IEEE Journal of Quantum Electronics, Vol. 36, No. 10, pp. 1168-1173.**